Investigation of plug extrusion processes in counterpropagating waves

A. K. Divakov, V. A. Ermolaev, N. I. Zhigacheva, Yu. I. Meshcheryakov, Yu. A. Petrov, S. A. Petrochenkov, and M. V. Sil'nikov

Institute of Problems in Mechanical Engineering, St. Petersburg;
Scientific-Industrial Organization for Special Materials, St. Petersburg
(Submitted February 18, 1998)
Pis'ma Zh. Tekh. Fiz. **24**, 1–6 (October 12, 1998)

The creation of a radially nonuniform stressed state is proposed to achieve intensive shear processes under high-velocity loading of targets with a planar impactor. The technique allows laser differential interferometry to be used to study the microstructure kinetics of the deformable material. Experimental results are described.
[S1063-7850(98)00110-4]

The main difficulty involved in studying plug extrusion is the limited scope for measurements of the force and deformation characteristics of the dynamic response of the target, especially at the initial stage of penetration. Usually we can only measure the flight velocity of the impactor. By using pulsed x-ray photography, we can also measure the velocity of the interface between the front part of the impactor and the unperturbed part of the target. However, the spatial and temporal resolution in these experiments is as yet inadequate to study the initial stage of penetration which has so far been the least studied.

However, investigations of the dynamic backside spallation strength of targets using laser interferometry of the free target surface can yield detailed information not only on the temporal characteristics of the average velocity of this surface but also on the microstructure kinetics. In particular, the time variation of the particle velocity dispersion can be recorded at the so-called mesoscopic level of deformation and fracture (0.1–10 μm) (Ref. 1).

In this context, it is tempting to develop schemes for loading a planar target both to achieve plug extrusion and so that we could use methods of recording dynamic deformation and fracture used to study uniaxial deformation and backside spallation. With this aim we propose to use configurations of impactor and target which could create a radially nonuniform stressed state in the target, providing conditions for plug extrusion in a planar target under the action of both an unconventional elongated impactor and a conventional planar impactor used to study uniaxial deformation processes.

We shall analyze possible loading schemes. A nonuniform stressed state implies that the sample contains regions where the parameters of the pressure pulses differ. The simplest method is to vary the pulse length. In the light of this observation, we shall analyze the following loading schemes to produce a nonuniform stressed state under planar impact.

a) The impact surfaces of the impactor and the target are planar and the back of the impactor has a stepped profile. In this geometry, radial nonuniformity of the stressed state of the target occurs at the trailing edge of the incident pressure pulse.

b) The impactor and the target have planar impact surfaces and the back of the target has a stepped profile. A nonuniform stressed state occurs at the leading edge of the reflected pressure pulse. In this scheme, conditions where the shear strain rate is double that of the conventional interaction between an elongated impactor and a target are created near the protrusion.

c) The impactor and the target have planar impact surfaces and nonuniform boundary conditions for the reflected pressure pulse at the back of the target which are established by using a limiting disk with a hole. At the contact surface between the target and the disk, the incident wave passes into the disk material without reflection, being reflected first from the free surface of the target and then, after a delay, by the free surface of the disk.

d) Simulation of impact between an elongated impactor and a planar target.

Schemes (b) and (c) are preferred because in these cases, shear fracture is initiated from the free surface which allows the initial stage of the penetration process to be studied. In addition, in scheme (d) no wave interactions occur and the impactor velocity must be doubled compared with schemes (a) and (c) to achieve the shear strain rate required for penetration.

The following pattern should be observed for case (b): if t_0 is the time of arrival of a compression pulse at the free surface of a target protrusion, the pulse reaches the smooth part of the target at time $t_1 = t_0 + h/C_1$, where C_1 is the longitudinal velocity of sound in the target. From this time onward, a transverse perturbation wave begins to propagate in the radial direction, reaching the central part of the target where the interferometer beam is usually focused, by the time $t_2 = t_1 + d/C_s$ (C_s is the velocity of the transverse waves and d is the diameter of the protrusion). In order to record this wave, the interferometer must distinguish the times of arrival of the longitudinal wave at the free surface and the transverse wave. A second variant involves using two interferometers to independently record the two longitudinal waves successively reaching the surface of the target and the protrusion. In both cases, the dispersion of the particle velocities can be recorded in addition to the average velocity of

the target and the protrusion, so that the microstructure kinetics can be related to the nature of the plug extrusion.

Impact tests and microstructural investigations were aimed at developing an optimum scheme for plug extrusion by planar impact of an impactor on a target. One of the most important criteria, if not the main one, for similarity between the processes achieved using the conventional method of plug penetration by an elongated impactor and that proposed here (shear in counterpropagating waves at the edge of a step) is the similarity between the microstructural processes taking place in the shear zone in both cases. Two variants of the system were examined, with a protrusion at the back of the target and with an additional disk. In the tests using a limiting disk, a target of the same thickness as the impactor was used to eliminate backside spallation. For a D-16 aluminum alloy sample 1 mm thick, penetration was achieved for an impactor velocity of 350 m/s. For 5 mm thick samples of Ts-85 ductile high-strength steel the initial phase of shear fracture was only initiated at a velocity of 453 m/s. It should be noted that serious technical difficulties are involved in achieving shear fracture by scheme (c). Ideally the limiting disk should not be deformed in the region of contact with the target. However, disks made of KhVG steel heat-treated to hardness HRC=64 u did undergo deformation and partial fracture on the target side which changes the conditions of localization of the shear. Thus, further tests were carried out using scheme (b). For a steel impactor 3 mm thick and an impact velocity of 390 m/s, a shear crack formed all around the protrusion and at a velocity of 556 m/s the plug was completely broken through.

Microstructural analyses of the fracture zone show that the fracture geometry depends very strongly on the anisotropy of the target material. For example, for the isotropic D-16 alloy the plug penetration occurs precisely along the boundary of the protrusion. For Ts-85 steel this shear zone has a stepped geometry, as can be seen from the photograph (see Fig. 1). A longitudinal shear crack begins to grow along the boundary of the protrusion from the back of the target surface. At a depth of $\approx$1 mm it then becomes a normal cleavage crack running parallel to the free surface of the sample. This position can be attributed to the higher shear strength of this material compared with the spalling strength as a result of the strong anisotropy of the steel structure induced by rolling. At a certain distance from the free surface the energy of the elastic-plastic wave is insufficient to continue the shear fracture but is still sufficient for cleavage. Thus, when the longitudinal shear crack stops, the stress field is redistributed so that a zone of tensile stresses forms near the stopped shear crack. The situation is reminiscent of the familiar Zener–Stroh mechanism for the nucleation of cleavage cracks by blocking of dislocation pile-ups.

FIG. 1. Crack structure near a protrusion in a Ts-85 steel sample.

The results of tests using isotropic and strongly anisotropic materials show that the proposed method of initiating shear deformation can in fact produce shear deformation similar to that obtaining during penetration of a plug by an elongated impactor. However, in contrast to this last case, penetration of the plug is achieved at less than half the impactor velocity. In addition, the technique can be used to study the initial stage of penetration by recording the wave processes using methods used to study backside spallation.

In tests using Ts-85 steel it was observed that, whereas for a 5 mm thick sample shear fracture was initiated at a velocity of 453 m/s, for a sample 2.2 mm thick no traces of shear fracture were identified at the boundary of the protrusion even at a velocity of 523 m/s. In our view, this phenomenon is attributable to the different microstructure kinetics. It is known[2] that the particle velocity distribution function varies substantially as a wave penetrates inside a material, changing from nonsteady-state with a large dispersion of particle velocities to steady-state with a narrower velocity spread. In cases of large dispersion, rotational mechanisms of fracture are established, whereas for a narrow spread the mechanisms are translational in the form of bands of localized shear, which reduces the shear strength of the material. These assumptions may be checked by using an interferometer which can measure the particle velocity dispersion at the mesolevel.[1]

[1] Yu. I. Mescheryakov and A. K. Divakov, Dymat-Journal No. 4, 2681 (1994).
[2] Yu. I. Mescheryakov, N. A. Makhutov, and S. A. Atroshenko, J. Mech. Phys. Solids **422**, 1435 (1994).

Translated by R. M. Durham

Laws governing the reaction of a system

G. E. Skvortsov

St. Petersburg State University
(Submitted April 6, 1998)
Pis'ma Zh. Tekh. Fiz. **24**, 7–12 (October 12, 1998)

The law and principle of dynamic correspondence are used to analyze the laws governing the reaction of a system in the form of functional action–reaction relations for a wide range of nonequilibrium conditions. The dynamic correspondence is reflected by a dynamic object process classifier which is used to indicate possible new highly nonequilibrium effects. The laws of reaction are used to give a simple description of a structural transition for a wide range of systems. © *1998 American Institute of Physics.* [S1063-7850(98)00210-9]

A major problem involves determining the characteristic features and the functional form of the reaction of a system to an action.

The qualitative characteristics of the reaction of a wide range of systems in physics, chemistry, and biology are determined by the basic laws of reactions.[1–5]

The initial law of structural conditionality is subsequently modified in the form of a law measuring action and also the law and principle of dynamic correspondence, which are more convenient to use.

These laws are used to analyze the laws governing the reaction of systems in the form of functional relations of the determining quantities and measures of action as a function of their range of values.

The principle of dynamic correspondence is used to indicate the classes of laws and effects in terms of an object process classifier.

A fairly universal dependence is given for the structural transition reaction which modifies the model[5] and is used to describe transitions in physical, chemical, and biological systems.

1. The law of action measure states that the result of an action on a system is determined by the magnitude of the action relative to the corresponding structural characteristic of the system.

The measure of action is defined by the ratio of the action factor g to the corresponding structural factor $s[g]$

$$Gs=\frac{g}{s[g]}: \quad A_{ns}=\left|\frac{a_n-a_{n0}}{a_{ns}-a_{n0}}\right|, \quad F_s=\left|\frac{f}{f_s}\right|, \tag{1.1}$$

$$T_s=\tau_s\left|\partial t \ln\left|\frac{a_n}{a_{ns}}\right|\right|, \quad Ls=\lambda_s\left|\partial x \ln\left|\frac{a_n}{a_{ns}}\right|\right|, \tag{1.2}$$

$$G_0=\frac{g}{s[0]}, \quad S=\frac{s[g]}{s_0}. \tag{1.3}$$

The degree of nonequilibrium may be given by

$$C=\sum_s \frac{Gs}{1+\gamma_s(Gs-1)^2}, \tag{2}$$

where γ_s is a normalizing factor. These expressions use the notation from Refs. 2–5.

The action g includes the initial and boundary conditions, and the external and internal actions.

The measure of action together with the initial measure (1.3) and the degree of nonequilibrium are sufficient to determine the ''dynamism'' of any systems.

It is useful to compare the law of action measure with its analog for biological systems, the initial level law (Ref. 6, p. 121).

2. The principle of dynamic correspondence indicates that different processes in different systems may be compared by using a set of measures of action and degrees of nonequilibrium.

The law of dynamic correspondence states that processes have similarity, a measure of correspondence which is greater, the closer are the measures of action and the degrees of nonequilibrium for these processes.

The principle of dynamic correspondence indicates that partial correspondences exist and stimulates a search for these on the basis of various factors: similarity of equation, regimes, functional dependence of key quantities, process analogies, and so on.

The similarities of the equations and transition regimes for average nonequilibrium serve as the basis for the universality of the synergetics. Similarity based on equations and process analogies forms the content of the theory put forward in Ref. 7.

The general dynamic equations and the functional form of the general determining relations[8] provide the basis for realizing the principle of dynamic correspondence for highly nonequilibrium processes.

The principle of dynamic correspondence includes a whole range of effective specializations: the principle of negative feedback (Le Chatelier), the principle of ''kinetic perfection'' for evolving systems,[9] the Bauer principle of stable nonequilibrium of living systems, and so on.

3. The law and principle of dynamic correspondence are realized in the form of an object process classifier.

Object process classifiers consist of condensed information on objects and possible processes therein in the form of a table (matrix) which combines the class scale of the objects

(nuclear, atomic, molecular, and so on) with the intensity scale of the process, an increasing measure of action.

On the dynamic scale of object process classifiers are data on equilibrium structural characteristics of object systems; thermomechanics, $G<0.1$; classical dynamic theories, $G<0.2$; synergetics, $0.2<G<0.4$; superhydrodynamics,[10] $0.4<G<1$; structural transition regimes, $G\approx 1$; region of anomalous processes, $G\gtrsim 1$; first ''quasiequilibrium window,'' $1.1<G<1.3$, and so on, until disintegration and unification of the object systems.

The system of object process classifiers has a whole range of important useful properties. These include a prognostic property which can predict new effects and give the characteristics of new, as yet unidentified, branches of science.

By way of example, the wide range of anomalous effects, structural transition effects, and in particular structural transitions of fields and ''quasiequilibrium window'' effects can be cited.

The principle of dynamic correspondence and object process classifiers can be used to characterize the synergetics and superhydrodynamics of a many-nucleon nucleus, macromolecules, field, and so on.

4. Let us examine a realization of the principle of dynamic correspondence in the form of laws governing the functional form of the reaction and the magnitude of the measure of action or the degree of nonequilibrium.

The most general form of the macroscopic reaction is given by the determining relations and the operator solution of the superhydrodynamics equations[8]

$$J_n=K_n[G], \quad R=R[G,\Pi], \tag{3}$$

where J_n are the fluxes, K_n and R are the functional operators of the susceptibility and the reaction (nonlinear, nonlocal, delayed).

In order to identify the form of (3), it is advisable to distinguish the ranges $G<0.2$; $G_a<0.2$, $T,L>0.3$; $T,L<0.3$, $0.3<G_a<1$ (G_a is the measure of active action).

In the first range (weak nonequilibrium), the main dependences are described by the linear relations

$$J_n\simeq\sum_m K_{nm}G_m, \quad K_{nm}=\left(\frac{\delta J_n}{\delta G_m}\right)_{G=0},$$

$$R\simeq\sum_m R_m G_m, \tag{4}$$

K_{nm} and R_m are the coefficients of susceptibility and reaction. These relations are suitable for any systems, except in cases of an unstable initial state (structural transition regime) or resonance reaction. For the case of a threshold reaction of the system (switching, photoeffect), it is sufficient to add a constant to the relations (4).

For the second range the fluxes and the reaction have the form of linear space-time functionals

$$J_n=\sum_m \int dt'd\mathbf{x}' K_{nm}(t-t',\mathbf{x}-\mathbf{x}')G_{m0}(t',\mathbf{x}'),\ldots \tag{5}$$

Similar dependences in the complete range of scale measures T_0 and L_0 for gases were given in Ref. 8.

The main dependences in the third range have the form of the nonlinear functions

$$J_n=K_n(G), \quad R=R(G,\Pi). \tag{6}$$

We shall subsequently analyze this case for the structural transition reaction.

For a wide range of G it is advisable to use the principle of dynamic correspondences for the determining relations, having expressed these in the partially expanded interpolation form

$$J_n[G]=\sum_{l,s,m}\int_0^t dt'\int d\mathbf{x}'\varphi^{ls}_{nm}(\Delta t,\Delta\mathbf{x};G,G') \times\exp\left[-T^s_{nm}\left(\frac{|\Delta t|}{\tau^s_{nm}(G')}\right)-L^l_{nm}\left(\frac{|\Delta\mathbf{x}|}{\lambda^l_{nm}(G')}\right)\right]G'_m, \tag{7}$$

where $\Delta t=t-t'$, $\Delta\mathbf{x}=\mathbf{x}-\mathbf{x}'$, $G'\neq G(t',\mathbf{x}')$; φ, L, and T are functions whose behavior may be indicated for low and high values of the arguments. This expression of the kinetic laws is consistent with the general form and is designed to construct semiphenomenological theories. It has been effectively used for various systems (plasma, polymers, low-density gas).

5. Let us now analyze an analytic model of the structural transition reaction (for the case (6)) which substantially improves the initial description[5] and for which the fundamental quantity $\Phi(G)$ has the form

$$\frac{d\Phi}{dG}=\frac{(G-G_1)(G-G_2)}{\alpha^2(G-G_3)^2+\gamma^2}, \tag{8}$$

$G_{1,2,3}>0$, where $G_{1,2}$ are the maximum and minimum points, and G_3, α, and γ are the structural transition parameters, determined experimentally or from the kinetic model.

The solution of Eq. (8) with allowance for the condition $\Phi(0)=0$ has the form

$$\alpha^2\Phi=G+(G_{31}G_{32}-\epsilon^2)\frac{1}{\epsilon}\left[\tan^{-1}\left(\frac{G-G_3}{\epsilon}\right)+\tan^{-1}\left(\frac{G_3}{\epsilon}\right)\right] +\frac{1}{2}(G_{31}+G_{32})\ln\left(\frac{(G-G_3)^2+\epsilon^2}{G_3^2+\epsilon^2}\right), \tag{9}$$

$G_{ij}=G_i-G_j$, $\epsilon=\gamma/\alpha$.

Let us use the model (9) to describe the structural transition taking place when a domain wall moves in a magnetic field.[11] Using the condition for normalization of the quantities relative to the onset of the structural phase transition, $\Phi(1)=1$ and taking into account the threshold G_c at which the motion begins, according to the data given by Chetkov *et al.*[11] and setting $\alpha^2\Phi=V$, we obtain

$$\overline{G}=G-G_c, \quad V(\overline{G}_2=1.37)=0.48, \quad V(\overline{G}_3=1.09)=0.77,$$

$$\epsilon=0.35, \quad \max V'\simeq V'\left(\frac{\overline{G}_1+\overline{G}_2}{2}\right)=0.3. \tag{10}$$

Model (9) was used for various structural transitions: an arc discharge (Ref. 12, p. 277), sound damping with increasing temperature in amorphous selenium (Ref. 13, p. 242): an abrupt decrease—analog of superfluidity; anomalous photoconductivity (Ref. 14, p. 162); a flash of cold flame (Ref. 15, p. 212); flame propagation with a flash (Ref. 16, p. 250); and various biological processes (Ref. 6, pp. 77, 138, 156, 233, 249, and 284).

The wide range of triggering behavior in living systems undoubtedly indicates that in general, mechanisms of vital activity are based on structural transitions. This conclusion explains much in biological processes from a physics point of view.

On examining the results of an analysis of chemical reactions by potentiometric and spectrophotometric titration, we observe that the dependence (9) is generally observed at stages with an active transition state. This observation suggests a promising approach to the overall description of a wide range of reactions which generalizes the Semenov theory of chain reactions.

[1] G. E. Skvortsov, Pis'ma Zh. Tekh. Fiz. **16**(17), 15 (1990) [Sov. Tech. Phys. Lett. **16**, 647 (1990)].
[2] G. E. Skvortsov, Pis'ma Zh. Tekh. Fiz. **23**(6), 85 (1997) [Tech. Phys. Lett. **23**, 246 (1997)].
[3] G. E. Skvortsov, Pis'ma Zh. Tekh. Fiz. **23**(7), 23 (1997) [Tech. Phys. Lett. **23**, 261 (1997)].
[4] G. E. Skvortsov, Pis'ma Zh. Tekh. Fiz. **23**(10), 17 (1997) [Tech. Phys. Lett. **23**, 383 (1997)].
[5] G. E. Skvortsov, Pis'ma Zh. Tekh. Fiz. **24**(3), 80 (1998) [Tech. Phys. Lett. **24**, 117 (1998)].
[6] In *Living Systems Exposed to External Influence* [in Russian], St. Petersburg, (1992), 440 pp.
[7] S. S. Kutateladze, *Analysis of Similarity and Physical Models* [in Russian], Nauka, Leningrad (1986), 293 pp.
[8] G. E. Skvortsov, Zh. Éksp. Teor. Fiz. **68**, 956 (1975) [Sov. Phys. JETP **41**, 473 (1975)]; Vestn. Leningr. Gos. Univ. **13**, 94 (1979).
[9] S. E. Shnoll, *The Physicochemical Factors of Biological Evolution* (Academic Press, New York, 1981) [Russ. original, Nauka, Moscow, 1979, 262 pp.].
[10] G. E. Skvortsov, Pis'ma Zh. Tekh. Fiz. **23**(22), 7 (1997) [Tech. Phys. Lett. **23**, 861 (1997)].
[11] M. V. Chetkov, A. K. Zvezdin, S. N. Gadestskiĭ *et al.*, Zh. Éksp. Teor. Fiz. **94**(1), 269 (1988) [Sov. Phys. JETP **67**, 151 (1988)].
[12] V. I. Artemov, Yu. S. Levitan, O. A. Sinkevich, *Instabilities of Turbulence in a Low-Temperature Plasma* [in Russian], MÉI, Moscow (1994), 412 pp.
[13] U. Bushenau, in *Phase Transitions and Relaxation in Systems with Competing Energy Scales* (Academic Press, New York, 1993, 452 pp.).
[14] M. I. Korsunskiĭ, *Anomalous Photoconductivity*, Wiley, New York (1973); Russian orig, Moscow (1972), 192 pp.
[15] V. N. Kondrat'ev and E. E. Nikitin, *Chemical Processes in Gases* [in Russian], Moscow (1981), 262 pp.
[16] N. N. Semenov, *Chain Reactions* [in Russian], Moscow (1986), 534 pp.

Translated by R. M. Durham

Mechanism of field-enhanced self-sustaining secondary electron emission in porous dielectrics

P. M. Shikhaliev

A. F. Ioffe Physicotechnical Institute, St. Petersburg
(Submitted April 21, 1998)
Pis'ma Zh. Tekh. Fiz. **24**, 13–18 (October 12, 1998)

A model is proposed for field-enhanced self-sustaining electron emission in secondary-emission porous dielectrics. It is shown that the mechanism for the formation of primary electrons at the metal–porous dielectric interface is field emission from the metal, and the electric field of the required intensity for field emission is formed by redistribution of the field in the layer as a result of the avalanche formation of secondary electrons. © *1998 American Institute of Physics.* [S1063-7850(98)00310-3]

Porous materials made from dielectrics with a high coefficient of secondary electron emission are potentially useful as working media for various types of radiation detector[1–3] which use the phenomenon of field-enhanced secondary electron emission in porous dielectrics.

Unlike secondary electron emission from solid materials, in which slow secondary electrons are emitted only from within a thin surface layer at most hundreds of angstrom thick, in porous dielectrics the thickness of the layer from which slow secondary electrons are emitted reaches tens and hundreds of microns, and an electric field of 10^4–10^5 V/cm, which expels the slow electrons from the material, forms within these layers.[3–5] The role of the electric field is to balance the losses of the slow electrons due to scattering by phonons within the pore walls by accelerating these electrons inside the pore, thereby lowering their recombination probability. This type of emission (like the secondary electron emission from solid materials) has an almost instantaneous response—the emission appears and disappears at the times when the primary electron beam is switched on and off.[5]

When the field in a layer of porous dielectric increases above a certain critical value, the secondary emission current increases sharply and the coefficient of secondary electron emission may reach hundreds or thousands. An explanation of this effect was given in Refs. 5 and 6 as follows. In fairly strong electron fields the slow electron energy collected inside the pore is sufficient for impact ionization of the dielectric material and an avalanche-like increase in the density of the slow electrons in the porous layer parallel to the electric field. A characteristic feature of this type of emission is its slow response: after the primary electron beam has been switched off, the emission decreases very slowly and in some cases does not cease for many hours, i.e., it is self-sustaining.[5,6]

At present, no satisfactory model is available to explain this self-sustaining emission. In particular, the mechanism for transfer of electrons from the metal substrate to the bulk of the dielectric after its irradiation by primary electrons has not been fully clarified (in the presence of irradiation electron–hole transitions occur at the metal–dielectric interface; electron–hole pairs are excited by fast primary electrons.[1,5]) The most probable mechanism for this transfer is field emission from the metal into the dielectric in the absence of a primary electron beam, although the electric field needed to induce field emission should be two orders of magnitude higher than the field produced in the dielectric layer.[5,6]

Here it will be shown that the mechanism for transfer of electrons from the metal to a porous dielectric in the absence of primary electron beam is field emission from the metal. The field required for the field emission is formed by means of nonuniform redistribution of the potential within the porous layer as a result of an avalanche-like increase in the excitation density of the slow electrons. This is accompanied by increased conductivity of the material in the direction away from the metal substrate toward the surface of the porous layer and an increase in the field in the inner part of the layer (near the metal substrate).

Let us assume that a sample of porous material of thickness L on a metal substrate of thickness $\ll L$ is irradiated by a penetrating beam of primary electrons. We shall consider a longitudinal section of this layer of unit cross section (Fig. 1). The current i_0 flowing through this cross section does not depend on the coordinate x (current conservation law). Thus, it satisfies $dU(x)/dR(x)=i_0=\text{const}$, and we have $dR(x)=\rho(x)dx$, where $\rho(x)=1/e\mu n(x)$ is the resistivity of the material caused by the excitation of free secondary electrons in the layer, and μ and $n(x)$ are the mobility and density of the secondary electrons.

Thus, we find

$$\frac{dU}{dx}=\frac{i_0}{e\mu}\frac{1}{n(x)}. \tag{1}$$

It is known from the theory of secondary emission detectors that in an avalanche formation process, the electron density in the avalanche increases exponentially:[7,8]

$$n(x)=n_0\exp\left(\frac{x}{L}\ln K_0\right), \tag{2}$$

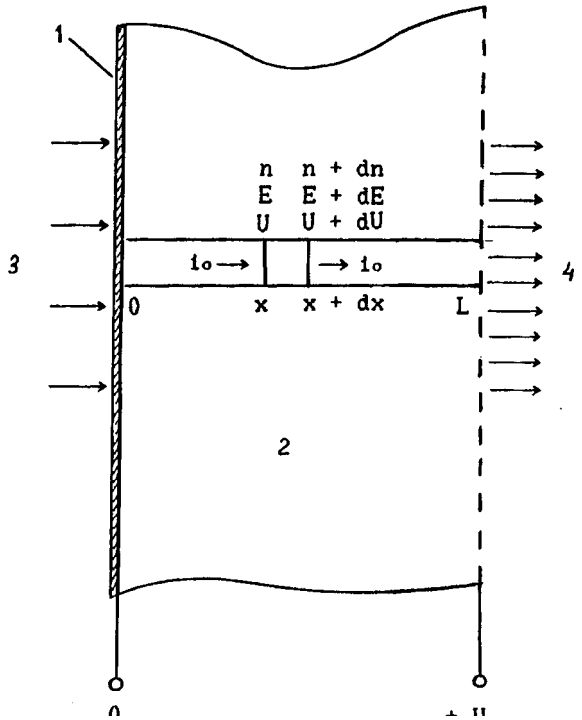

FIG. 1. Cross section of porous dielectric on metal substrate: *1*—metal, *2*—porous layer, *3*—primary electrons, and *4*—secondary electrons.

where we have written $n_0=n(0)$, K_0 is the coefficient of electron multiplication in the avalanche formation process when a potential difference $U_0>U_k$ is applied to the porous layer, and U_k is the critical potential difference at which the avalanche formation process begins. From Eq. (2) we obtain

$$\frac{dn}{dx}=\frac{\ln K_0}{L}n(x), \tag{3}$$

and K_0 can be approximated as

$$\ln K_0=A(U_0-U_k), \tag{4}$$

where A is a known constant. However, expressions (2) and (3) are valid for a linear potential distribution in the layer when the potential is $U(x)=U_0x/L$. Since the conductivity varies along the layer in the avalanche formation process, $U(x)$ is redistributed nonlinearly. In this case, for Eq. (3) to be valid $\ln K_0$ should be replaced by $\ln K_0'=A(U_0'-U_k)$, where $U_0'=(dU/dx)L$ (Ref. 9). Taking this into account, Eq. (3) now has the form

$$\frac{dn}{dx}=\frac{A}{L}\left(\frac{dU}{dx}L-U_k\right)n. \tag{5}$$

Equations (1) and (5) yield the system

$$\begin{cases}\dfrac{dU}{dx}=\dfrac{i_0}{e\mu}\dfrac{1}{n}\\[2ex] \dfrac{dn}{dx}=\dfrac{A}{L}\left(\dfrac{dU}{dx}L-U_k\right)n\end{cases} \tag{6}$$

with the boundary conditions $U(0)=0$, $U(L)=U_0$, and $n(0)=n_0$. The solutions of Eq. (6) with allowance for these boundary conditions are as follows:

$$\begin{aligned}U(x)&=\frac{1}{A}\ln\frac{\exp(AU_kx/L)-a}{1-a},\\ n(x)&=\frac{Li_0}{e\mu U_k}\frac{1-a\exp(-AU_kx/L)}{1-a},\\ E(x)&=\frac{dU}{dx}=\frac{U_k}{L}\frac{1}{1-a\exp(-AU_kx/L)},\end{aligned} \tag{7}$$

where $a=(\exp(AU_0)-\exp(AU_k))/(\exp(AU_0)-1)$.

It is easy to see from Eq. (7) that for $U_0=U_k$, $a=0$, and $U(x)=U_0x/L$, we obtain $E(x)=U_0/L=E_0$, $n(x)=i_0/e\mu E_0$, which corresponds to the condition for cessation of avalanche formation. For $U_0>U_k$ at the metal–porous layer interface ($x=0$) we have

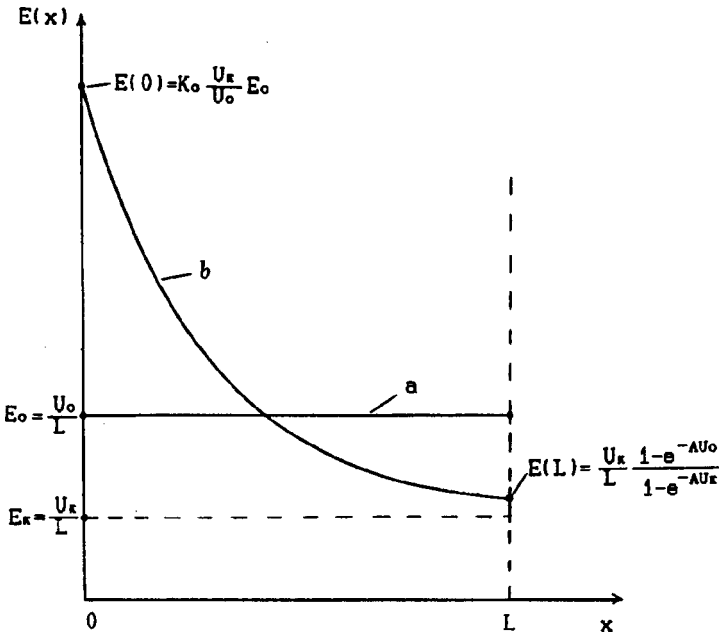

FIG. 2. Electric field distribution in porous layer before (a) and after initiation of primary electron beam (b).

$$E(0)=\frac{U_k}{L}\frac{1}{1-a}. \quad (8)$$

At the exit surface of the porous layer ($x=L$) we find:

$$E(L)=\frac{U_k}{L}\frac{1-\exp(-AU_0)}{1-\exp(-AU_k)},$$

$$n(L)=n_0\frac{1-a\exp(-AU_k)}{1-a}.$$

Allowing for Eq. (4) in Eq. (8), we find $E(0)=(U_k/U_0)K_0E_0$. For the typical values $K_0\approx 200$, $U_k/U_0\approx 0.5$ observed experimentally we obtain $E(0)=100(U_0/L)=100E_0$. Thus, if the potential difference at the porous layer exceeds the critical value, the electric field at the metal–porous layer interface may increase by two orders of magnitude after switching on the primary electron beam (Fig. 2). This field is quite sufficient to initiate field emission from the substrate. After the primary electron beam has been switched off, avalanche formation is initiated by the field electrons and becomes self-sustaining. The duration of this self-sustaining electron emission may be influenced by many factors. One possible reason for the gradual decrease in intensity and cessation of self-sustaining emission is the dissociation of dielectric molecules caused by electron impact which leads to degradation of the emission characteristics of the material.

In conclusion, the author is deeply grateful to B. A. Mamyrin for discussions of the material and valuable comments.

[1] J. Edgecumbe and E. L. Garvin, J. Appl. Phys. **37**, 3321 (1966).
[2] C. Chianelli, P. Ageron, J. P. Bouvet *et al.*, Nucl. Instrum. Methods Phys. Res. A **273**, 245 (1988).
[3] M. P. Lorikyan, Usp. Fiz. Nauk **165**, 1323 (1995).
[4] N. L. Yasnopol'skiĭ and A. É. Shabel'nikova, Fiz. Tverd. Tela. (Leningrad) **10**, 103 (1968). [Sov. Phys. Solid State **10**, 75 (1968)].
[5] N. L. Yasnopol'skiĭ, A. É. Shabel'nikova, A. P. Balashov, and N. S. Lozhkina, in *Research in Radio Engineering and Electronics*, Part 2 [in Russian], Moscow (1975), p. 67.
[6] I. M. Bronshteĭn and B. S. Fraĭman, *Secondary Electron Emission* [in Russian], Nauka, Moscow (1969), 408 pp.
[7] C. Loty, Acta Electron. **14**(1), 107 (1971).
[8] M. R. Aĭnbund and B. V. Polenov, *Secondary Electron Emission Multipliers and Their Applications* [in Russian], Énergoatomizdat, Moscow (1981).
[9] P. M. Shikhaliev, Nucl. Instrum. Methods Phys. Res. (1998) (in press).

Translated by R. M. Durham

Switching time of planar ferroelectric capacitors using strontium titanate and barium strontium titanate films

A. B. Kozyrev, O. I. Soldatenkov, and A. V. Ivanov

St. Petersburg Electrotechnical University
(Submitted March 27, 1998)
Pis'ma Zh. Tekh. Fiz. **24**, 19–25 (October 12, 1998)

A microstripe cavity was used to make microwave ($f \sim 10$ GHz) measurements of the time of variation of the permittivity of $SrTiO_3$ and $(Ba,Sr)TiO_3$ films exposed to unipolar video-frequency voltage pulses. It was shown that the permittivity of $SrTiO_3$ films varies over times less than 30 ns. For $(Ba,Sr)TiO_3$ films two characteristic times of variation of the permittivity were identified: a fast variation over times less than 30 ns and a slower variation, on the order of 20 μs. © *1998 American Institute of Physics.* [S1063-7850(98)00410-8]

The ferroelectric materials $SrTiO_3$ and $(Ba,Sr)TiO_3$ which possess high dielectric nonlinearity are attracting considerable interest among developers of microwave devices. It was shown that when bulk single-crystal and polycrystalline ferroelectrics are used as nonlinear elements of parametric amplifiers and harmonic oscillators, the permittivity of these materials varies under the action of a microwave sinusoidal signal over a time less than 10^{-11} s (Refs 1 and 2). Such a short relaxation time is attractive from the point of view of developing microwave control and switching devices (photoconverters, channel switches, tunable filters, and so on), which require high speed for controlling video-frequency voltage pulses.

In modern microelectronics, ferroelectric films are required to fabricate these devices and their properties may differ substantially from those of the bulk material. In particular, highly oriented strontium titanate ($SrTiO_3$) films demonstrate a nonmonotonic temperature dependence of the permittivity $\varepsilon(T)$ and increased microwave losses ($\tan\delta$) which differ from the microwave properties of the single crystals.[3–5] Thus, the response time of the permittivity of the films on exposure to a microwave signal and under the action of video-frequency voltage pulses requires further investigation. Here we describe the method and report results of an experimental investigation of the time of variation of the permittivity of $SrTiO_3$ and $(Ba,Sr)TiO_3$ films under the application of controlling unipolar video-frequency voltage pulses.

Preferentially (100)-oriented $SrTiO_3$ films of thickness $h \cong 0.7$ μm were prepared by magnetron sputtering on Al_2O_3 substrates. Polycrystalline films of $(Ba,Sr)TiO_3$ (60% Ba, 40% Sr), of thickness $h \cong 4$ μm were fabricated by ceramic technology on MgO substrates. These films were described in more detail in Refs. 3 and 5. The samples for the investigations were planar ferroelectric capacitors fabricated using these films (Fig. 1a). The controllability of the capacitors ($K = C_{U=0V}/C_{(U\max)}$) using $SrTiO_3$ (gap width $g = 10$ μm, gap length $l = 0.5$ mm) and $(Ba,Sr)TiO_3$ films ($g = 30$ μm, $l = 1$ mm) reaches $K \cong 2$ when the dc electric field strength in the gap is increased to around 10 V/μm.

The time of variation of the permittivity of the ferroelectric capacitor as a result of interaction of a pulsed control voltage was measured by determining the rate of frequency tuning of the amplitude-frequency characteristic of a microstripe cavity incorporating the capacitor being studied. The time variation of a weak (compared with the control voltage pulse) microwave signal passing through the cavity with the ferroelectric capacitor connected can be used to determine the response time of the ferroelectric film to the pulsed action.

The topology of the microstripe measurement circuit, including the cavity with the planar capacitor is shown in Fig. 1a. The planar ferroelectric capacitor is inserted in a gap in the microstripe line of the cavity near its short-circuited end. At the other end of the cavity no-load conditions are established. The cavity is connected to the microwave circuit via capacitive gaps which provide the required coupling between the cavity and the microwave circuits and also protect the microwave circuit from the action of the control voltage. The control voltage pulse is applied to the ferroelectric capacitor via low-pass filters with a cutoff frequency ~ 2 GHz. The low-pass filters are connected to the cavity microstripe near points of zero microwave electric field which can reduce the influence of the control circuits on the amplitude-frequency characteristic of the cavity.

The change in the capacitance of the capacitor when a dc control voltage $C(U_b)$ is applied changes the resonant frequency f_0 of the cavity (Fig. 1b) is given by

$$2\pi Z_0 f_0\, C(U_b) = \tan\left(\frac{2\pi}{c}\sqrt{\varepsilon_{\text{eff}}}\, f_0\, l_{\text{eff}}\right), \tag{1}$$

where Z_0 and ε_{eff} are the wave impedance and the effective permittivity of the cavity microstripe line, l_{eff} is the effective cavity length, and $c = 3\times 10^8$ m/s is the velocity of light. When the control voltage pulse is applied to the capacitor, the amplitude-frequency characteristic of the cavity undergoes a frequency shift which leads to a change in the transmission coefficient S_{21} at a fixed microwave signal frequency (Fig. 1b). A comparison between the applied voltage video-frequency pulse and the detected microwave response

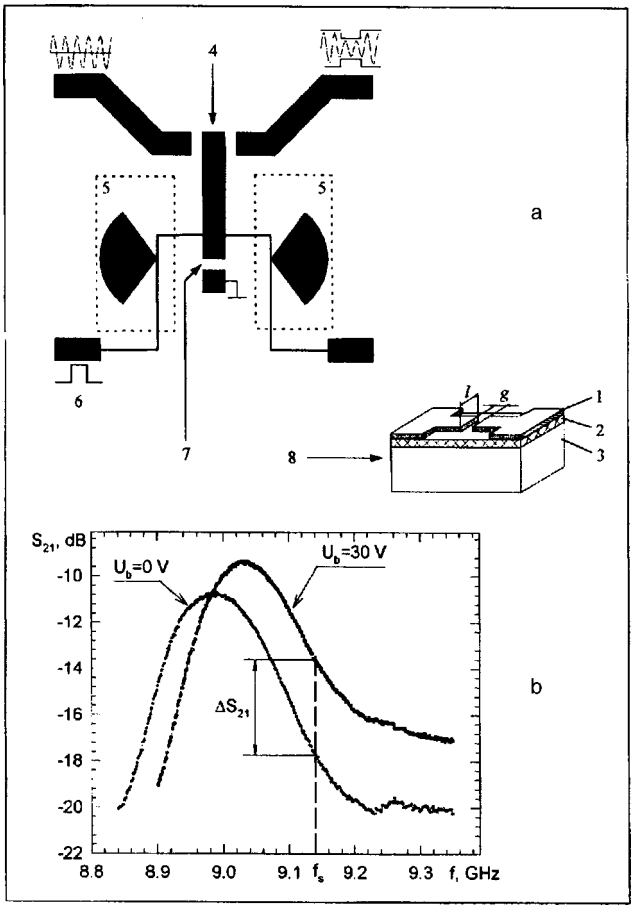

FIG. 1. a — Simplified layout of microstripe microwave system to measure switching time of planar ferroelectric capacitors: *4* — microstripe cavity, *5* — low-pass filters, *6* — circuit to supply control pulse, *7* — connection point for planar capacitor, *8* — planar ferroelectric capacitor (*1* — copper electrodes, *2* — $SrTiO_3$ or $(Ba,Sr)TiO_3$ film, *3* — Al_2O_3 or MgO substrate). b — Change in the amplitude–frequency characteristic of the cavity when a dc control voltage is applied to the ferroelectric capacitor; ΔS_{21} — change in the transmission coefficient at fixed microwave signal frequency (f_s).

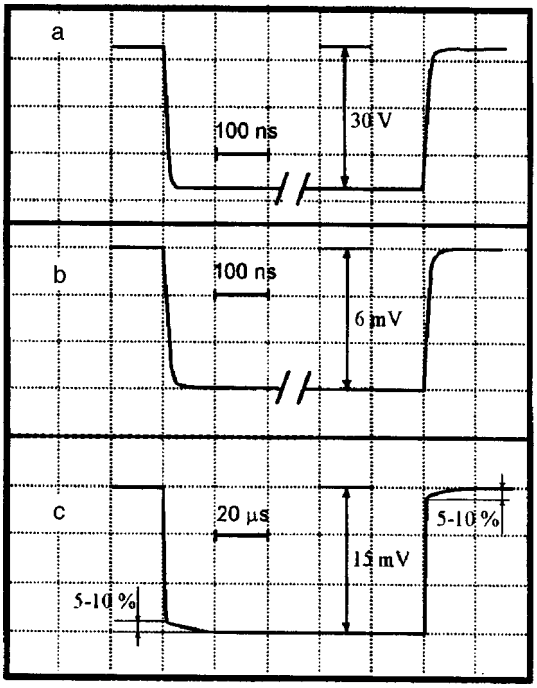

FIG. 2. Oscilloscope traces showing switching time of $SrTiO_3$ (b) and $(Ba,Sr)TiO_3$ (c) capacitors under the action of a 100 μs control pulse (a). The scale of the pulse length of the microwave response for the $SrTiO_3$ and $(Ba,Sr)TiO_3$ elements is different to reveal the ''slow'' ($\sim$20 μs) relaxation mechanism.

pulse observed on the screen of an oscilloscope can reveal the cavity tuning time when the ferroelectric capacitor is connected.

The time of the transition processes in the resonant circuit and the circuit distortion of the control voltage pulses when these are applied to the capacitor is less than 1 ns, which means that we can reliably determine the relaxation times t_r of the ferroelectric element provided that $t_r \geqslant 10$ ns. For the experiments we used a voltage pulse generator which delivered rectangular unipolar video-frequency pulses of up to 60 V with lengths between 0.1 μs and 10 ms, and a rise time of 30 ns. Thus, the determination of the response time of the ferroelectric film to the voltage pulse was limited only by the speed of the generator, i.e., by the $\sim$30 ns rise time of the control pulse.

For all the $SrTiO_3$ capacitors studied over the entire range of amplitude and length of the control video-frequency pulses, the envelope of the microwave signal was identical to the profile of the control pulse. The rise and decay times of the detected microwave pulse were the same as the rise time of the control pulse, $\sim$30 ns, which indicates that the permittivity response time of an $SrTiO_3$ capacitor is $t_r \leqslant 30$ ns. By way of example, Fig. 2a shows oscilloscope traces of the control voltage pulse (pulse length 100 μs, rise time $t_f \cong 30$ ns, and amplitude $U_m = 30$ V) and the detected microwave signal pulse (Fig. 2b) after passing through the cavity with an $SrTiO_3$ capacitor.

For the cavity with a $(Ba,Sr)TiO_3$ capacitor the envelope of the microwave signal (Fig. 2c) indicates that there are two different mechanisms responsible for the change in the permittivity of the $(Ba,Sr)TiO_3$ film under the action of the control voltage pulse: a fast variation in the permittivity over a time less than the rise time of the control pulse ($\sim$30 ns) and a slower variation with a response time of the order of 20 μs. The slow variation in the amplitude of the detected microwave signal was less than 5–10% of the total amplitude of this pulse.

We note that for the $SrTiO_3$ capacitors the change in the transmission coefficient ΔS_{21} of the microwave signal under the action of video pulses of amplitude U_m for times $t \geqslant t_f \cong 30$ ns agreed with the value of ΔS_{21} observed when a fixed bias $U_b = U_m$ was applied to the capacitor. A similar effect was observed for $(Ba,Sr)TiO_3$ elements for $t \geqslant 20\mu$s. Thus, for times exceeding those specified, the same change in the capacitance was observed for both types of control actions. This indicates that there are no other slower relaxation mechanisms and means that Eq. (1) and the capacitance–voltage characteristics obtained for a fixed bias $C(U_b)$ can be used to determine the shift of the resonant frequency (the controllability of the devices) under pulsed action.

Studies carried ourt using the present method enabled us to conclude that the total change in the permittivity of $SrTiO_3$ films exposed to pulsed action takes place over times $\leqslant 30$ ns. For $(Ba,Sr)TiO_3$ capacitors a slower change in the permittivity was also observed with a relaxation time of the order of 20 μs which, however, is no more than 10% of the total change in ε. The response time of planar $SrTiO_3$ and $(Ba,Sr)TiO_3$ capacitors and the change in their capacitance under the action of control voltage pulses are quite acceptable for these to be used as fast elements of tunable microwave devices.

[1] *Ferroelectrics in Microwave Technology*, edited by O. G. Vendik [in Russian], Sovetskoe Radio, Moscow (1979), 272 pp.
[2] M. DiDomenico, D. A. Johnson, and R. H. Pantell, J. Appl. Phys. **33**, 1697 (1962).
[3] A. B. Kozyrev, T. B. Samoilova, O. I. Soldatenkov *et al.*, in *Proceedings of the 27th European Microwave Conference (EMC97)*, Jerusalem, Israel, Vol. 2, p. 1020 (1997).
[4] D. Galt, J. Proce, J. Beall, and T. Harvey, IEEE Trans. Appl. Supercond. **5**, 2575 (1995).
[5] A. B. Kozyrev, V. N. Keis, G. A. Koepf *et al.*, Microelectron. Eng. **29**, 257 (1995).

Translated by R. M. Durham

Modified method of plasma-enhanced chemical vapor deposition of nanocrystalline silicon

V. G. Golubev, A. V. Medvedev, A. B. Pevtsov, and N. A. Feoktistov

A. F. Ioffe Physicotechnical Institute, Russian Academy of Sciences, St. Petersburg
(Submitted April 21, 1998)
Pis'ma Zh. Tekh. Fiz. **24**, 26–30 (October 12, 1998)

A modified plasma-enhanced chemical vapor deposition technology is developed for nanocrystalline Si which combines the standard rf glow discharge method and the hollow-cathode discharge method in a single process cycle. The volume fraction of nanocrystallites varied monotonically along the layer, whereas their size remained constant. The electrical and optical characteristics of these films were investigated.
[S1063-7850(98)00510-2]

Thin silicon films with a mixed amorphous crystalline phase composition and crystallite sizes in the range 20–100 Å have recently attracted close attention in connection with studies of their properties associated with quantum-level effects[1] and potential practical applications. The synthesized materials comprise a system of crystalline silicon quantum dots whose volume fraction may exceed 50%, while the nanocrystal–amorphous matrix interface is a heterojunction with tunneling through the insulator.[2] From the point of view of technical applications, it should be noted that the conductivity may be increased to values exceeding 1 S/cm by doping,[3,4] thus improving the current–voltage characteristics of $p-i-n$ structures using these layers. These materials may also be used as wide-gap windows in photoconverters,[5] and photo- and electroluminescence has been observed in the visible range at room temperature.[6,7]

It is undoubtedly of interest to determine how the electrical and optical characteristics of nanocrystalline silicon (nc-Si) are related to the sizes and volume fraction of nanocrystallites and also to the properties of the heterojunctions between the nanocrystallites and the amorphous matrix. Such investigations are usually carried out using nc-Si prepared using different technologies or in a series of similar technological processes. In these cases, both the sizes and volume fraction of nanocrystallites usually vary. Thus, by fabricating layers with a fixed size and varying volume fraction of crystallites in a single deposition process, it would be possible to draw more reliable conclusions as to how these parameters influence the electrical, optical, and radiative properties of nc-Si. To solve this problem we proposed a modified version of plasma-enhanced chemical vapor deposition (PE CVD) which can produce films containing crystallites of a given size whose volume fraction varies monotonically along the layer in an amorphous matrix.

Hydrogenated nc-Si was prepared by PE CVD under conditions of strongly hydrogen-diluted silane. The method differed from the standard technique[8] by incorporating two types of rf discharge in a single technological process. This was achieved by making a hole at the center of the rf electrode (Fig. 1) near which a self-sustained high-intensity discharge was struck when the rf voltage exceeded a threshold, maintaining a homogeneous rf discharge over the entire electrode area. In this way a hollow cathode discharge[9] in which the silane underwent more vigorous dissociation and a normal rf discharge were combined in the diode system.

The cylindrical heated electrode on which the circular substrate was located was grounded with respect to the rf component and a fixed negative bias of 0–300 V could be applied to it. The process parameters were as follows: silane concentration in hydrogen 2–6%, working mixture pressure 0.3–1 Torr, flow rate 10–30 sccm, temperature 100–300 °C, specific rf power 0.3–3 W/cm^2, and frequency 17 MHz.

A particular combination of process parameters and a fairly large-diameter substrate (around 75 mm) could produce a radially dependent volume fraction of crystallites in the deposited film in a single deposition process. The volume fraction of crystallites increased from 0 to 25% with increasing distance from the substrate. The size of the crystallites varied by no less than 5%. This method of fabricating nc-Si allowed us to reliably determine the dependence of the electrical and optical properties of the films on the volume fraction of crystallites of the same size contained in them.

Nanocrystalline Si was deposited on circular substrates of fused quartz and crystalline silicon. Laser interferometry with angular incidence of the beam on the substrate was used for in situ monitoring of the growth rate and optical parameters. The growth rate of the films was 0.3–1.0 Å/s for a homogeneous discharge. When the films were deposited with a homogeneous discharge and a hollow-cathode discharge burning simultaneously, the growth rate increased to 2 Å/s.

The volume fraction and the size of the nanocrystallites were determined by a numerical analysis of the Raman scattering spectra allowing for the spatial confinement of the phonons.[10] Measurements were also made of the conductivity and optical transmission of the layers. The hydrogen content, determined by analyzing the infrared transmission spectra, was 17–37% depending on the deposition conditions.

A comb of 3×1 mm metal electrodes, each around 1 mm apart, was deposited along the diameter of the substrate to measure the electrical conductivity (see Fig. 1). Measure-

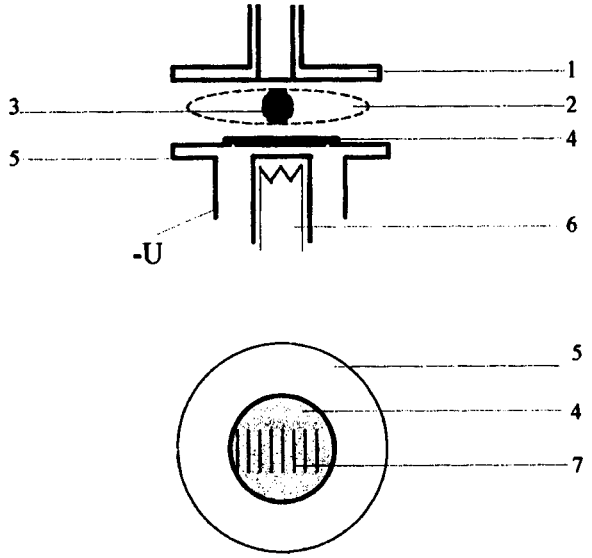

FIG. 1. Schematic of modified plasma-enhanced chemical vapor deposition of nanocrystalline silicon films: *1*—rf electrode with hole *2*— homogeneous discharge burning zone, *3*—high-intensity discharge burning zone, *4*—substrate, *5*—heated electrode, grounded with respect to rf component, *6*—heater, *7*—comb of metal electrodes. The position of the substrate on the heated electrode is shown in the lower diagram.

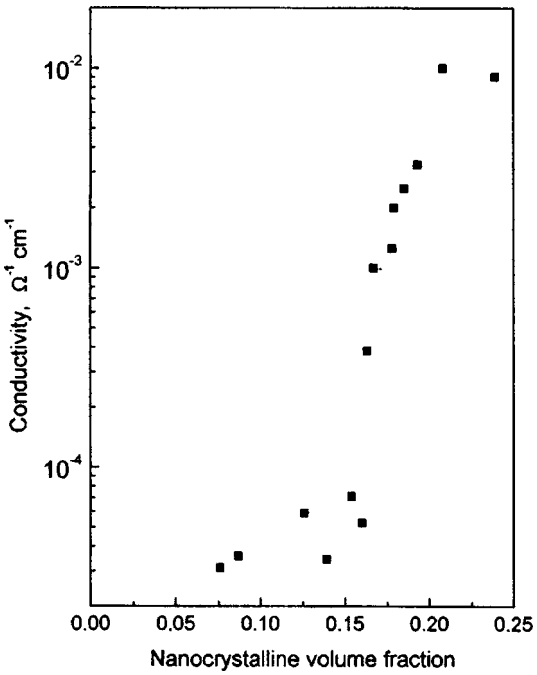

FIG. 2. Conductivity of nanocrystalline films versus volume fraction of nanocrystallites for sample containing ~40 Å crystallites.

ments of the optical transmission and the Raman spectra were made between neighboring electrodes. Figure 2 gives the conductivity as a function of the volume fraction of silicon nanocrystallites of (40 ± 2) Å in the radial direction along the layer. An abrupt increase in conductivity was observed when the volume fraction of crystallites exceeded $\simeq 16\%$. This result may be interpreted as the formation of a percolation threshold in the system of conducting silicon nanocrystallites implanted into the insulating amorphous matrix.[10]

The optical band gap (E_g) was determined by analyzing the absorption spectra of the films using the Tauc formula $\alpha \sim (E-E_g)^2$. It was observed that E_g increased from 1.8 eV at the center of the substrate to 2.0 eV at the edge where the volume fraction of nanocrystallites exceeded 20%.

To sum up, we have developed a modified PE CVD process which can be used to deposit, in a single cycle, a film containing a volume fraction of silicon nanocrystallites of fixed size in an amorphous matrix, which varies monotonically along the layer. The electrical and optical characteristics of the nanocrystalline silicon were investigated as a function of the volume fraction of crystallites.

This work was partially supported by the Russian Fund for Fundamental Research (Project No. 98-02-17350) and by the INCO-COPERNICUS Program (Grant No. PL97-8104).

[1] H. Takagi, H. Ogawa, Y. Yamazaki, and T. Nakagiri, Appl. Phys. Lett. **56**, 2379 (1990).
[2] G. Y. Hui, R. F. O'Connell, Y. L. He, and M. B. Yu, J. Appl. Phys. **78**, 3945 (1995).
[3] S. S. He, M. J. Williams, D. J. Stephens, and G. Lucovsky, J. Non-Cryst. Solids **164–166**, 731 (1993).
[4] Y. He, C. Yin, G. Cheng, L. Wang, X. Liu, and G. Y. Hu, J. Appl. Phys. **75**, 797 (1994).
[5] R. E. Hollingworth, P. K. Bhat, and A. Madan, J. Non-Cryst. Solids **97–98**, 309 (1987).
[6] X. Liu, S. Tong, L. Wang, G. Chen, and X. Bao, J. Appl. Phys. **78**, 6193 (1995).
[7] S. Tong, X. Liu, L. Wang, F. Yan, and X. Bao, Appl. Phys. Lett. **69**, 596 (1996).
[8] T. Hamasaki, H. Kurata, M. Hirose, and Y. Osaka, Appl. Phys. Lett. **37**, 1084 (1980).
[9] C. M. Horwitz, S. Boronkay, M. Gross, and K. Davies, J. Vac. Sci. Technol. A **6**, 1837 (1988).
[10] V. G. Golubev, V. Yu. Davydov, A. V. Medvedev, A. B. Pevtsov, and N. A. Feoktistov, Fiz. Tverd. Tela. (St. Petersburg) **39**, 1348 (1997) [Phys. Solid State **39**, 1197 (1997)].

Translated by R. M. Durham

Decay dynamics of superheated states of liquid metals

A. P. Kubyshkin, F. Kh. Mirzoev, and V. Ya. Panchenko

Industrial Laser Research Center, Russian Academy of Sciences, Shatura
(Submitted June 2, 1997)
Pis'ma Zh. Tekh. Fiz. **24**, 31–35 (October 12, 1998)

An analysis is made of a kinetic model for the decay of the superheated state of liquid metals formed under the action of a nanosecond laser pulse. It is shown that the temperature varies exponentially with time and the characteristic relaxation time is determined.
 [S1063-7850(98)00610-7]

Studies of the physical properties of materials in metastable states are of particular importance in the problem of phase transitions. Metastable states may be formed as a result of first-order phase transitions such as evaporation, condensation, crystallization, and so on.[1] In the metastable state, various thermodynamic characteristics such as the compressibility, specific heat, and coefficient of thermal expansion[2] undergo changes which may be of interest for the development of new materials. Existing sources of high-power laser radiation delivering pulses with variable time parameters (down to femtosecond scales) can now act on metals, converting them to strongly overheated (metastable) states[2] previously unattainable by conventional methods.[1] Karabutov *et al.*[3] showed that mercury may be superheated by nanosecond laser pulses on a mechanically loaded surface. The material is converted to the metastable state as a result of the appreciable dynamic dependence of the temperature and pressure variation during and after the laser pulse. It was shown experimentally that during decay of the superheated state of mercury, the temperature varies exponentially with time and the characteristic relaxation time is $\tau_T = 70$ ns.

The most probable mechanism for the decay of these states in a liquid metal is the fluctuational formation and growth of competing phase nuclei in the layer of superheated metal. Here we consider a kinetic model of the decay of superheated metal states which can be used to study the time dependence of the temperature of superheated liquids and also the main characteristics of the phase transition (nucleation rate, density of nuclei).

The nucleation rate (J) depends on the degree of superheating $\theta = (T - T_0)/T_0$, which varies with time as a result of absorption of the latent heat of the phase transition (Q) accompanying the formation of new-phase nuclei. The heat balance equation in this case may be written in the form

$$\theta = \frac{1}{\rho c T_0}\int_0^t S(t')dt' - \frac{4\pi Q}{3\rho c T_0 \Omega}\int_0^\infty r^3 f(r,t)dr, \qquad (1)$$

where ρ is the density, c is the specific heat, Ω is the volume of a single particle, and $f(r,t)$ is the distribution of stable centers as a function of the radius r at time t.

The function $f(r,t)$ satisfies the equations

$$\frac{\partial f}{\partial t} + \frac{\partial}{\partial r}(Vf) = 0, \quad f(r,0) = 0, \quad f(r_0,t) = \frac{J(\theta(t))}{V(r)} (r = r_0), \qquad (2)$$

where $V(r) = dr/dt$ is the growth rate of the centers and r_0 is the minimum radius. Since the time taken to establish a steady-state distribution of near-critical nuclei is far shorter than the characteristic time $\theta(t)$, the function $J(t)$ is quasi-steady, i.e., it is determined by the instantaneous superheating $J(t) = J(\theta(t))$.

The growth rate is $V = \mu\theta(t)/r^n$ (Ref. 4), where n is the growth index of the nuclei and μ is the kinetic coefficient ($\mu = 10^{-8}$ cm^3/s) ($n = 0$ if nuclei growth is limited by the kinetics of interphase transitions; $n = 2$ when layer-by-layer growth predominates).

The nucleation rate is given by

$$J = N_1 B \exp(-U_c/kT), \qquad (3)$$

where N_1 is the number of particles per unit volume of the metastable phase, $U_c = 4\pi\gamma r_c^2/3$ is the height of the activation barrier, $r_c = 2\gamma\Omega/Q\theta$ is the critical radius, γ is the surface tension, and $B = \Omega d\sqrt{\gamma kT}\exp(-W/kT)/2\pi r_c^2 h$ (h is Planck's constant, W is the activation energy of viscous flow, and d is the interatomic distance).[4]

From Eqs. (1)–(3) we have

$$J(\theta) = J_0 \exp[-G(\theta)]. \qquad (4)$$

Here we have

$$J_0 = N_1 d(Q\theta)^2\sqrt{(1+\theta)kT_0} \times \exp[-W/kT_0(1+\theta)]/8\pi\gamma^{3/2}\Omega h$$

and

$$G(\theta) = 16\pi\gamma^3\Omega^2/3Q^2kT_0\theta^2(\theta+1).$$

We introduce the new variables $\zeta = \int_{r_0}^r r^n dr$ and $z(t) = \mu\int_0^t \theta(t')dt'$. Equation (2) can then be written in the form

$$\frac{\partial g}{\partial z} + \frac{\partial g}{\partial \zeta} = 0, \qquad (5)$$

where $g(r) = f(r)/r^n$. The solution (5) clearly only depends on one variable, i.e.,

$$g(r,t) = g(x) = g(z(t) - \zeta(t)), \quad g(x) - \frac{J(\theta(x))}{\mu\theta(x)}. \qquad (6)$$

Here we have written $\theta(x) \equiv \theta(t(x))$.

As in Ref. 5, we expand the function in the argument of the exponential function (4) as a Taylor series near the initial superheating θ_0: $G = G_0 + G'(\theta_0)(\theta - \theta_0) + \ldots$. Neglecting the dependence of J_0 on θ compared with the very strong exponential dependence of J on θ and assuming that in the nucleation region $G'(\theta_0)(\theta - \theta_0) < 1$, we have from Eq. (4)

$$g(x) \approx g_0 \exp[-\alpha\varepsilon(x)],$$

$$g_0 = J_0(\theta_0)(\mu\theta_0)^{-1} \exp[-G(\theta_0)], \tag{7}$$

where $\varepsilon = 1 - \theta/\theta_0$ is the relative change in the superheating and $\alpha = -\theta_0 G'(\theta_0)$.

Let us assume that the superheating is created instantaneously $S(t) = S_0\delta(t)$, $S_0 = \rho c T_0 \theta_0$ (θ_0 is the initial superheating), and Eq. (1) gives

$$\theta(t) = \theta_0\left(1 - \frac{4\pi Q}{3\rho c T_0 \theta_0 \Omega}\int_0^\infty r^3 f(r,t)\,dr\right). \tag{8}$$

Substituting expression (7) into Eq. (8), we obtain an equation for the superheating dynamics:

$$\varepsilon(z) = \beta\int_0^z (z-\xi)^m \exp[-\alpha\varepsilon(\xi)]\,d\xi,$$

$$\beta = 4\pi(n+1)^m Q J_0/3\mu\rho c\,\theta_0^2 \Omega T_0, \quad m = 3/(n+1). \tag{9}$$

To derive Eq. (9) we assume that nuclei of dimensions $r > r_0$ make a significant contribution to the change in the superheating.

After substituting $\varepsilon(z) = \alpha^{-1} Z_m(z/z_c)$, where $z_c = [(m+1)/\alpha\beta]^{1/(m+1)}$, we have from Eq. (9)

$$Z_m(z) = (m+1)\int_0^z (z-\xi)^m \exp[-Z_m(\xi)]\,d\xi. \tag{10}$$

By iterating about $Z_m^0 = 0$ as a zeroth approximation, we find

$$Z_m^{(1)} = z^{m+1}, \quad Z_m^{(2)} = (m+1)\int_0^z (z-\xi)^m \exp(-\xi^{m+1})\,d\xi \tag{11}$$

and so on. We note that the iterations (11) converge fairly rapidly toward a single solution of Eq. (10) and thus we can confine ourselves to the first two iterations.

We shall now determine the function $z(t)$. Taking into account the definition of $\varepsilon(z)$, we have the following equation for $z(t)$:

$$\frac{dz}{dt} = \frac{\mu\theta_0}{\alpha}[\alpha - Z_m(z/z_0)]. \tag{12}$$

For short times we than have $z(t) \approx \mu\theta_0 t$. For large t, using the expansion $Z_m(z) \approx Z_m(z_0) + Z_m'(z_0)(z - z_0)$, where z_0 is the solution of $Z_m(z_0) = \alpha$, we obtain $z(t) = z_0[1 - \exp \times(-t/\tau_T)]$. Thus, confining ourselves for simplicity to the first iteration for $Z_m^{(1)}$, we obtain for the superheating temperature $\theta(t) = \theta_0 \exp(-t/\tau_T)$. The nucleation rate is $J(t) = J_0 \exp(-t/\tau_N)^{m+1}$, where $\tau_T = \tau_N(\alpha^{1/(1+m)}/m)$, $\tau_N = [(m+1)/\alpha\beta]^{1/(1+m)}/\mu\theta_0$ is the characteristic relaxation time of the superheated state, and τ_N is the duration of nucleation. Thus, we have shown that the temperature of the superheated liquid metal relaxes exponentially to the equilibrium value. For typical parameters of liquid mercury ($\rho = 14\,\mathrm{g/cm^3}$, $\Omega = 2\times10^{-22}\,\mathrm{cm^3}$, $W = 10^{-13}\,\mathrm{erg}$, $\gamma = 0.5\,\mathrm{erg/cm^2}$, $J = 10^7\,\mathrm{cm^{-3}\cdot s^{-1}}$, $N = 4\times10^{22}\,\mathrm{cm^3}$, $\alpha \sim 10^4$, $m = 1$) we obtain the characteristic relaxation time $\tau_T \sim 80\,\mathrm{ns}$, which is broadly consistent with the experimental data.[3] Note that the characteristic nucleation time is $\tau_N = 0.8\,\mathrm{ns}$.

This work was supported financially by the Russian Fund for Fundamental Research (Grant No. 96-02-18988a).

[1] V. G. Boĭko, Kh. I. Mogel', V. M. Sysoev, and A. V. Chalyĭ, Usp. Fiz. Nauk **161**(2), 77 (1990) [Sov. Phys. Usp. **34**, 141 (1990)].
[2] F. V. Bunkin and A. M. Tribel'skiĭ, Usp. Fiz. Nauk **130**, 193 (1980) [Sov. Phys. Usp. **23**, 105 (1980)].
[3] A. A. Karabutov, A. P. Kubyshkin, V. Ya. Panchenko, and P. B. Podymova, Kvant. Elektron. (Moscow) **22**, 820 (1995).
[4] V. P. Skripov, *Metastable Liquids*, Wiley, New York (1974); Russian orig., Nauka, Moscow (1972), 312 pp.
[5] F. Kh. Mirzoev, S. A. Reshetnyak, E. P. Fetisov, and L. A. Shelepin, Preprint No. 017-86 [in Russian], MIFI, Moscow (1986).

Translated by R. M. Durham

Metal–insulator cathode in an rf electron gun

N. I. Aĭzatskiĭ, E. Z. Biller, V. A. Kushnir, V. V. Mitrochenko, I. V. Khodak, and V. F. Zhiglo

''Kharkov Physicotechnical Institute'' National Science Center
(Submitted May 6, 1998)
Pis'ma Zh. Tekh. Fiz. **24**, 36–39 (October 12, 1998)

The possibility of using metal–insulator cathodes in rf guns of 10 cm linear resonant electron accelerators has been studied experimentally for the first time. Results of calculations and the development of a prototype cathode are described. Results of an experimental investigation of the operating regimes of an rf gun are presented. The gun delivered a beam having a particle energy greater than 300 keV, a pulse length of 40–50 ns, and a pulsed current of 3.5–4.5 A.
 [S1063-7850(98)00710-1]

In rf electron guns, the cathode is located in a cavity resonator and electrons are emitted under the action of an rf electric field.[1] These devices have been widely used in linear resonant electron accelerators with high beam brightness. Conventionally used thermionic and photoemissive cathodes can produce beams having durations between 10^{-6} and 10^{-12} s. The production of nanosecond and picosecond electron beams from rf guns with a photoemissive cathode requires elaborate laser systems with laser radiation of suitable duration.[2,3] Thus, it is undoubtedly of interest to study the possibility of using alternative types of cathodes in rf guns to produce high-intensity beams with pulse lengths between 10^{-9} and 10^{-8} s. One possible type of cathode to solve this problem is a metal–insulator cathode.[4–7] The present paper reports an investigation of this type of cathode in fairly high-intensity microwave fields.

The cathode *1* (Fig. 1) is a system of insulating and metal cylinders. Teflon was used as the insulator *4* and the metal part of the cathode *5* was formed by a copper cylinder of 4 mm outer diameter, having a conical tip with a thickness of $\sim 20\,\mu$m at the end. For the experiments we used the resonant rf electron gun system of the LIK linear research accelerator,[3] which consists of two TM_{010} cavities coupled via a central aperture. The working frequency of the gun is 2797.15 MHz. A complete description of the gun is given in Ref. 8.

The initial preparation stage for the experiments involved using the SUPERFISH program[9] to make a series of calculations to determine the influence of the metal–insulator cathode on the quality factor Q, the natural frequency f_0, and the longitudinal electric field distribution in the resonant system of the electron gun. It was shown that for $l = 0.5$–1.5 mm and insulating cylinder diameters of 3 and 4 mm, the incorporation of an insulator with $\tan\delta = 10^{-4}$–10^{-2} and $\varepsilon = 1$–12 has no significant influence on the Q factor ($\Delta Q/Q = 10^{-2}$) and the natural frequency ($\Delta f_0/f_0 = 10^{-5}$) of the gun cavity. The length of the discharge gap was taken as 1 mm which corresponds to a field of $\cong 6.0$ MV/m in the cathode plane with a maximum field of 30 MW/m on the cavity axis.

During the experiments we measured the current from the metal cylinder I_c and the current at the exit from the gun I_g (Fig. 1), which was determined using an inductive current meter *3*. An inductive probe and a microwave detector *2* were used to observe the signal E proportional to the field strength. The amplitude of the field in the cavity was regulated by varying the microwave power P_c supplied to the cavity between 0.1 and 1.5 MW. The electric field strength was determined using the expression

$$E_c(\mathrm{V/m}) = 342\sqrt{P_c(W)Q_0} \quad \text{(Ref. 8)},$$

and the microwave pulse length was 2 μs.

The results of experiments carried out using two cathodes may be summarized as follows. As microwave power builds up in the cavity of the gun, the positive pulsed signal I_c increases. Its amplitude depends exponentially on the field strength, which indicates that in the predischarge stage, field emission from the tapered metal cylinder occurs. When the field in the cavity reaches 25–30 MV/m, the amplitude of the current I_c increases abruptly, approximately by a factor of 20, reaching 18 A. At the exit from the gun the current amplitude and pulse length are 6–8 A and 30–50 ns, respectively.

After some time had elapsed ($\approx 8\times 10^4$ pulses), the cathode operating regime changed to a qualitatively different phase. At the same field strength in the rf gun, the signal I_c only remained positive until the onset of the discharge ,and

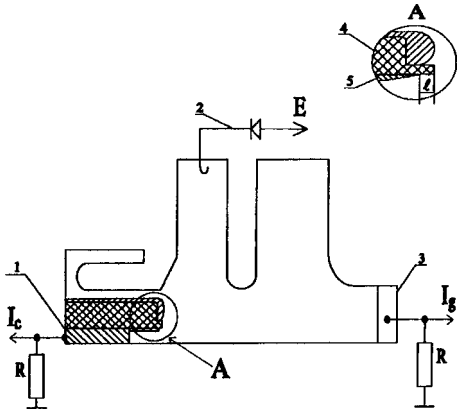

FIG. 1.

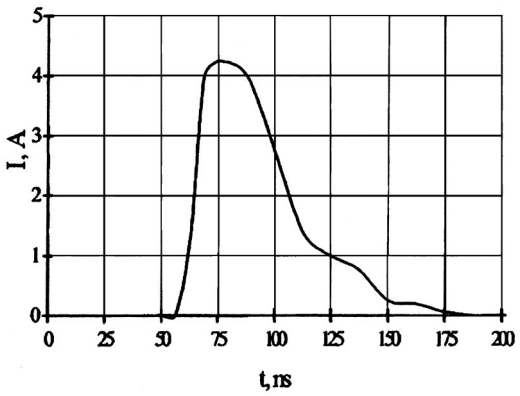

FIG. 2.

the amplitude of this prebreakdown current was less than 1 A. After the discharge had been initiated, this signal became negative until the end of the rf pulse. The pulsed current at the exit from the gun (Fig. 2) had an amplitude of 3.5–4.5 A and a length of 40–60 ns. Under these conditions the field emission current from the tapered metal part of the cathode is clearly not the main source of electrons. The electron energy (more than 300 keV) at the exit of the rf gun was estimated by analyzing the degree of particle capture during the acceleration process in the main part of the accelerator (see Ref. 3). In this regime, the gun operated for more than 5 h at a pulse repetition frequency of 12.5 Hz without any visible changes in the output current characteristics.

In both cases described the fluctuations of the current amplitude and the temporal variability were less than 15% and ± 5 ns, respectively. During the discharge almost all the stored microwave power was utilized and the amplitude of the field dropped to zero and remained at this level until the end of the microwave pulse. This indicates that the cavity is detuned for 2 μs, which is substantially longer than the discharge time of ~ 50 ns. The gun clearly operates in a stored energy mode, since the length of the current pulse is $\tau \ll Q/\pi f_0$. In this case, the length of the output current pulse is determined by the discharge rise rate and by the energy stored in the cavity.

To conclude, we have demonstrated experimentally that a metal–insulator cathode may be used in an rf electron gun to obtain a high-intensity nanosecond beam. At the same time, it should also be noted that the mechanism for emission of electrons from a metal–insulator cathode in fairly high-intensity rf fields has by no means been fully explained. This topic requires comprehensive study and will form the subject of further research.

[1] C. Travier, *RF-Guns: Review*, SERA/90-219/RFG, RFG Note 07, LAL (1990).
[2] C. Travier, in *Proceedings of the Fourth European Particle Accelerator Conference*, Vol. 1 (World Scientific, Singapore, 1994), pp. 317–321.
[3] N. I. Aĭzatskiĭ, E. Z. Biller, V. N. Boriskin *et al.*, Fiz. Plazmy **20**, 671 (1994) [Plasma Phys. Rep. **20**, 603 (1994)].
[4] S. P. Bugaev, A. M. Iskol'dskiĭ, and G. A. Mesyats, Zh. Tekh. Fiz. **37**, 1855 (1967) [Sov. Phys. Tech. Phys. **12**, 1358 (1967)].
[5] G. A. Mesyats and G. N. Furseĭ, *Cold Cathodes* [in Russian], Sovetskoe Radio, Moscow (1974), pp. 287–292.
[6] S. A. Vysotskiĭ, Yu. F. Pavlychev, and V. I. Pershin, in *Proceedings of the 12th All-Union Conference on Charged Particle Accelerators*, Vol. 2 [in Russian] (1990), pp. 11–15.
[7] V. S. Balagura, B. G. Safronov, and S. A. Cherneshchikov, VANT Ser. Yad.-Fiz. Issled. No. 4(25), 48 (1992).
[8] N. I. Aĭzatskiĭ, E. Z. Biller, A. N. Dovbnya *et al.*, Prib. Tekh. Éksp. No. 1, 34 (1997).
[9] J. H. Billen and L. M. Young, in *Proceedings of the 1993 Particle Accelerator Conference*, Vol. 2 (1993), pp. 790–792.

Translated by R. M. Durham

Chain mechanism for initiation of hydrocarbon oxidation reactions in a low-temperature plasma

Yu. N. Novoselov, V. V. Ryzhov, and A. I. Suslov

Institute of Electrophysics, Urals Branch of the Russian Academy of Sciences, Ekaterinburg;
Institute of High-Current Electronics, Siberian Branch of the Russian Academy of Sciences, Tomsk
(Submitted March 23, 1998)
Pis'ma Zh. Tekh. Fiz. **24**, 40–43 (October 12, 1998)

A self-consistent model is used for a numerical study of the kinetics of plasma-chemical reactions initiated in a low-temperature gas-discharge plasma in an atmospheric-pressure CH_4O_2 mixture. An analysis is made of a chain mechanism for the formation of radicals in ion-molecular processes involving water and oxygen molecules, which can appreciably reduce the energy consumption needed to form the oxidation products. It is shown that under the conditions of a non-self-sustained, electron-beam-initiated, atmospheric-pressure discharge the energy consumption needed to produce methanol molecules may, at a few eV, be between four and fives times lower than that in a self-sustained discharge. [S1063-7850(98)00810-6]

The initiation of hydrocarbon oxidation reactions in a low-temperature plasma to process natural gas or purify air from organic molecular contaminants is a promising line of research in plasma physics. The oxidizing conversion of natural gas can produce various valuable oxygen-containing products (methanol, formaldehyde, formic acid, and so on). However, the high energy consumption (tens of eV)[1] needed to form the active radicals is a major disadvantage impeding the widespread implementation of these technologies. The energy consumption can usually be reduced appreciably when the oxidation reactions are initiated with the involvement of chain processes.[2]

A self-consistent numerical model has been developed to analyze the kinetics of the oxidation processes in a hydrocarbon plasma. This model includes calculations of the system used to supply energy to the reactor active zone (electron beam or gas discharge), calculations of the rate constants of reactions involving electrons by means of a numerical integration of the Boltzmann equation for the electron energy distribution function, and solution of the rate equations for gas-phase reactions.[3] In the present study the initial gas was a mixture of methane (92%) and oxygen. The choice of numerous other more complex hydrocarbons as initial components presents no major difficulties, since the oxidation kinetics of methane embraces a very broad spectrum of organic molecules.

The model takes into account processes involving the formation of CH_3, HO_2, H, O, and OH radicals as a result of direct dissociation of CH_4, H_2O, and O_2 and also in reactions of electronically excited states of CO, O, and O_2 with hydrocarbons and other stable molecules in the mixture. Particular attention is focused on ion-molecular processes which may result in the formation of these radicals. In particular, the reaction chain

$$\begin{array}{ccccc} e & \xrightarrow{H_2O} & H^- & \xrightarrow{O_2} & HO_2 + e \\ \uparrow & & & & \downarrow \\ & \longleftarrow & E/N & \longleftarrow & \end{array} \qquad (1)$$

gives OH radicals, HO_2, and an electron which can repeatedly participate in their formation, obtaining the necessary energy from the field. In the presence of this type of chain, the energy consumption needed to form the final reaction products is reduced substantially.

To test the program we compared the results of the numerical simulation and an experiment[4] where the oxidation of methane was investigated in a plasma-chemical reactor with an atmospheric-pressure barrier discharge in a CH_4/O_2 mixture at a temperature of 100°C. The most convenient for such a comparison is the range of low specific input energies (approximately $<0.2\,J/cm^3$), when a small quantity of oxidation products (less than 1%) forms in the reactor. In this case, the methanol yield depends almost linearly on the input energy and the calculated dependence shows good agreement with the experimentally measured values. Most of the experimental data was obtained under these conditions. The calculations showed that in terms of current density, these values fall approximately within the shaded area. In Fig. 1 the triangle indicates the experimental energy consumption needed to form CH_3OH in one of the regimes.

In order to search for the optimum conditions for the chain process (1), the numerical model was used to investigate the yield of oxidation products at current densities in the microchannel $j=0.3-10.0\,A/cm^2$. Figure 1 gives the energy consumption ε needed to form a CH_3OH molecule as a function of j, both taking into account the chain mechanism (1) (curve *2*) and neglecting it (curve *1*). The rise in consumption as j increases is caused by an increase in the energy losses in electron–ion recombination events, while the drop in efficiency with decreasing current density is caused by a

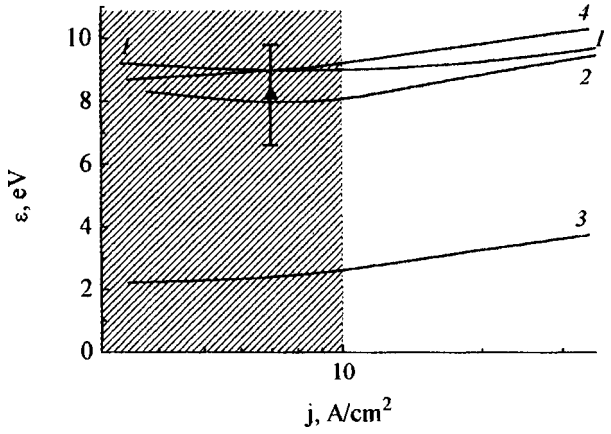

FIG. 1. Yield of CH_3OH as a function of discharge current density: *1*, *2*—barrier discharge, *3*—electron-beam-initiated discharge, and *4*—non-self-sustained discharge neglecting chain process.

reduction of the parameter E/N in the gap (the current density was regulated by varying the amplitude of the applied voltage). The calculations show that the chain process in a barrier-discharge plasma weakly influences the CH_3OH yield. This can be attributed to the high electron energy consumption needed to excite the electronic levels of the molecules in comparison with the channel for dissociative attachment of electrons to H_2O.

A substantial reduction in the energy consumption for the yield of incomplete oxidation products may be achieved in a non-self-sustained discharge with constant E/N considerably below the breakdown value. Figure 1 gives the calculated dependence $\varepsilon(j)$ for a non-self-sustained discharge initiated by a 10 ns electron beam for E/N of order 10 Td (curve *3*). The duration of the entire discharge was 500 ns. For this duration the energy input from the discharge was on the order of 5.0×10^{-3} J/cm^3, whereas the input energy from the beam was 1.0×10^{-4} J/cm^3. The specific input energy of a non-self-sustained discharge neglecting the chain process was 2.0×10^{-4} J/cm^3. In this case, the value of ε is comparable with the energy consumption in a barrier discharge (curve *4*).

One consequence of the chain process is the formation of an additional number of radicals actively participating in ion-molecular reactions (H radicals, for example) which can sustain prolonged burning of a non-self-sustained discharge at low electric field strength. The radicals are generated mainly as a result of low-threshold processes of dissociative attachment of electrons to H_2O and direct dissociation of water and oxygen molecules. Under the conditions obtaining in a barrier discharge, methyl radicals and hydrogen are formed mainly by direct electron-impact decomposition of CH_4 (the threshold for this process is of the order of 10 eV).[5]

To sum up, we have shown by means of a numerical simulation that electron-beam-initiated discharge burning regimes may take place in which oxidation reactions are stimulated by the chain process (1). This can substantially reduce the specific energy consumptions for the oxidizing conversion of hydrocarbons and the oxidation of organic impurities in air.

The lower energy consumption is mainly attributable to a reduction of the parameter E/N in the plasma and the formation of radicals as a result of low-threshold dissociative attachment of electrons to H_2O molecules, and also by direct dissociation of H_2O and O_2.

[1] S. P. Bugaev, V. A. Kuvshinov, N. S. Sochugov *et al.*, in *Proceedings of the International Symposium on High-Pressure, Low-Temperature Plasma Chemistry V*, Hakone, Milovy, Czech Republic, 1996, pp. 145–149.
[2] B. V. Potapkin, V. D. Rusanov, and A. A. Fridman, Dokl. Akad. Nauk SSSR **308**, 897 (1989).
[3] V. V. Ryzhov and A. I. Suslov, in *Proceedings of the 18th Symposium on Plasma Physics and Technology*, Prague, Czech Republic, 1997, p. 56.
[4] K. Okazaki, T. Nozaki, Y. Uemitsu *et al.*, in *Proceedings of the 12th International Symposium on Plasma Chemistry*, Minnesota, 1995, pp. 581–586.
[5] W. L. Morgan, Plasma Chem. Plasma Process. **12**, 477 (1992).

Translated by R. M. Durham

Adhesion mechanism of friction in nanotribocontacts

G. V. Dedkov

Kabardino-Balkar State University, Nalchik
(Submitted April 8, 1998)
Pis'ma Zh. Tekh. Fiz. **24**, 44–50 (October 12, 1998)

An adhesion mechanism is proposed for the frictional force between the tip of an atomic force (friction) microscope and a surface, whereby the frictional force is determined by the energy of breaking and formation of adhesive bonds for a discrete microslide step of length close to the atomic radii of the contacting bodies. Calculations were made of the frictional force as a function of the radius of curvature and the distance between the tip and the surface for silicon–silicon and tungsten–iron contacts. © *1998 American Institute of Physics.*
[S1063-7850(98)00910-0]

At present no satisfactory quantitative theory is available for the forces of adhesive friction at the atomic level (as is indicated in reviews by Tabor[1] and Bhushan *et al.*[2]), although some progress has been achieved in this direction.[3–8] The theory of contact interaction,[9–14] not being strictly atomistic, contains various simplifying assumptions relating to the shape of the contact zone, the type of adhesion forces, and the elastic moduli of the tribosystem which are taken from macroscopic physics, so that an analysis of an elementary adhesive friction event for the simplest tribocontact, such as the tip of an atomic force (friction) microscope and a planar surface, is a very topical problem.

The basic physical idea developed here was in fact put forward by Tabor.[1] Each elementary discrete event in which the tip slides along the surface is accompanied by an abrupt (irreversible) breaking of adhesive bonds between atoms of the contacting bodies and also by an equally sudden formation of new bonds (this last process has been called an ''adhesion avalanche'' Ref. 4). The atoms taking part in these processes are set in vibrational motion, entraining neighboring atoms and imparting to them an excess potential energy which ultimately results in thermal dissipation of the energy.

The mechanism described is shown schematically in Fig. 1. The initial position of the tip (Fig. 1a) is characterized by the minimum energy of the tribosystem and by the presence of steady-state adhesive bonds, some of which are shown by the solid lines connecting contacting atoms. If the force F applied to the tip exceeds a critical value, microslip occurs, causing the tip to shift to the right by the distance Δx. The typical value of Δx should be of the same order of magnitude as the interatomic distance or the lattice period since, for an infinitely slow shift, the atomic configuration of the tip and the section of the surface is close to the initial configuration, and thus the total energy of the system remains unchanged. This is consistent with the experimentally observed discrete behavior of the breaking of adhesive bonds during the operation of an atomic force microscope[15] and also with the geometric model of jerky tip motion (stick–slip motion in English terminology).[16] Essentially the same ideas were also put forward by Deryagin.[17]

As a result of the abrupt sudden motion of the tip, the adhesive bonds do not have time to relax, so they break and new bonds form. In Fig. 1b the broken bonds are shown by the broken lines to the left of the tip and the newly formed bonds are shown by the heavy lines on the right.

Calculation of the energy of the broken and newly formed adhesive bonds is a key issue in quantitative estimates of the frictional force. Here, the following simple formula is proposed:

$$\Delta W = \sum_k |\Delta w_k|, \tag{1}$$

where Δw_k is the change in energy of the kth bond. Summation is over to all bonds which contribute to the total energy of the adhesive contact. Using formula (1) we obtain for the dissipative frictional force

$$F = \Delta W / \Delta x. \tag{2}$$

The frictional force defined by formulas (1)–(2) differs fundamentally from the internal frictional force calculated in Refs. 6–8 in terms of the change in the total energy; in this treatment, the total energy is zero. The irreversibility of the elementary sliding event is reflected by the sign of the absolute value in formula (1). Any change in the energy of any adhesive pair causes this energy to be dissipated via the vibrational motion of the contact atoms. In this context, the concept of an external frictional force introduced by Pokropivnyĭ *et al.*[6–8], artificially defined as the difference between the tangential components of the forces acting on the tip relative to two successive slide steps in the simulation process, becomes meaningless. These types of forces are not dissipative since the average work accomplished by them is also close to zero.

Evidence in support of the proposed mechanism is also provided by the following factor. Let us assume that the zone of strong adhesive contact has the area A and, for simplicity, that the contact is formed by homogeneous materials. The total adhesion energy of the tribosystem can then be written in the form $W = \gamma A$, where γ is the specific surface energy. If the tip undergoes a sudden shift, assuming that the old adhesive bonds are completely broken and there is a similar

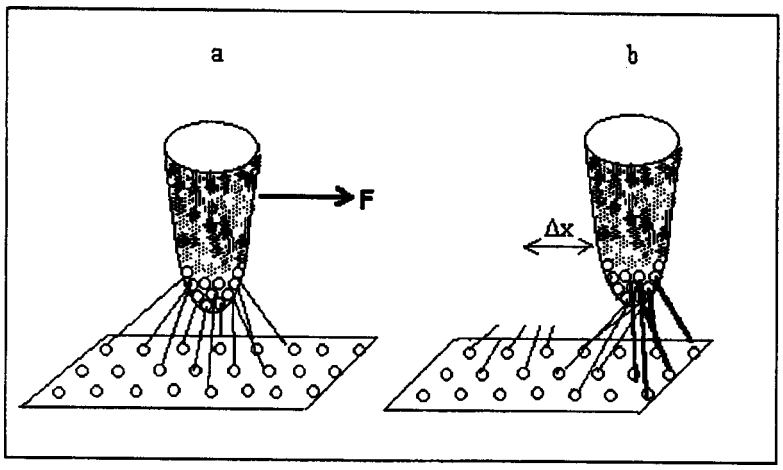

FIG. 1. Illustration of adhesive friction mechanism: a—initial position of tip; b—position after an abrupt shift over the short distance Δx. The broken old adhesive bonds are shown by the broken lines and the newly formed bonds are shown by the heavy lines.

number of newly formed bonds, the energy transformed into random motion of contact atoms will clearly be approximately $\Delta W = 2\gamma A$. Then, using formulas (1) and (2) and assuming $\Delta x = d$, where d is the lattice period, we obtain for the frictional force

$$F = 2\gamma A/d. \tag{3}$$

However, in the pioneering work of Bowden and Tabor,[18] it was shown that for metals the adhesive frictional force is given by

$$F = \tau A, \tag{4}$$

where τ is the shear modulus and A is the real contact area. It follows from Eqs. (3) and (4) that

$$\tau = 2\gamma/d. \tag{5}$$

The existence of this relationship is not coincidental since the orders of magnitude of the numerical values contained in Eq. (5) are internally consistent: $\tau \approx 10^9$ Pa, $\gamma \approx 1$ J/m^2, $d \approx 10^{-9}$ m.

Figure 2 gives the product τr as a function of γ (where r is the atomic radius) plotted for various hard metals with known surface energy and shear modulus. All the numbers are handbook values.[19] The dashed curve was obtained by means of a least-squares fit to the experimental points.

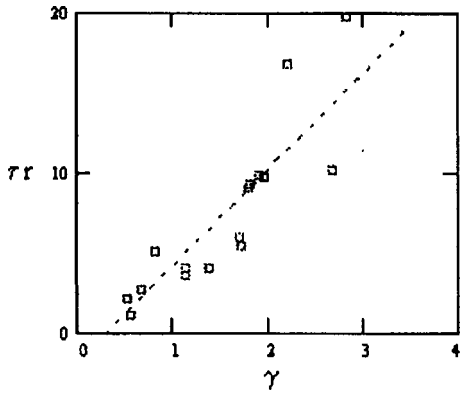

FIG. 2. Correlation between the shear modulus τ, the surface energy γ, and the atomic radius r of hard metals. The units of τr and γ are joules per square meter.

The definite correlation deduced from the figure confirms the validity of the proposed model. The fact that the slope of the curve slightly exceeds the theoretical value of 4 (the value $r = d/2$ was used to plot the graph instead of d) can be explained by the fact that the characteristic breaking (formation) area of the adhesive bonds as the tip moves should exceed twice the area of static contact.

It is interesting to note that by applying formula (5) to calculate the shear modulus for an experiment[14] in which the frictional forces were measured between a silicon tip and an $NbSe_2$ surface, we obtain 6.8×10^8 and 5.8×10^8 N/m^2 for tip radii of 12 and 45 nm if we take the sum of the Nb and Se radii as d and the adhesion energy of this contact as γ. Similar calculations made in Ref. 14 using a fairly involved theory[9] give 6.1×10^8 and 6.6×10^8 N/m^2. The difference compared to the τ values obtained here can be attributed to the different adhesion energy γ for different tip radii according to the data given in Ref. 14: 0.099 J/m^2 and 0.087J/m^2, respectively for radii of 12 and 45 nm (in the static regime).

We also note that formulas (4)–(5) yield the Amonton law for the friction of macroscopic bodies, since the real contact area is proportional to the clamping force.[18]

Under conditions such that a tip slides at distance h from the surface without contact, the frictional force should depend on h and on the radius of curvature R of the tip apex. In order to find these dependences, direct calculations were made using formulas (1) and (2) and the results are plotted in Figs. 3a and 3b for a tribocontact between a silicon tip and an arbitrary square lattice of silicon atoms with period 0.207 nm (Fig. 3a) and also for a contact between a tungsten tip and the (100) plane of the iron crystal lattice. In both cases, the shape of the tip was a paraboloid of revolution, the interaction potentials of the silicon atoms were calculated in the electron gas approximation,[20] and those of the iron and tungsten atoms were calculated in the Morse approximation.[21] To simplify the calculations the atomic structure of the tip and the sample was taken to be rigid, neglecting relaxation, which is justified for fairly large h.

It can be seen from the figures that the frictional force increases approximately linearly as the radius of curvature R of the tip increases and decreases exponentially with increasing h. The linear dependence of the frictional force on the

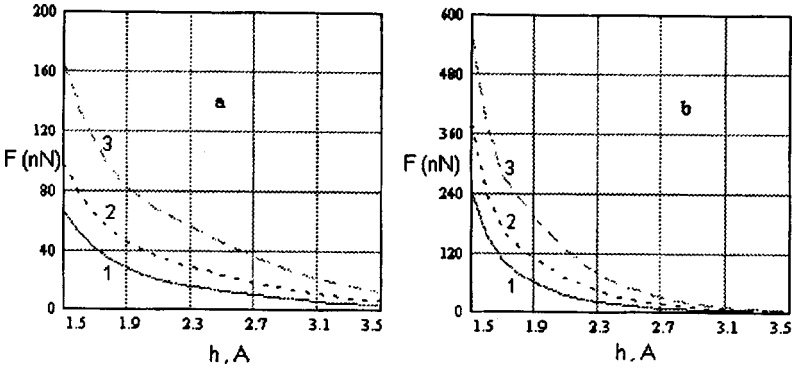

FIG. 3. Friction force versus radius of curvature R and tip height h above surface: *1*—$R=10$ nm, *2*—$R=20$ nm, and *3*—$R=40$ nm; a—silicon tip above an arbitrary square lattice of silicon atoms (period 0.206 nm) and b—tungsten tip above (100) plane of α–Fe crystal. The forces are given in nanonewtons.

radius agrees with the experimental data[14] (see Figs. 11 and 12) for near-zero values of the clamping force, i.e., under conditions of weak contact.

Accurate calculations of the frictional force as a function of the load require allowance for the relaxation of the atomic configuration at the times when the tip becomes ''attached'' to the surface.

This mechanism can be described as stati, since the frictional force does not depend on the tip velocity. Under conditions of sliding at constant velocity other effects also appear which lead (in a first approximation) to a frictional force proportional to the velocity. For instance, momentum may be transferred from the tip to the surface by means of electromagnetic fluctuations (similar to Van der Waals forces) or via the phonon subsystem. These topics require special consideration.

[1] D. Tabor, Trenie Iznos **15**, 296 (1994).
[2] B. Bhushan, J. N. Israelachvili, and U. Landman, Nature (London) **374**, 607 (1995).
[3] W. Zhong and D. Tomanek, Phys. Rev. Lett. **64**, 3054 (1990).
[4] U. Landman, W. D. Luedtke, N. A. Burnham, and R. J. Colton, Science **248**, 454 (1990).
[5] J. B. Sokoloff, Phys. Rev. B **52**, 7205 (1995).
[6] A. V. Pokropivnyĭ, V. V. Pokropivnyĭ, and V. V. Skorokhod, Pis'ma Zh. Tekh. Fiz. **22**(2), 1 (1996) [Tech. Phys. Lett. **22**, 46 (1996)].
[7] V. V. Pokropivnyĭ, V. V. Skorokhod, and A. V. Pokropivnyĭ, Trenie Iznos **17**, 579 (1996).
[8] V. V. Pokropivny, V. V. Skorohod, and A. V. Pokropivny, Mater. Lett. **31**, 49 (1996).
[9] D. Maugis, J. Colloid Interface Sci. **150**, 243 (1992).
[10] R. W. Carpick, N. Agrait, D. F. Ogletree, M. Salmeron, J. Vac. Sci. Technol. B **14**, 1289 (1996).
[11] E. Meyer, R. Luthi, and L. Howald, J. Vac. Sci. Technol. B **14**, 1285 (1996).
[12] K. L. Johnson, Proc. R. Soc. London, Ser. A **453**, 163 (1997).
[13] M. A. Lantz, S. J. O'Shea, A. C. F. Hoole, and M. E. Welland, Appl. Phys. Lett. **70**, 970 (1997).
[14] M. A. Lantz, S. J. O'Shea, M. E. Welland, and K. L. Johnson, Phys. Rev. B **55**, 10776 (1997).
[15] J. H. Hoh, J. P. Cleveland, C. B. Prater, J. P. Revel, and P. K. Hansma, J. Am. Chem. Soc. **114**, 4918 (1992).
[16] J. Kerssemakers and J. Th. M. De Hosson, J. Appl. Phys. **80**, 623 (1996).
[17] B. V. Deryagin, *What is Friction?* [in Russian], Academy of Sciences of the USSR Press, Moscow (1963).
[18] F. P. Bowden and D. F. Tabor, *The Friction and Lubrication of Solids* (Clarendon Press, Oxford, 1950).
[19] I. S. Grigor'ev and E. Z. Mikhaĭlov (Eds.), *Handbook of Physical Quantities* [in Russian], Nauka, Moscow (1991).
[20] G. V. Dedkov, Usp. Fiz. Nauk **165**, 919 (1995).
[21] I. M. Torrens, *Interatomic Potentials* (Wiley, New York, 1972).

Translated by R. M. Durham

Anisotropy of thin ferromagnetic films

A. V. Kovalev

B. P. Konstantinov Petersburg Institute of Nuclear Physics, Russian Academy of Sciences, Gatchina
(Submitted January 22, 1998)
Pis'ma Zh. Tekh. Fiz. **24**, 51–56 (October 12, 1998)

A model is proposed and checked experimentally to describe a direct relationship between the anisotropy of thin ferromagnetic films and the texture of a low-symmetry magnetically ordered phase of CoFe alloy which has a monoclinic unit cell. The measured distortions of the initial cubic cell are an order of magnitude greater than the magnetostriction constants of the solid sample. An analysis is made of a system for the formation of anisotropic stresses in the plane of the film in which this effect is attributed to the magnetic texture. A suitable method is developed for making diffraction measurements and analyzing the experimental data.
 [S1063-7850(98)01010-6]

Intensive research to identify the nature of the uniaxial magnetic anisotropy of thin films has been carried out for some forty years. The models of this phenomenon used so far are described by Prutton[1] and Soohoo.[2] Clemens *et al.*[3] in particular attribute the anisotropy of the magnetic properties of CoFe alloy films to a magnetostrictive effect: when a beam of deposited atoms is obliquely incident, anisotropic stresses are created in the plane of the film which determine the direction of the easy magnetization axis. This clearly poses the question as to the mechanism responsible for the formation of these anisotropic stresses, which usually results in the construction of complex systems for the ordering of the film structure and its defects. Here we propose a self-consistent model for the formation of anisotropy of the mechanical and magnetic properties of thin films in which this anisotropy is a consequence of directional crystallization resulting in the formation of a crystalline texture of a low-symmetry, magnetically ordered phase.

The proposed hypothesis was checked experimentally for films of CoFe30.5V1.5 alloy obtained by magnetron sputtering. X-ray diffraction measurements were made using an automated DRON-3M difffractometer with Cu $K\alpha$ radiation. The films were deposited on 0.1 mm thick glass substrates. The pseudocubic-phase textures were initially determined for samples obtained under different sputtering conditions. Measurements of the crystalline parameters of the low-symmetry phase were made using samples with a symmetric pseudocubic-phase texture:[4] the maximum of the density distribution of the (111) planes lies in the plane of the film, the distribution half-width is $\approx 23°$, and the distribution density of the orthogonal (110) planes does not depend on the azimuthal angle φ. Results will be presented for a sample 7000(70) Å thick. The fixed substrate was positioned 75 mm from the center of the sputtered target whose vertical and horizontal dimensions were in the ratio $\sim 9:1$. The easy magnetization axis coincides with the horizontal direction and strong in-plane magnetic anisotropy is observed (the results of the magnetic measurements will be published in another study). In this case, the average dimensions of the regions of coherent scattering obtained from the broadening of the diffraction peaks are 90(10) Å. No in-plane anisotropy of the crystallite shape is observed.

A schematic of the diffraction measurements is shown in Fig. 1. Let us assume that the x and y axes in the plane of the film (Fig. 1a) coincide with the horizontal and vertical directions of the substrate in the sputtering chamber, n is the normal to the xy plane, $n_{\psi\varphi}$ is the normal to the (110) plane, and ε_1, ε_2, and $\varepsilon_{\psi\varphi}$ are the elastic strains in the appropriate directions. In the experiments measurements were made of the interplanar spacings for two systems of planes: $\psi = 90°$ and $\psi = 35°$. The angle ψ was varied by rotating the sample about the principal axis of the diffractometer while the azimuthal angle φ was varied by rotating the film mounted on a GP-14 texture attachment about the n direction. The interplanar spacings $d(110)$ in the $(\mathbf{a}_1, \mathbf{a}_2, \mathbf{a}_3)$ basis of the pseudoplanar cell (Fig. 1b) are determined by the direction of spontaneous magnetization $\mathbf{I}_s$ in an isolated crystallite.

For the texture described above, it is natural to assume that the in-plane direction of $\mathbf{I}_s$ is along $[\bar{1}10]$. Then, in accordance with the Neimann principle,[5] the symmetry of the ferromagnetic crystal should be described by the 2/m point group, and the [110] directions (Fig. 1b) become nonequivalent. In a standard system[6] the **a**, **b**, and **c** axes of a monoclinic cell coincide with the [110], $[\bar{1}10]$, and [001] directions and the angle between [110] and [001] is not 90°. This type of cell has four different interplanar spacings $d(110)$: $d(\bar{1}10) = d_1$, $d(110) = d_2$, $d(\bar{1}01) = d(0\bar{1}1) = d_3$, and $d(101) = d(011) = d_4$. Then, for the pseudocubic-phase texture described and the existing symmetry of the sputtering conditions, the probabilities of the (111) and $(\bar{1}\bar{1}1)$ planes of isolated crystallites lying in the plane of the film should be the same. This has the result that in the appropriate directions measurements are not made of d_3 and d_4 but of their average, which we shall henceforth denote by d.

The asymmetry of the sputtering conditions may create a preferential orientation of the $[\bar{1}10]$ directions in the xy plane, which is equivalent to the formation of a magnetic texture. For an ideal texture (Fig. 1c) we can measure d_1 ($\psi = 90°$, $\varphi = 0°$), d_2 ($\psi = 35°$, $\varphi = 90°$), and d ($\psi = 90°$,

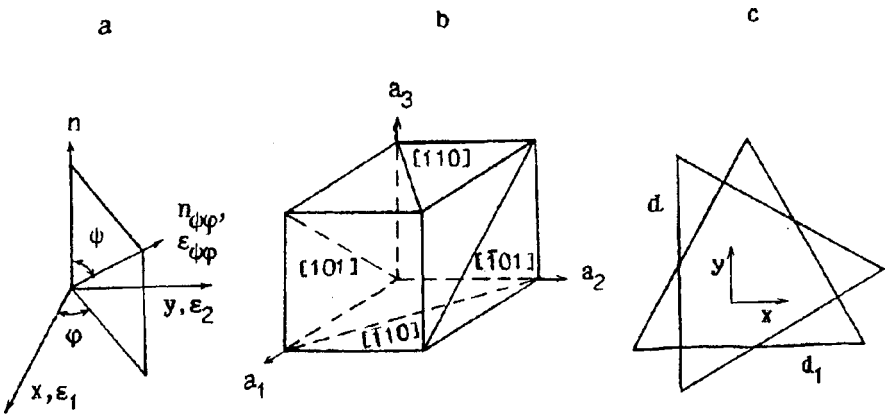

FIG. 1. Schematic of diffraction measurements: a — choice of coordinate system for measurement of adjusting angles, b — nonequivalent directions in monoclinic cell, c — orientation of crystallites for ideal texture (the triangles shown must be supplemented by another two obtained by turning the figure through 180° about the normal to the *xy* plane).

$\varphi=90°$ and $\psi=35°$, $\varphi=0°$), which are related by

$$d_1=d+\delta_1+\delta_2, \quad d_2=d+\delta_1-\delta_2, \tag{1}$$

where δ_1 and δ_2 are the parameters of this model. The contribution of the elastic deformations was taken into account by the standard ''$\sin^2\psi$'' method,[7] which uses the expression

$$\varepsilon_{\varphi\psi}=\varepsilon_1 \sin^2\psi\cos^2\varphi+\varepsilon_2 \sin^2\psi\sin^2\varphi. \tag{2}$$

For the observed pseudocubic-phase texture the triangles formed by the [110] directions uniformly fill the *xy* plane. Then, the probability $P(\varphi)$ that the $(\bar{1}10)$ plane, for instance, falls within a reflecting position depends on φ. For the strongest possible magnetic anisotropy we have

$$P(0°)=1, \quad P(90°)=0. \tag{3}$$

In our case the dependences $d(\varphi,\psi=\text{const})$ are described by linear functions, which were used to analyze the experimental data.

The results of the measurements are plotted in Fig. 2. The absolute values of all the measured $d(110)$ values were determined with the same error $\Delta d\simeq 0.002$ Å, which is insignificant for the calculations of the required parameters. Measurements of the shifts of the diffraction peaks relative to their positions at $\varphi=0°$ were made for angles 2ϑ between 43° and 47°. The relative errors were $\Delta d(110)\leqslant 2\times10^{-4}$ Å.

Assuming the measuring system shown in Fig. 1, we obtain from formulas (1) and (2) the following expressions for the measured values $d(\varphi,\phi)$:

$$g_1=d+\delta_1+\delta_2+\varepsilon_1 d_0+\Delta_1=2.02201\,(14)\text{ Å} \quad (\psi=90°,\ \varphi=0°),$$

$$g_2=d+\varepsilon_2 d_0+\Delta_1=2.01869(14)\text{ Å} \quad (\psi=90°,\ \varphi=90°),$$

$$g_3=d+0.33\varepsilon_1 d_0+\Delta_2=2.01734(14)\text{ Å} \quad (\psi=35°,\ \varphi=0°),$$

$$g_4=d+\delta_1-\delta_2+0.33\varepsilon_2 d_0+\Delta_2=2.01896(14)\text{ Å} \quad (\psi=35°,\ \varphi=90°), \tag{4}$$

where Δ_1 and Δ_2 are the systematic errors of the absolute measurements caused by the indeterminacy of the instrumental ''zero'' and other geometric factors, and d_0 is the average of $d(\varphi,\psi)$. The condition $\Delta_1=\Delta_2$ was satisfied so that the system (4) could be solved, and additional optical measurements were also made. The film, attached to a mandrel with a cylindrical hole, has an almost spherical shape whose radii of curvature measured in the *x* and *y* directions were $R_x=417\ (14)$ mm and $R_y=455\,(14)$ mm. In this case, the system (4) yields the following values of the model parameters:

$$\delta_1=2.52(30)\times10^{-3}\text{ Å}, \quad \delta_2=0.95(36)\times10^{-3}\text{ Å},$$

$$\varepsilon_1 d_0=1.79(29)\times10^{-3}\text{ Å}, \quad \varepsilon_2 d_0=1.94(29)\times10^{-3}\text{ Å},$$

which are determined assuming that condition (3) is satisfied. The true values of the spontaneous deformation caused by the magnetic ordering can only be higher than those obtained.

The existence of magnetic texture should give rise to anisotropy of the elastic stresses in the plane of the film. For samples with strongly defined magnetic anisotropy in the free state the film–substrate system shows preferential bending about the *y* direction, i.e., the elastic stresses are clearly anisotropic in the *xy* plane (Fig. 1). We now hypothesize that during sputtering some quasiequilibrium stress state is formed in the film at a temperature around 200 °C. During

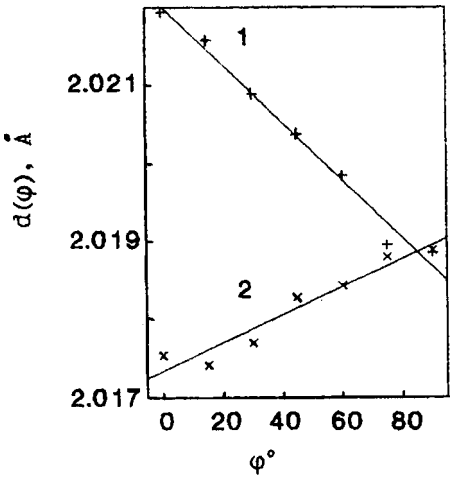

FIG. 2. Measured interplanar spacings for fixed angles ψ: *1* — $\psi=90°$, *2* —$\psi=35°$. The scale of the absolute values of $d(\varphi)$ was determined to within ~0.002 Å.

cooling additional stresses appear in the film as a result of the difference between the coefficients of thermal expansion of the film and the substrate. The existence of a magnetically ordered phase texture implies that the in-plane directions are nonequivalent. In this case, the elastic deformations of the film are determined by the tensor components of the coefficients of thermal expansion. For monoclinic symmetry this symmetric second-rank tensor has four independent components.[8] Thus, in the proposed model the anisotropy of the elastic deformations is a consequence of the magnetic texture and not the cause of it.

This work was supported by the Russian Fund for Fundamental Research (Project No. L-EH 96-15-96775).

The author takes great pleasure in thanking V. V. Deriglazov, A. V. Zaĭtsev, A. I. Okorokov, B. G. Peskov, V. A. Ul'anov, G. E. Shmelev, and A. F. Shchebetov for assistance with the work.

[1] M. Prutton, *Thin Ferromagnetic Films* (Butterworths, Washington, 1964; Sudostroenie, Leningrad, 1967, 266 pp.).
[2] R. F. Soohoo, *Magnetic Thin Films* (Harper and Row, London, 1965; Mir, Moscow, 1967, 422 pp.).
[3] D. Clemens, A. Vananti, C. Terrier *et al.*, Physica B **234–236**, 500 (1997).
[4] A. V. Kovalev, Preprint No. PIYaF–2199 [in Russian], Institute of Nuclear Physics, Gatchina, (1997), 11 pp.
[5] L. A. Shuvalov, in *Modern Crystallography: Vol. 4, Physical Properties of Crystals*, [in Russian], Nauka, Moscow (1981), 495 pp.
[6] B. K. Vaĭnshteĭn, *Modern Crystallography: Vol. 1, Crystal Symmetry. Methods of Structural Crystallography* [in Russian], Nauka, Moscow (1979), 383 pp.
[7] Ya. S. Umanskiĭ, Yu. A. Skakov, A. N. Ivanov, and L. N. Rastorguev, *Crystallography. X-Ray and Electron Microscopy* [in Russian], Metallurgiya, Moscow (1982), 631 pp.
[8] Yu. I. Sirotin and M. P. Shaskol'skaya, *Principles of Crystal Physics* [in Russian], Nauka, Moscow (1975), 680 pp.

Translated by R. M. Durham

A new class of electrostatic systems which keep plane homogeneous charged-particle beams exactly parallel

L. G. Glikman and Yu. V. Goloskokov

Institute of Nuclear Physics, National Nuclear Center, Alma-Ata, Kazakhstan
(Submitted August 11, 1997; resubmitted March 23, 1998)
Pis'ma Zh. Tekh. Fiz. **24**, 57–61 (October 12, 1998)

An analysis is made of electrostatic systems whose field is formed by two superposed two-dimensional fields with a common plane of symmetry (midplane). It is assumed that these fields overlap in the region where a charged particle beam propagates. The main property of these systems is that they conserve ideally (without angular aberrations) the parallelism of a charged particle beam of uniform energy-to-charge ratio, propagating in the midplane of the field. This new class of electrostatic system includes the four-electrode system given as an example in which each electrode consists of four plates positioned symmetrically relative to the midplane. © *1998 American Institute of Physics.* [S1063-7850(98)01110-0]

Plane parallel charged particle beams having uniform energy-to-charge and mass-to-charge ratios, propagating in two-dimensional or conical static electromagnetic fields ideally (without angular aberrations) conserve their parallelism after propagation through these fields (see, for example, Refs. 1 and 2). In these cases, the particles propagate in the midplane which forms the plane of symmetry of the electric field and the plane of antisymmetry of the magnetic field. Here we propose another class of electrostatic systems whose field is formed by two superposed two-dimensional fields with a common plane of symmetry (midplane). The parallelism of plane charged particle beams having uniform energy-to-charge ratios is ideally preserved after propagating through the field of these systems. In what follows, for conciseness we shall describe charged particle beams having uniform energy-to-charge ratios as homogeneous.

We shall assume that in an x,y,z Cartesian coordinate system, the common midplane of two two-dimensional fields coincides with the $z=0$ plane, and that one of the two-dimensional fields is described by the potential $\varphi_1(x,z)$, and the other by the potential $\varphi_2(y,z)$. In the nonrelativistic approximation, the Hamilton–Jacobi equation describing the motion of a charged particle in the midplane of these superposed fields described by the scalar potential $\varphi=\varphi_1+\varphi_2$ has the form

$$\frac{1}{2m}\left[\left(\frac{\partial S_0}{\partial x}\right)^2+\left(\frac{\partial S_0}{\partial y}\right)^2\right]+e\Phi_1(x)+e\Phi_2(y)=E, \tag{1}$$

where e is the particle charge, m is its mass, S_0 is the reduced action function, related to the action function S by $S=-Et+S_0$, t is the time, E is a constant equal to the total particle energy, $\varphi_1(x,0)\equiv\Phi_1(x)$, and $\varphi_2(y,0)\equiv\Phi_2(y)$. In Eq. (1) the variables are separated. Substituting S_0 into this equation in the form of the sum $S_0(x,y)=S_1(x)+S_2(y)$, we obtain

$$\frac{1}{2m}\left(\frac{dS_1}{dx}\right)^2+e\Phi_1(x)-E=-\frac{1}{2m}\left(\frac{dS_2}{dy}\right)^2-e\Phi_2(y)=\lambda, \tag{2}$$

where λ is an arbitrary constant. Equation (2) is used to find the momenta $P_x=m$, $\dot{x}=dS_1/dx$ and $P_y=m$, $\dot{y}=dS_2/dy$, after which the complete integral of the Hamilton–Jacobi equation is determined. Then a well known method is used to find the particle trajectory equation in quadratures,

$$\int_{x_0}^{x}\frac{(\operatorname{sgn}\dot{x}(x))dx}{\sqrt{W_0\sin^2\theta_0+e(\Phi_{10}-\Phi_1)}} - \int_{y_0}^{y}\frac{(\operatorname{sgn}\dot{y}(y))dy}{\sqrt{W_0\cos^2\theta_0+e(\Phi_{20}-\Phi_2)}}=0, \tag{3}$$

and the relationship between the coordinate x and the time t

$$t-t_0=\sqrt{\frac{m}{2}}\int_{x_0}^{x}\frac{(\operatorname{sgn}\dot{x}(x))dx}{\sqrt{W_0\sin^2\theta_0+e(\Phi_{10}-\Phi_1)}}. \tag{4}$$

Here W is the particle kinetic energy, θ is the angle between the particle velocity and the y axis, and the zero subscript indicates the initial values of the variables. The subscript "$i\,0$", $i=1,2$ indicates that the potential labeled i is calculated at the initial point of the trajectory. Using Eqs. (1)–(3), we can find the angle θ at any point on the trajectory of a particle moving in the midplane:

$$\sin^2\theta=\frac{W_0\sin^2\theta_0+e(\Phi_{10}-\Phi_1)}{W_0+e(\varphi_0-\Phi_1-\Phi_2)}. \tag{5}$$

This last equation yields one of the main properties of electron-optical systems with this type of field, i.e., after entering this field, a homogeneous parallel charged-particle beam propagating in the midplane exactly (without angular aberrations) preserves its parallelism after propagating through the field. The required electron-optical properties of this field perpendicular to the midplane and in the two-dimensional field are provided by selecting the potentials at the electrodes of the system used to generate this field. In particular, conditions can be selected to conserve the parallelism of a three-dimensional homogeneous beam (telescopic conditions). The parameters of the proposed system which

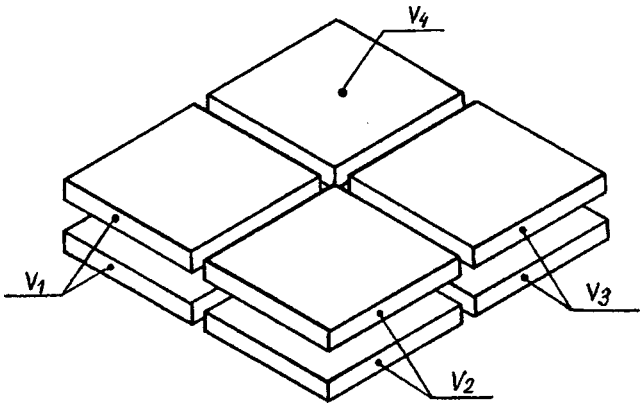

FIG. 1. Four-electrode electrostatic system.

characterize its properties perpendicular to the midplane, are calculated using general formulas for electron-optical systems with a midplane.[3,4]

By way of an example of the proposed systems, we describe a four-electrode system whose field-defining surfaces lie on two planes parallel to the midplane and separated from it by the same distance $d/2$ (see Fig. 1). Each electrode consists of two plates at the same potential and positioned symmetrically relative to the midplane. It is assumed that the gaps between the plates of neighboring electrodes are so small than their width can be neglected when studying the electron-optical properties. In cases of practical interest, it is generally sufficient for the width of the gaps between the plates to be $\approx 0.1d$. The plates of the first electrode projected onto the midplane occupy the quadrant $x<0$, $y<0$, those of the second electrode occupy the quadrant $x>0$, $y<0$, those of the third the quadrant $x>0$, $y>0$, and those of the fourth the quadrant $x<0$, $y>0$. The electrode potentials are denoted by V_1, V_2, V_3, and V_4, respectively. It is easy to establish that under these assumptions the potential φ may be represented as the sum of the potentials $\varphi_1(x,z)$ and $\varphi_2(y,z)$ of two two-electrode systems with a two-dimensional field if the following condition is satisfied:

$$V_3 - V_2 = V_4 - V_1. \tag{6}$$

The field of each system with a two-dimensional field decays rapidly with increasing distance from the gaps separating the electrodes. Thus, if we impose the constraint that the field of this four-electrode system at the boundary of the region occupied by the field should not exceed 0.01% of the maximum, in the midplane the field of the system may be considered to be concentrated in the cross-shaped region

$$\left|\frac{x}{d}\right| \leqslant 3, \quad \left|\frac{y}{d}\right| \leqslant 3. \tag{7}$$

Outside this region the particle trajectories can be considered to be rectilinear for most practical applications. In addition, refraction of the rays on entering and leaving the field can be neglected. As for the case of two-dimensional fields generated by electrodes separated by straight gaps (see Refs. 1 and 5), for this particular system we can easily select shapes and sizes of plates for which the field in the region where the beam propagates agrees with the calculated value. The problem of coupling the beam into and out of the system can easily be solved if the potential of the first electrode in the beam path matches the potential of the object space and the potential of the last electrode in the beam path matches that of the image space. The design solution depends on the particular application of the proposed electron-optical system. For example, when it is used as a prism in a dihedral electrostatic prism energy analyzer, the potentials of the object and image spaces match the electrode potentials of the collimator and focusing lenses adjacent to the prism. Similar design solutions can be found in Refs. 1 and 5. However, unlike a prism with separate two-dimensional fields, the new prism will be substantially more compact.

The proposed system can also be effectively used as a mirror with a large angle of deflection and a lens with a straight optic axis which can ideally broad plane charged-particle beam with a large energy spread exactly parallel. Other practical applications are also possible.

The authors thank S. Ya. Yavor for interest in this work and useful comments.

[1] V. M. Kel'man and S. Ya. Yavor, *Electron Optics* [in Russian], Nauka, Leningrad (1968), 488 pp.
[2] L. G. Glikman, Zh. Tekh. Fiz. **54**, 1986 (1984) [Sov. Phys. Tech. Phys. **29**, 1166 (1984)].
[3] S. P. Karetskaya and L. V. Fedulina, Zh. Tekh. Fiz. **52**, 740 (1982) [Sov. Phys. Tech. Phys. **27**, 419 (1982)].
[4] S. P. Karetskaya, L. G. Glickman, L. G. Beizina, and Yu. V. Goloskokov, Adv. Electron. Electron Phys. **89**, 391 (1994).
[5] V. M. Kel'man, S. P. Karetskaya, L. V. Fedulina, and E. M. Yakushev, *Electron-Optical Elements of Charged-Particle Prism Spectrometers* [in Russian], Nauka, Alma-Ata (1979), 232 pp.

Translated by R. M. Durham

Formation of macroparticle structures in an rf induction discharge plasma

Yu. V. Gerasimov, A. P. Nefedov, V. A. Sinel'shchikov, and V. E. Fortov

Scientific-Research Center of Pulsed Heat Physics, Russian Academy of Sciences, Moscow
(Submitted May 26, 1998)
Pis'ma Zh. Tekh. Fiz. **24**, 62–68 (October 12, 1998)

It was demonstrated experimentally that macroparticles may undergo levitation and form ordered structures in an rf induction discharge plasma. The experiments were carried out using 1.87 μm melamine formaldehyde particles in neon at a pressure of 25–500 Pa. The generator frequency was 100 MHz. © *1998 American Institute of Physics.* [S1063-7850(98)01210-5]

In recent years, many experimental and theoretical studies have been devoted to dust plasmas, i.e., plasmas containing macroparticles.[1,2] Interest in this type of research was stimulated by the theoretical prediction of Ikezi[3] and subsequent experimental confirmation that various types of ordered structures may be formed from macroparticles injected into the plasma, including plasma crystals. The formation of ordered structures was observed in an rf capacitive discharge plasma,[4] a stratified glow discharge,[5] and in a thermal plasma of hydrocarbon fuel combustion products.[6] In the combustion product plasma the macroparticles acquired a positive charge of $Z_p \sim 10^3$ electron charges as a result of thermal emission. At a gas temperature $T_g = 1700$ K, particle density $n_p = 5 \times 10^7\ \mathrm{cm}^{-3}$, and electron density $n_e \sim 10^{10}\ \mathrm{cm}^{-3}$ the measured pair correlation function clearly revealed a peak indicative of short-range interaction order and characteristic of a liquid.

In a discharge plasma the macroparticles acquire a negative charge, which is determined by the floating potential at a given point in space and by the macroparticle size. In various experiments the value of Z_p varied between 10^4 and 10^6 electron charges. On entering an electrostatic trap, depending on the conditions which are characterized to a first approximation by the ideality parameter, macroparticles group into an ensemble having some particular order. In simulations of structures formed from macroparticles, allowance must be made for the force of the gravitational field, interaction of particles among themselves and with an external electric field, and also interaction of particles with the plasma neutral and ion components.[7] The suspension (levitation) of macroparticles and the formation of ensembles possessing different degrees of order takes place in a discharge zone where the constant component of the electric field exhibits appreciable nonuniformity acting as an electrostatic trap for the charged macroparticles. In an rf capacitive discharge this trap forms near the electrodes, whereas in a stratified glow discharge it forms at the head of the striation.

Here we report the first observations of ordered structures in an rf induction discharge plasma. Unlike the types of discharge mentioned above, an rf induction discharge is an electrodeless discharge. This factor is highly attractive from the viewpoint of various technological applications and for fundamental research, since it is possible to produce and study plasmas having different configurations and lengths. In an rf induction discharge it is predicted that isolated charged macroparticles and ensembles of these particles will levitate in the region between the homogeneous quasineutral plasma and the wall confining the plasma volume, or the neutral gas surrounding it.

The plasma was generated in a vertical glass tube, 20 mm in diameter and 20 cm long, using a standard PPBL-3 device used to supply electrodeless lamps which serve as sources of atomic line spectra of various metals. The generator frequency was 100 MHz. Estimates indicate that the average power deposited in the inductor was around 1 W and could be varied severalfold by varying the current through the inductor in the range $I = 60$–200 mA. The tube was inserted in an inductor formed by four coils so that its lower end was several millimeters below the first inductor coil (see Fig. 1). The working gas was neon at pressure P between 25 and 500 Pa. When the generator was switched on, the lumi-

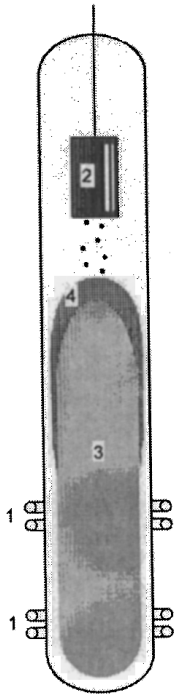

FIG. 1. Schematic of experimental tube: *1*—inductor coils, *2*—particle container, *3*—luminous plasma volume, and *4*—region containing levitating particles.

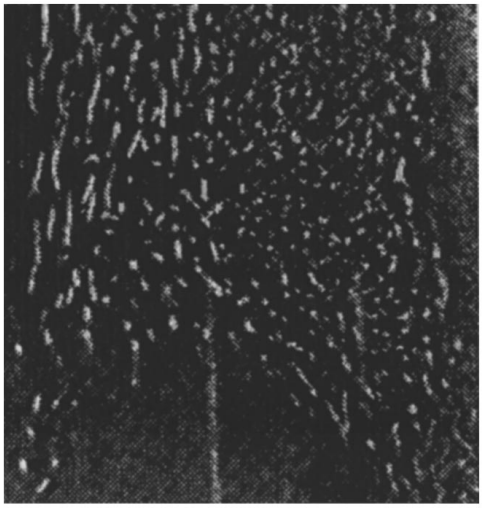

FIG. 2. Image of vertical cross section (8.4×8.7 mm) of particle ensemble for $I=120$ mA and $P=63$ Pa.

FIG. 4. Image of four particles levitating near the walls at $I=150$ mA and $P=115$ Pa. Size of fragment 3.6×5.0 mm.

nous plasma region filled the entire tube in the transverse direction. In the vertical direction, the size of the plasma depended on the gas pressure and the generator power, and could vary between a few centimeters and the entire vertical dimension of the tube. Particles were injected into the plasma by shaking a metal container located in the upper part of the tube 70 mm from the upper coil of the inductor. The bottom of the container was made of a fine metal mesh. Melamine formaldehyde particles of diameter $1.87 \pm 0.04\ \mu$m were used. Taking the density of the material as $1.5\ \mathrm{g/cm^3}$, the weight of a single particle was $4.1 \times 10^{-5}\ \mu$g.

The particle observation system was similar to that used in Ref. 5. A knife-shaped 670 nm diode laser beam having a width of 25 mm and a thickness of around 200 μm near the constriction illuminated the volume under study. The laser beam could be moved vertically and horizontally and its plane rotated. In this way, different cross sections of the plasma could be observed. The particles were observed in scattered laser radiation using a CCD camera mounted at an angle of 60° to the plane of the laser knife and the images obtained were recorded with a video recorder.

Particle levitation was observed near the wall and at the upper boundary of the plasma, i.e., in the transition region between the uniformly luminous plasma and the neutral gas (see Fig. 1). Figure 2 shows an image of the vertical cross section of an ensemble of particles suspended above the luminous region, which was recorded at pressure 63 Pa and current 120 mA. It can be seen that the individual particles oscillate about the equilibrium position and their image is blurred. As the pressure increases, the amplitude and frequency of the oscillations decreases. In all cases, however, regardless of how the particles behaved (whether they oscillated or remained in a fixed state), the region in which they levitated was sharply delimited: the upper limit was some boundary in the neutral gas and the lower limit was the boundary of the luminous plasma, which can be identified with the region of homogeneous quasineutral plasma. This behavior shows up clearly in Fig. 2. An increase in the generator power caused the volume occupied by the plasma to expand, i.e., shifted the boundary of the luminous zone in the vertical direction and thus shifted the entire particle region.

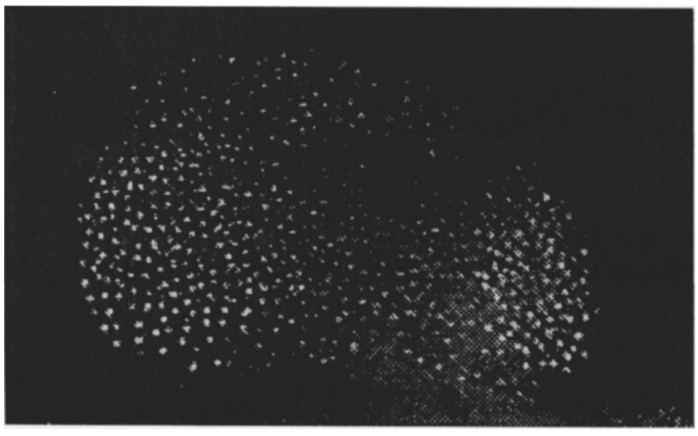

FIG. 3. Image of vertical cross section (6.4×3.9 mm) of particle ensemble for $I=200$ mA and $P=500$ Pa.

The pattern of particle motion showed little change.

At a pressure of the order of 500 Pa and generator current of 200 mA, a stable structure consisting of numerous particles was observed between the plasma and the bottom of the metal container (the typical distance between them was of the order of 2 cm). Figure 3 shows a cross section of this region in the vertical plane. Increaing the total number of particles (by injecting additional particles) increased the size and changed the shape of the structure in the vertical direction, and also resulted in the appearance of directional circulating particle fluxes in the lower part of the structure.

Near the wall we observed separately suspended particles and vertical chains of several particles which could levitate for an arbitrarily long time. Figure 4 shows an image of four particles suspended near the wall at pressure 115 Pa and generator current 150 mA. The distance between the particles was around 700 μm. Changing the generator power did not cause any substantial change in the observed pattern until the upper boundary of the plasma approached the region of observation.

To sum up, it has been demonstrated experimentally for the first time that ordered macroparticle structures may be obtained in an rf induction discharge plasma. The shape and behavior of the particle ensembles is very similar to those observed in a stratified dc glow discharge.

In conclusion, the authors thank V. I. Molotkov and V. M. Torchinskiĭ for assistance with the experiments and also A. M. Lipaev for helping to processes the video images.

[1] V. N. Tsytovich, Usp. Fiz. Nauk **167**, 57 (1997).
[2] A. P. Nefedov, O. F. Petrov, and V. E. Fortov, Usp. Fiz. Nauk **167**, 1216 (1997).
[3] H. Ikezi, Phys. Fluids **29**, 1764 (1986).
[4] H. Thomas, G. E. Morfill, V. Demmel *et al.*, Phys. Rev. Lett. **73**, 652 (1994).
[5] A. M. Lipaev, V. I. Molotkov, A. P. Nefedov *et al.*, Zh. Éksp. Teor. Fiz. **112**, 2030 (1997) [JETP **85**, 1110 (1997)].
[6] V. E. Fortov, A. P. Nefedov, O. F. Petrov *et al.*, JETP Lett. **63**, 187 (1996).
[7] T. Nitter, Plasma Sources Sci. Technol. **5**, 93 (1996).

Translated by R. M. Durham

Modeling of a crossed-groove cavity in the 8 mm wavelength range

F. F. Baryshnikov, G. A. Bogatova, G. D. Bogomolov, V. V. Zavyalov, V. A. Ipatov, A. I. Kleev, V. V. Perebeĭnos, N. V. Cheburkin, and E. Yu. Shamparov

State-Owned Special Design Bureau ''Granat,'' Moscow;
P. L. Kapitsa Institute of Physics Problems, Russian Academy of Sciences, Moscow
(Submitted March 31, 1998)
Pis'ma Zh. Tekh. Fiz. **24**, 69–75 (October 12, 1998)

Results are presented of experiments on the scale modeling of a crossed-groove quasioptic cavity. It is demonstrated that high-Q modes can be excited with a ring structure at the mirror and a field maximum at the center of the cavity. © *1998 American Institute of Physics.*
[S1063-7850(98)01310-X]

Crossed-groove quasioptic cavities have been proposed for infrared free-electron lasers with high average powers (10–100 kW or higher).[1] A characteristic feature of this cavity is that its dominant oscillation is azimuthally symmetric, bounded by caustics, and focused near the central part of the cavity; but unlike cavities with spherical mirrors, it has an annular field distribution at the mirrors. Thus, the apertures at the center of the mirrors should weakly perturb this oscillation, and an axial electron beam can be passed through these mirrors to interact with the field in the cavity. Replacing the spherical-mirror cavity in a high-power free-electron laser[2] with a crossed-groove cavity can especially simplify the electron output of the radiation[3,4] and can also reduce the specific thermal load on the mirrors by increasing the area occupied by the field on the mirror.

The qualitative pattern of field formation in crossed-groove cavities was described in Refs. 5 and 6 and the characteristics of the natural oscillations were analyzed theoretically and numerically in Refs. 7–9. In this brief communication we describe preliminary results of experimental modeling of the oscillations in crossed-groove cavities.

Experimental investigations of optical cavities using a full-scale prototype are difficult because the fabrication of such a prototype is frequently no easier than fabricating a working cavity. In addition, it is comparatively difficult to develop the instrumentation needed for this research in the infrared (such as tunable radiation sources, detectors, and so on).

A possible method of solving this problem is scale modeling based on known scaling laws.[10] If the characteristic dimensions of the system are much greater than the wavelength and the transverse dimensions are much smaller than the longitudinal, the characteristics of the natural oscillations are completely determined by various dimensionless parameters. In particular, the authors of Ref. 9 used the following dimensionless parameters to calculate the natural oscillations: $c=ka^2/2L$, the Fresnel parameter; $g=1-(2L/R)$, the curvature parameter; $\beta=(4L/a)\cot(\alpha/2)$, the kink parameter of the mirror surface to the axis; and $\tau=b/a$, the relative size of the aperture at the center of the mirror. The physical parameters of the cavity are $\lambda=2\pi/k$, the working wavelength; L, the distance between the mirrors ot the cavity; and R, the radius of curvature of the mirror; α, the ''kink'' angle of the surface of the cavity mirror on the axis; $2a$, the mirror diameter; and $2b$, the diameter of the aperture at the center of the mirror (inset to Fig. 1a).

For the scale modeling it is important to note that there are only four dimensionless parameters, whereas there are six physical parameters. Thus, defining the dimensionless parameters leaves two physical parameters free, which specifically allows us to convert to the most convenient frequency range for the measurements and to select acceptable resonator dimensions.

The characteristics of a crossed-groove cavity were measured in the 8 mm range using apparatus whose block diagram was described in Ref. 11. The model cavity was formed by concave and plane mirrors (inset to Fig. 1a), The concave mirror, having the diameter 118 mm and radius of curvature 170 mm, was turned from brass with the center of curvature displaced from the turning axis by 40 mm. The kink angle of the mirror at the center was 76.4°. The 100 mm plane mirror was known to be larger than the calculated caustic of the dominant oscillation.

The concave mirror with an optical positioning head was mounted on the stage of a horizontal optical comparator whose displacement was measured with an optical microscope to within 5 μm. The circular plane mirror was attached to the fixed part of the comparator. The cavity was excited by a waveguide via a coupling aperture in the concave mirror, 30 mm from the cavity axis, i.e., close to the maximum of the annular oscillation field in confocal geometry.

The excitation source was a frequency-modulated oscillator in the millimeter range. The detected signals from the cavity (via the central coupling aperture in the plane mirror) and the wavemeter consisted of resonance curves and were recorded simultaneously on the screen of a two-channel digital oscilloscope. The measurements were made at a fixed frequency as the concave mirror was moved. The set of measured resonance lines of the natural oscillations L_{mnq} between the center of the concave mirror and the plane mirror determined the cavity spectrum. The Q factor was calculated from the width of the resonance curve and the field distribution was measured by the trial body method.[11]

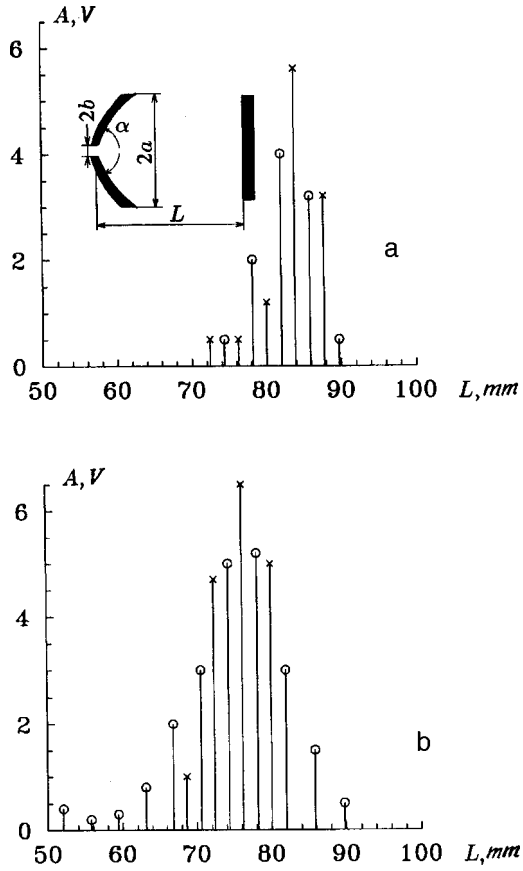

FIG. 1. Spectra of crossed-groove cavity: a—with absorber and b—without absorber. Excitation frequency 43.1 GHz; ○—00q oscillation, ×—11q oscillation; higher oscillation modes are not displayed in the spectra.

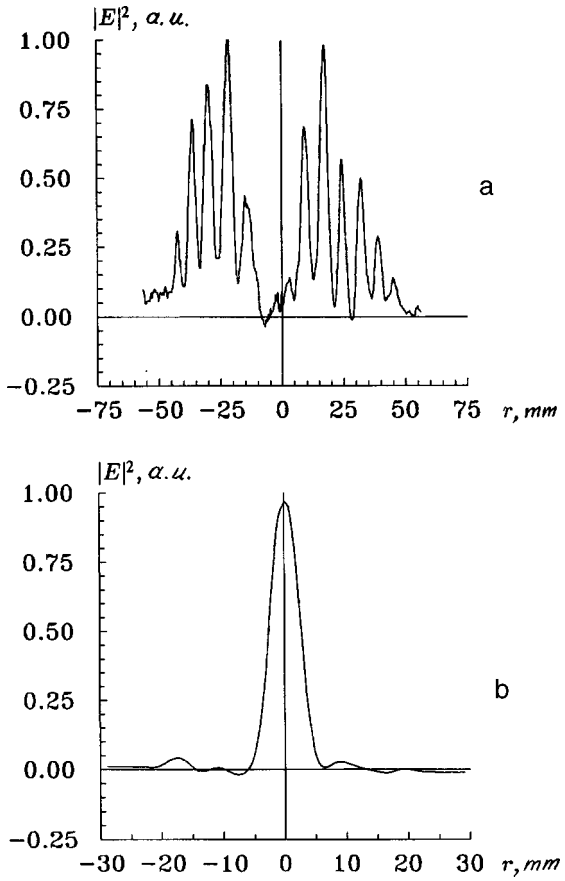

FIG. 2. Results of measurements of the distribution of the dominant oscillation fields in a crossed-groove cavity: a—near concave mirror and b—near plane mirror. Excitation frequency 43.1 GHz.

When the distance L was varied between 28 and 100 nm, several tens of cavities of different amplitude were observed. Only the fairly high-intensity oscillations with Q factors >1000 were investigated. In addition, the dense spectrum of oscillations excited in the ''quasiclosed'' cavity (for $28<L<50$ mm) was not investigated, since this was not of particular interest.

In one of the first series of experiments a cone 1.5 cm in diameter and 1.5 cm high made of plasticene, which is a good absorber in the millimeter wavelength range, was attached to the central part of the concave mirror (the measured reflection coefficient was <0.1). This absorbing insert, which is qualitatively equivalent to an aperture at the center of the mirror, should have the weakest influence on oscillations with a dip in the field near the center of the concave mirror and specifically on annular oscillations and azimuthally nonuniform oscillations with an internal caustic. In fact, the oscillation spectrum of the cavity with an absorbing cone was considerably more widely spaced, which simplified the identification of the oscillation modes by the trial body method.

Figure 1a shows the spectrum of the resonance structure with an absorber in the form of lines whose height is proportional to the amplitude A of the resonance signal and Fig. 1b shows the spectrum without an absorber. In addition to the dominant (annular) oscillation 00q (q is the longitudinal index), we also investigated a series of resonances consisting of two closely spaced oscillations ($\Delta L<0.05$) mm, one of substantially larger amplitude. Measurements of the field distribution of these oscillations showed that they consist of a doubly degenerate azimuthally nonuniform oscillation mode 11q with an internal caustic. As a result of the unavoidable azimuthal asymmetry of the cavity, the degeneracy is lifted and both oscillations, whose fields are shifted azimuthally by 90°, are excited independently.

Figure 2a gives the distribution of the square of the dominant oscillation field measured by stretching a wire with the trial body at right angles to the cavity axis at a distance of around 1 mm near the edge of the concave mirror, and Fig. 2b shows the distribution obtained near the plane mirror. The oscillatory nature of the distribution near the concave mirror is caused by the trial body systematically crossing the concave phase fronts. The radial distribution of the field reflects the envelope of these oscillations.

The results of measurements of the Q factor $Q(L)$ of the annular oscillations are shown in Fig. 3. This dependence is typical of oscillations bounded by external caustics (see Ref. 11). As L increases, the Q factor initially increases as a result of a decrease in the relative fraction of ohmic losses at the mirrors and then increases abruptly as a result of the increased radiation losses as the external caustic approaches the edge of the mirror. The relative radiation losses for the

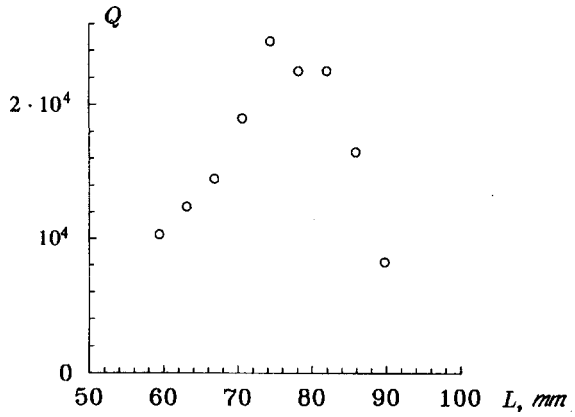

FIG. 3. Q factor of the 00*q* oscillation as a function of distance between mirrors. Excitation frequency 43.1 GHz.

maximum Q factor were $\leqslant 10^{-3}$, which agrees with the calculated estimates.[9]

To conclude, this model experiment has demonstrated the main property of a crossed-groove cavity: the existence of high-Q ring modes having a focused distribution in the central part of the cavity, which provides an additional argument in favor of using this type of cavity in high-power free-electron lasers.

This work was partially supported by the Russian Fund for Fundamental Research (Grants Nos. 96-02-17790-a and 96-15-96956).

[1] G. A. Bogatova, N. V. Cheburkin, and V. V. Perebejnos, Nucl. Instrum. Methods Phys. Res. A **359**, 61 (1995).
[2] N. A. Vinokurov, N. G. Gavrilov, E. I. Gorniker, G. N. Kulipanov, I. V. Kuptsov, G. Ya. Kurkin, G. I. Erg, Yu. I. Levashov, A. D. Oreshkov, S. P. Petrov, V. M. Petrov, I. V. Pinayev, V. M. Popik, I. K. Sedlyarov, T. V. Shaftan, A. N. Skrinsky, A. S. Sokolov, V. G. Veshcherevich, and P. D. Vobly, Nucl. Instrum. Methods Phys. Res. A **359**, 41 (1995).
[3] G. N. Kulipanov, V. N. Litvinenko, A. S. Sokolov, and N. A. Vinokurov, Nucl. Instrum. Methods Phys. Res. A **308**, 106 (1991).
[4] N. G. Gavrilov, G. N. Kulipanov, V. N. Litvinenko, I. V. Pinayev, V. M. Popik, I. G. Silvestrov, A. S. Sokolov, N. A. Vinokurov, and P. D. Vobly, Nucl. Instrum. Methods Phys. Res. A **308**, 109 (1991).
[5] F. F. Baryshnikov, G. A. Bogatova, and V. V. Perebeĭnos, Pis'ma Zh. Tekh. Fiz. **21**(16), 67 (1995) [Tech. Phys. Lett. **21**, 663 (1995)].
[6] N. V. Vinokurov and S. S. Serednyakov, in *Proceedings of the Second Asian Symposium on Free Electron Lasers*, Novosibirsk, 1995, pp. 141–149.
[7] F. F. Baryshnikov, G. A. Bogatova, V. V. Perebeĭnos, and N. V. Cheburkin, Kvant. Elektron. (Moscow) **23**, 349 (1996).
[8] F. F. Baryshnikov, G. A. Bogatova, V. V. Perebeĭnos, and N. V. Cheburkin, Opt. Spektrosk. **81**, 160 (1996) [Opt. Spectrosc. **81** 145 (1996)].
[9] F. F. Baryshnikov, G. A. Bogatova, G. D. Bogomolov, A. I. Kleev, V. V. Perebeĭnos, and N. V. Cheburkin, Kvant. Elektron. (Moscow) **24**(3), 230 (1997).
[10] L. A. Vaĭnshteĭn, *Open Cavities and Open Waveguides*, Golem Press, Boulder, CO (1969); Russian orig., Sovetskoe Radio, Moscow (1966).
[11] G. D. Bogomolov, in *High-Power Electronics 3* [in Russian], Nauka, Moscow (1964), pp. 154–175.

Translated by R. M. Durham

Retention time and memory mechanism in ferrite powders

L. N. Kotov and V. N. Shaporov

Syktyvkar State University
(Submitted August 1, 1997; resubmitted April 8, 1998)
Pis'ma Zh. Tekh. Fiz. **24**, 76–80 (October 12, 1998)

The first results are presented of investigations of the retention time of magnetoacoustic long-term memory signals in ferrite powders for various magnetizing fields and temperatures. A mechanism is proposed to explain how these memory signals form. © *1998 American Institute of Physics.* [S1063-7850(98)01410-4]

Interest in the phenomenon of magnetoacoustic long-term memory (MALM) in an ensemble of small ferrite particles has been stimulated by the possibility of using this effect in memory devices and high-frequency signal converters. This effect may form the basis of a fundamentally new repeatable method of recording and reading information. Information storage devices based on this effect should have a high speed compared with existing devices because of the very short access time.[1]

In the MALM effect, a ferrite powder statically memorizes the echo signals produced by two successive (recording) radiopulses of duration Δ acting on the powder at times $t=0,\tau$ and generates additional signals as a result of the action of a third (readout) pulse at time $t=T\gg\tau$ (Ref. 2). These signals appear at times $t=T+n\tau(n=1,2,3,\ldots)$ and are known as MALM signals.

At present, there are two models capable of explaining the appearance of MALM signals: the reorientation model[3] and the internal model.[4] The reorientation model was used to describe a memory effect in piezoelectric powder and can be essentially transferred to ferrite powders.[3] Thus, we shall only analyze the internal model, which has not been sufficiently discussed in the literature, and we shall also examine the conditions for the formation of MALM signals.

The mechanism for the formation of MALM signals according to the internal model may be described as follows. The electromagnetic field of the first and second exciting pulses of radiation at frequency ω, supplied to the sample at times $t=0,\tau$, excites the elastic subsystem of the particles at the ferromagnetic resonance frequency ω_0 by magnetoelastic coupling. Intensive acoustic vibrations are observed for those particles whose natural frequencies Ω satisfy the condition $\Omega\approx\omega=\omega_0$ (Ref. 4). As a result of nonlinear interaction of the elastic vibrations excited by the recording pulses, the natural frequencies of the oscillators shift. Since the recording of intense signals is observed for almost single-domain particles, a change in the natural frequency of the particles may be related to an irreversible rotation of the magnetization vectors in the particles. The irreversible rotation occurs under the action of two radiopulses acting at times $t=0,\ \tau$. The fairly long precession of the magnetization vector in the powder particles (up to time τ) may be caused by the acoustic vibrations excited by the first pulse. After the action of the readout pulse, the vibrations of the particles for which the natural frequencies have shifted produce the MALM signals.

Here we present results of investigations carried out using a coherent pulsed radio spectrometer with exciting pulses of length 4 μs, interval $\tau=40\,\mu$s, and radiation frequency 18 MHz. The static and alternating magnetic fields were mutually perpendicular. The powder samples were prepared from YIG polycrystals with grain sizes between 2.5 and 5 μm. The powder particles of between 71 and 100 μm were

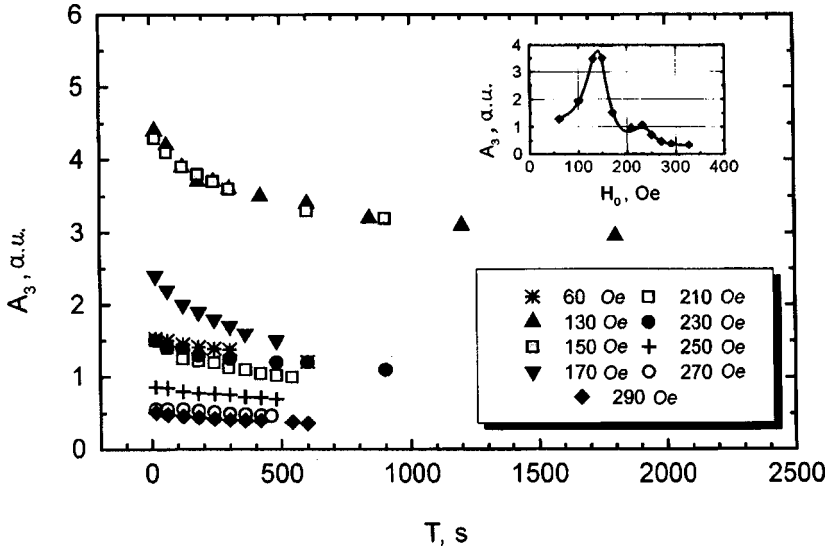

FIG. 1. Amplitude of MALM signals in $Y_3Fe_{4.3}AlO_{12}$ powder with different magnetizing fields. The numbers give the fields in oersted: *1* —60, *2* —130, *3* —150, *4* —170, *5* —210, *6* —230, *7* — 250, *8* —270, and *9* —290. The inset gives the amplitude of the MALM signals as a function of the magnetizing field at time 460 s.

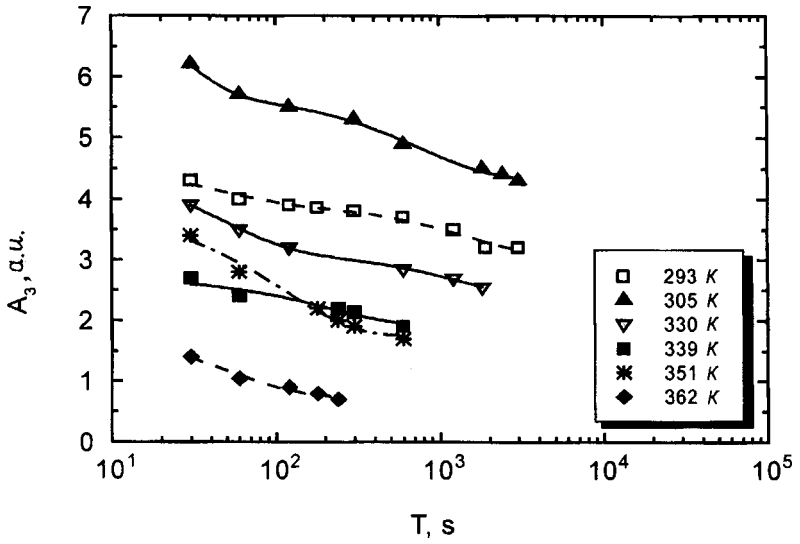

FIG. 2. Amplitude of MALM signals in $Y_3Fe_4Al_{0.7}O_{12}$ ferrite powder at various temperatures in optimum magnetizing fields. The numbers give the temperature in kelvin: *1* —293, *2* —305, *3* —330, *4* —339, *5* —351, and *6* —362.

poured into glass ampoules with a vacuum better than 10^{-4} Torr.

Figure 1 gives the amplitude of the memory signals A_3 as a function of the time of application of the readout pulse for various magnetizing fields H_0 in Al-doped YIG powder having the composition $Y_3Fe_{4.3}Al_{0.7}O_{12}$ with the saturation magnetization $M_s = 52$ G at room temperature.

It can be seen from the inset to Fig. 1, which gives the amplitude of the MALM signals as a function of the magnetizing field H_0 at time $t = 460$ s, that the amplitude A_3 reaches a maximum for fields $H_0 \approx 150$ Oe close to the saturation fields of this sample. In these fields the magnetization vector **M** in the particles is in quasistable equilibrium, in which it can easily be deflected by any angle under the action of the fields of the recording pulses. After the end of these pulses, the magnetization vectors in the particles relax to their initial position, which is responsible for the relatively rapid decay of the signal amplitude with time (Fig. 1). Only a few particles remain in which the vector **M** is fairly reliably retained in the new position, and thus these can have an almost unbounded relaxation time. For large ($H_0 \geqslant 250$ Oe) and small ($H_0 \approx 60$ Oe) magnetizing fields the vector **M** is retained by a fairly strong effective field (in the first case by the magnetizing field and in the second case, by the anisotropy field), so that the probability of its reorientation is low. In this case, the recording takes place in a small number of particles in which the vector **M** is reliably anchored in the new position which is responsible for the relatively small amplitude and weak decay of the MALM signals with time.

The internal model explains the behavior of the curves giving the amplitude of the MALM signals as a function of the readout time in optimum magnetizing fields (fields for which the signals are strongest) at various temperatures, ranging from room temperature to close to the Curie point for a YIG $Y_3Fe_4AlO_{12}$ sample (Fig. 2). The retention time of the MALM signals decreases as the Curie point is approached since the thermal energy approaches the exchange energy and thus the time needed for disordering of the magnetic moments becomes shorter.

We note some other features of the MALM phenomenon which can be described by the internal mechanism. The MALM signals disappear after the sample has been heated above the Curie temperature (and then cooled to room temperature), since the magnetization distribution produced during recording is destroyed. In addition, the experiment showed that the signals observed after heating the powder above the Curie point are several times stronger than those before heating. The explanation for this observation may be that after heating sections with remanent magnetization disappear in the interior of the crystallites, and the magnetization vectors rotate considerably more easily. This also suggests that the recording mechanism can be described by the internal model.

The MALM effect has not been used so far because of the short signal retention time and also because of the damage to the memory signals when the powder is shaken.[3,4] On the basis of these investigations, it can be concluded that first, the storage time of the MALM signals can be arbitrarily long and second, recording can be achieved either as a result of both mechanisms or predominantly as a result of the energetically most favorable mechanism under particular conditions. Thus, under certain conditions recording can be achieved using only the internal mechanism, for example using samples in which the powder particles are distributed in a nonmagnetic matrix, where they cannot rotate but merely vibrate, which solves the problem of loss of information by shaking.

[1] L. N. Kotov, in *Abstracts of Papers presented at the Seventh International Conference on Ferrites*, Bordeaux, France, 1996, p. 444.
[2] V. A. Shutilov, E. V. Charnaya, L. N. Kotov *et al.*, Pis'ma Zh. Tekh. Fiz. **12**, 1060 (1986) [Sov. Tech. Phys. Lett. **12**, 438 (1986)].
[3] R. L. Melcher and N. S. Shiren, *Physical Acoustics*, Vol. 16 (Academic Press, New York, 1982), p. 341.
[4] B. A. Goldin, L. N. Kotov, L. K. Zarembo, and S. N. Karpachev, *Spin–Phonon Interaction in Crystals (Ferrites)* [in Russian], Nauka, Leningrad (1991), 150 pp.

Translated by R. M. Durham

Hydrogen-induced phase transition in barium cerate

Yu. M. Baĭkov, V. M. Egorov, N. F. Kartenko, B. A-T. Melekh, Yu. P. Stepanov, and Yu. N. Filin

A. F. Ioffe Physicotechnical Institute, Russian Academy of Sciences, St. Petersburg
(Submitted May 26, 1998)
Pis'ma Zh. Tekh. Fiz. **24**, 81–84 (October 12, 1998)

The action of water vapor on nominally pure $BaCeO_3$ perovskite at 850 K causes hydrogen to be incorporated into the lattice and a thermally metastable state to form. The lattice symmetry changes as a result of an orthorhombic–pseudocubic transition which takes place at a temperature substantially lower than the known thermally initiated rhombohedral–cubic transition at 1173 K. © *1998 American Institute of Physics.* [S1063-7850(98)01510-9]

The barium cerate studied by us ($BaCeO_3$) has four modifications with transition temperatures of 520–535, 600–670, and 1173 K (Refs. 1–3). Barium cerate is one of the base compounds for the synthesis of high-temperature protonic conductors in which hydrogen is not a dominant chemical component of the oxides and thus is usually incorporated by contact with water vapor. The effectiveness of this procedure depends on the presence of oxygen vacancies in the lattice, produced by acceptor doping (partial substitution of cerium by yttrium or rare earths). For this reason, nominally pure (henceforth called ''pure'') $BaCeO_3$ is of no interest from the technological point of view. However, physical and chemical investigations have revealed differences in the structural characteristics of doped and pure $BaCeO_3$, and it is interesting to understand how these differences relate to the difference in the behavior of hydrogen in pure $BaCeO_3$ and its doped derivatives which we observed in an earlier study.[4] In addition, the consequences of hydrogen incorporation for the structure of barium-cerate based oxides have never been considered, including in our earlier studies,[1,4] where we investigated the properties of pure and doped $BaCeO_3$ synthesized by induction melting.

Here we report the first main results of an investigation of the consequences of thermochemical treatment with water vapor, which allows us to reinterpret the physicochemical processes taking place in high-temperature protonic conductors when they are used industrially and also during physical and chemical investigations. The results refer to the changes in the thermal and structural properties as a result of hydrogen incorporation and also the relationship observed between the rate of hydrogen thermal desorption and the phase transition in $BaCeO_3$.

The initial $BaCeO_3$ obtained by induction melting[1] was ground into powder and normalized by annealing in air (400 Pa moisture content) for 50 h at 800 K. After this treatment the samples were a uniform dark yellow and regardless of the cooling conditions, were characterized as orthorhombic perovskite. The differential scanning calorimetry spectra in the range 300–700 K have two peaks with maxima at 522 ± 1.5 and 607–593 K (boundaries of hysteresis). These thermal effects are interpreted as the result of second-order (522 K) and first-order (607–593 K) phase transitions. The hydrogen content in pure $BaCeO_3$ was <1 at.%.

After normalization, some of the samples were used as a control and some were subjected to thermal vapor treatment: nitrogen containing 0.1% oxygen, 850 K, 100 h, moisture content 3 kPa D_2O (D_2O was used because of the method used subsequently to analyze and observe thermal desorption). After this treatment, the samples were light yellow and conserved their weight and color even when stored in air. The weight of the pure $BaCeO_3$ samples (2 g) remained almost unchanged after the experiment, but isotope exchange data indicated that the hydrogen content in pure $BaCeO_3$ increased to 4 at.%. Moreover, as we showed earlier,[4] molecular hydrogen (here in the form of D_2; the D_2O vapor amounted to $\sim 20\%$) was predominantly released by thermal desorption from pure barium cerate. Since we are interested here in the relationship between phase transitions and hydrogen behavior, particular attention was paid to the temperature at which hydrogen (deuterium) thermal desorption begins.

Despite special measures taken to enhance the sensitivity of the thermal desorption analysis, no release of D_2 or D_2O was detected up to 600 K. The first signs of gas release only appeared at 650 K, and the rate of thermal desorption revealed a distinct jump at 660–680 K. Of particular interest is the observation of thermal desorption in the temperature range after the first-order phase transition (Fig. 1). This may be caused by an increase in the hydrogen (proton) mobility in the lattice and by the initiation of some chemical mechanism which results in the formation of hydrogen molecules from a different chemical (hydroxide) form of hydrogen in the oxide.

A second, but no less interesting, observation is that thermal desorption processes are initiated not only after the phase transition at 607 K but also after the actual end of the heat release as a result of a metastable effect. This effect, which appears after the thermochemical treatment, is observed by differential scanning calorimetry as an exothermic peak in the range 400–750 K and is not noticeable on a second scanning. The energy release of the metastable effect is higher than that of both phase transitions in the same temperature range (950, 230, and 46 J/mol, respectively).

The nature of the metastable effect is not yet clear and we plan to study it. Nevertheless, at the phenomenological

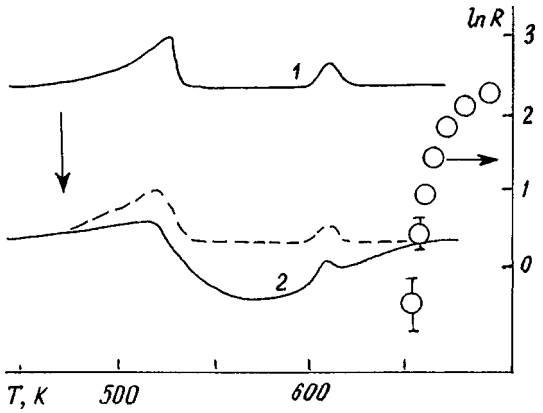

FIG. 1. Differential scanning calorimetry spectra of $BaCeO_3$: normalized (*1*) and after treatment with water vapor (*2*). Dashed curve—second scanning; line of circles—rate of D_2 thermal desorption (R) in arbitrary units.

level, this metastable effect can explain the phenomenon of hydrogen (water) supersaturation during thermal vapor treatment which was described in Ref. 5, since not only the thermal properties of pure $BaCeO_3$ but also the crystal-chemical parameters change in the course of this process. These changes showed up when the x-ray diffraction spectra of pure $BaCeO_3$ samples were compared before and after treatment. The peaks in the range 145–151° ($\theta 2\theta$ geometry, CuK_α radiation), which are fairly typical identifiers of ''fine'' lattice symmetry characteristics of perovskites and are clearly distinguishable for the initial orthorhombic sample, formed a broadened peak in the treated sample. This behavior can be interpreted as the appearance of (pseudo)cubic lattice symmetry after the thermal vapor treatment (see Fig. 2). This observation, made for the first time, also suggests a possible reason for the spread in the lattice parameters and their assignment to different $BaCeO_3$ symmetries by different authors, which we noted in Ref. 1.

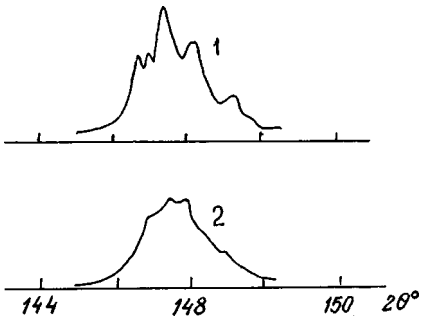

FIG. 2. Part of x-ray diffraction spectrum of $BaCeO_3$ before (*1*) and after (*2*) thermal vapor treatment.

This work was carried out under Russian Fund for Fundamental Research Project No. 97-03-33466a ''Hydrogen in perovskites.''

[1] Yu. M. Baĭkov, V. M. Egorov, N. F. Kartenko *et al.*, Pis'ma Zh. Tekh. Fiz. **22**(11), 91 (1996) [Tech. Phys. Lett. **22**, 476 (1996)].
[2] T. Scherban, R. Villenueve, L. Albello, and G. Lucazeau, J. Raman Spectrosc. **24**, 805 (1993).
[3] K. S. Knight, Solid State Ionics **74**, 109 (1994).
[4] Yu. M. Baikov, Solid State Ionics **97**, 471 (1997).
[5] K. D. Kreuer, E. Schonherr, and J. Maier, Solid State Ionics **70–71**, 278 (1994).

Translated by R. M. Durham

Preparation and investigation of films of $(Zn_{1-x}Cd_x)_3(P_{1-y}As_y)_2$ solid solutions

V. M. Trukhan, V. F. Gremenok, V. V. Rubtsov, and I. A. Viktorov

Institute of Solid-State and Semiconductor Physics, Belarus National Academy of Sciences, Minsk
(Submitted December 29, 1997)
Pis'ma Zh. Tekh. Fiz. **24**, 85–88 (October 12, 1998)

Pulsed laser evaporation was used to prepare thin films of $(Zn_{1-x}Cd_x)_3(P_{1-y}As_y)_2$ solid solutions. It was shown that varying the flux density of the laser radiation and the substrate temperature allows films to be obtained whose composition, structure, and electrical properties are similar to those of the bulk samples. © *1998 American Institute of Physics.* [S1063-7850(98)01610-3]

In recent years increasing interest has been shown in film samples of II_3-V_2 semiconductors in connection with fundamental aspects of studying their physical properties and also because of the possibility of using thin films in semiconductor and quantum electronics.[1,2] It should be noted that II_3-V_2 solid solutions are of particular interest, since they can operate in a range of compositions free from the polymorphic transitions typical of this group of compounds.[2]

The preparation of films of complex semiconductor compounds encounters problems with deviations of the composition from stoichiometry caused by dissociation of the materials during the evaporation process. Consequently, in many cases, conventional methods of preparing thin films (thermal deposition, cathode sputtering, and so on) are unsuitable. Pulsed laser evaporation was used here to obtain films of $(Zn_{1-x}Cd_x)_3(P_{1-y}As_y)_2$ solid solutions. This technology is considered to have many advantages over conventional methods of deposition.[3] Here we present results of an investigation of the structure and electrical properties of thin layers of different compositions. The choice of solid solution compositions was determined on the basis of an earlier component optimization of crystal samples for use as elements of Hall detectors.[4]

The initial materials for the deposition process were polycrystalline samples of $(Zn_{1-x}Cd_x)_3(P_{1-y}As_y)_2$ solid solutions grown by a single-temperature method with vibrational mixing and by a two-temperature method with different temperature gradients along the furnace. The substrates were chemically purified Corning 7059 glasses and their temperatures were sustained in the range $T_l = 50-300\,^{\circ}C$. The films were deposited in a vacuum chamber at a residual gas pressure of $(4-6)\times10^{-5}$ Torr using a free-running industrial laser (pulse length 10^{-3} s, wavelength 1.06 μm) (Ref. 5). The laser radiation power was 10^5–(5×10^5) W/cm^2. Depending on the number of laser pulses, the thickness of the film varied between 0.2 and 1.5 μm.

It was established that the surface quality of the films obtained by pulsed laser evaporation depends very strongly on the lens–target distance, i.e., on the flux density of the laser radiation at the surface of the target. By using defocused radiation, we obtained solid-solution films with a mirror-smooth surface, almost free from droplets and pinholes. In this case, the flux density of the laser radiation was $(1.3-1.6)\times10^5$ W/cm^2 and shallow holes formed in the target (the depth of the holes is much less than their transverse dimensions).

The composition and structure of the targets and films were monitored by microstructural and x-ray phase analysis. It was established that the composition of thin films obtained from stoichiometric targets depends on the substrate temperature.[6] At temperatures above 250 °C the films were 10–20% depleted in phosphorus and arsenic relative to the target. The ratio of zinc to cadmium was accurately reproduced in this temperature range within 4% measurement er-

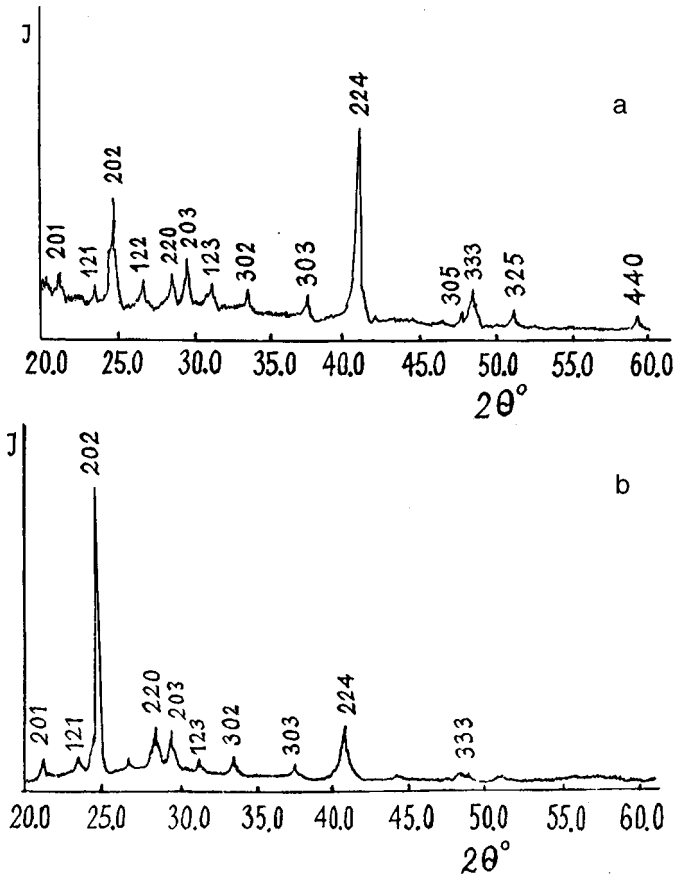

FIG. 1. X-ray diffraction patterns: a—powder sample of $(Zn_{0.265}Cd_{0.735})_3(P_{0.1}As_{0.9})_2$ solid solution; b—films obtained at a substrate temperature of 240 °C.

TABLE I.

Film composition	T_l, °C	ρ, Ω cm	n, cm^{-3}	μ, $cm^2\ V^{-1}\ s^{-1}$
$(Zn_{0.23}Cd_{0.77})_3$	100	48.0	4.8×10^{14}	270.5
$(P_{0.23}As_{0.77})_2$	240	11.1	1.2×10^{15}	626.2
$(Zn_{0.27}Cd_{0.73})_3$	100	27.5	1.4×10^{15}	383.7
$(P_{0.10}As_{0.90})_2$	240	7.9	3.3×10^{16}	887.4

ror. Investigations of the structure and phase composition of the films showed that at low substrate temperatures (50–150 °C) crystalline layers grow, although the diffraction peaks were of low intensity and broadened. This suggests substantial crystal lattice defects. At substrate temperatures above 200 °C the intensity of the peaks increases and their width decreases.

Figure 1a shows an x-ray diffraction pattern for a powder target having the composition $(Zn_{0.265}Cd_{0.735})_3(P_{0.1}As_{0.9})_2$ and Fig. 1b shows that for a film grown at $T_l = 240$ °C. It can be seen that the film and the target have identical structures and phase composition, while the films of these solid solutions reveal a clearly defined texture in the ⟨202⟩ direction. The crystal lattice parameters of the target and the film determined by the least squares method were almost the same ($a = 8.7664$ Å and $c = 12.3879$ Å).

The electrical characteristics of the thin layers were investigated at room temperature by the van der Pauw method. It was found that the films possessed *n*-type conductivity and their parameters are given in Table I as a function of the composition and deposition temperature.

It can be seen that the substrate temperature strongly influences the electrical characteristics of thin solid solutions of II_3V_2 semiconductors; this is directly related to the structure and composition of the laser-deposited layers.

To sum up, pulsed laser evaporation has been used to obtain films of $(Zn_{1-x}Cd_x)_3(P_{1-y}As_y)_2$ solid solutions whose composition and structure are similar to those of the bulk materials. Preliminary results of electrical measurements indicate that these films are potentially useful as magnetoactive elements of magnetic field meters.

This work was supported financially by the Belarus Fund for Fundamental Research.

[1] S. F. Marenkin, A. V. Maĭmasov, and V. A. Popov, in *Abstracts of Papers presented at the Fifth International Conference on Thermodynamics and Material Science of Semiconductors* [in Russian], Moscow (1997), p. 95.
[2] V. B. Lazarev, V. Ya. Shevchenko, and Ya. Kh. Grinberg, *III–V Semiconductor Compounds* [in Russian], Nauka, Moscow (1987), 170 pp.
[3] A. N. Pilyankevich, Yu. A. Bykovskiĭ, and M. V. Loshchinskiĭ, Preprint: *Laser Deposition of Thin Films*, Kiev (1980), 33 pp.
[4] V. A. Rubtsov, V. M. Trukhan, and V. N. Yakimovich, Dokl. Akad. Nauk BSSR **54**, 837 (1990).
[5] É. E. Matyas, V. F. Gremenok, and V. M. Trukhan, Fiz. Tekh. Poluprovodn. **25**, 1656 (1991) [Sov. Phys. Semicond. **25**, 1000 (1991)].
[6] V. M. Trukhan, V. F. Gremenok, and V. A. Rubtsov, Neorg. Mater. (1998) (in press).

Translated by R. M. Durham

Preparation of thick $YBa_2Cu_3O_{7-\delta}$ films by dc magnetron sputtering

E. K. Hollmann, D. A. Plotkin, S. V. Razumov, and A. V. Tumarkin

St. Petersburg State Electrotechnical University
(Submitted April 10, 1998)
Pis'ma Zh. Tekh. Fiz. **24**, 89–94 (October 12, 1998)

High-temperature superconducting films up to 3.6 μm thick were obtained and their properties requisite for the development of microwave devices were investigated. It is shown that $YBa_2Cu_3O_{7-\delta}$ films of thickness exceeding $3-5\,\lambda_L$ may be obtained for use in the microwave range. © *1998 American Institute of Physics.* [S1063-7850(98)01710-8]

INTRODUCTION

Films of good structural quality with high critical parameters are required to fabricate microwave devices using the high-temperature superconductor $YBa_2Cu_3O_{7-\delta}$. In order to localize the field in the film and reduce the microwave losses, the thickness of the film should exceed a few London penetration depths λ_L. For an ideal $YBa_2Cu_3O_{7-\delta}$ (YBCO) crystal oriented with the *c* axis of the unit cell perpendicular to the surface (*c*-orientation), the value of λ_L according to various sources is between 1400 and 1800 Å (Ref. 1) and increases in the presence of any structural defects in the film, for example, as a result of the inclusion of differently oriented grains. This implies that films at least 0.5 μm thick are required for microwave applications.

In our previous studies[2,3] we examined the problems involved in obtaining thick YBCO films and we reported results of an investigation of films 0.1–2.6 μm thick obtained by dc magnetron sputtering. Here we report results for YBCO films up to 3.6 μm thick prepared by magnetron sputtering at a deposition rate of $\sim$15 Å/min. The films were investigated by x-ray diffraction analysis, electron microscopy, and Rutherford backscattering.

EXPERIMENT

The films were deposited in a planar dc magnetron system using a sapphire substrate with a cerium dioxide sublayer.[4] The pressure of the oxygen working gas was 1 Torr. The temperature of the substrate holder was maintained at 650 °C and remained constant during the process. The discharge current increased from 100 to 600 mA during the first 30 min of the process and then remained constant. The film deposition time was between 1 and 40 h. The thickness of the deposited films was measured using a Dektak-3030 profilometer and the estimated growth rate was 15 Å/min ± 5%. The parameters of the films are given in Table I.

TABLE I.

Sample No.	Discharge current, mA	Deposition time, h	Thickness, μm
654	600	20	1.8
656	600	14	1.26
657	600	1	0.1
665	600	6.2	0.56
667	600	40	3.6

RESULTS AND DISCUSSION

The structural quality of the samples was investigated by x-ray diffraction analysis (Geigerflex series *D*/max–RC Rigaku, $\lambda = 1.5418$ Å CuK_α radiation). The diffraction patterns of the films clearly show all (00*l*) peaks, indicating a perfect *c*-oriented structure. The (*h*00) peaks, which indicate the presence of *a*-oriented grains, are only observed in the x-ray diffraction pattern of the 0.1 μm thick sample, which confirms that, in terms of preferential orientation, the quality of the films deposited under these conditions improves with increasing thickness.[2]

Figure 1 gives the full-width at half-maximum (FWHM) of the (005) peak. The tendency of the peak width to decrease with increasing film thickness up to $\sim$1.3 μm suggests that the crystal quality of the films improves. The subsequent broadening of the peak and corresponding deterioration of the structure may be attributed to the evolution of a surface relief which becomes particularly appreciable at large thicknesses (see Fig. 3).

Figure 2 gives the *c* parameter of the films calculated from the (0011) peak as a function of thickness compared with data for films obtained at deposition rates of 3 and

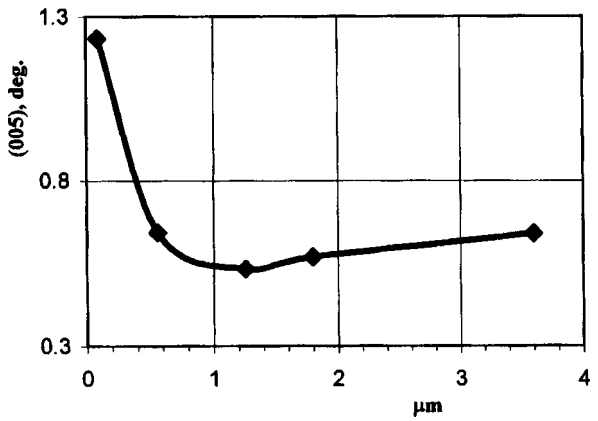

FIG. 1. FWHM of $YBa_2Cu_3O_{7-\delta}$(005) peak on rocking curve ($\Delta\omega$) as a function of film thickness.

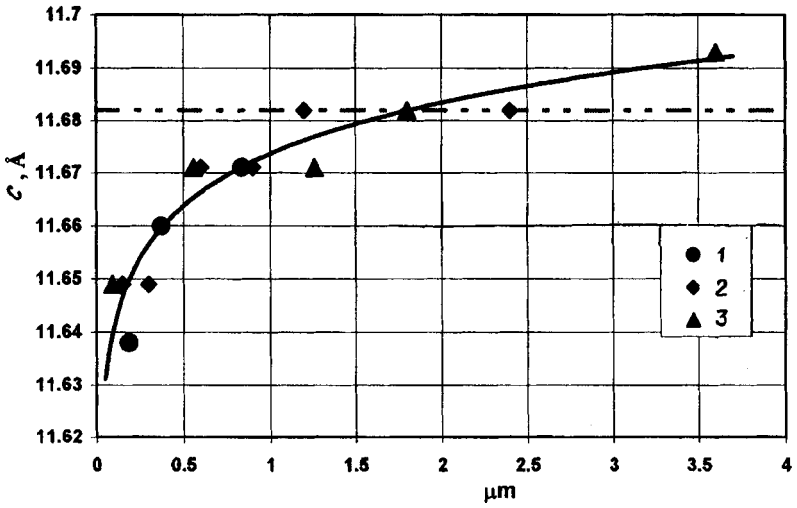

FIG. 2. The *c* parameter versus film thickness. Deposition rate: *1*—3, *2*—10, and *3*—15 Å/min.

10 Å/min (Refs. 2 and 3). The general tendency of the *c* parameter to increase with thickness allows us to assess the oxygen content in the $YBa_2Cu_3O_{7-\delta}$ film and suggests that from the point of view of the correspondence between the oxygen flux and the Y, Ba, and Cu fluxes, the conditions created by a deposition rate of 10 Å/min are preferable.

The surface morphology of the films was investigated by scanning electron microscopy. The photographs shown in Fig. 3 illustrate the change in the surface of the film with increasing thickness: the evolution of a relief where the pore size and the fraction of the film area occupied by pores increases while the concentration of inclusions remains approximately constant. In our previous studies[2,3] we put forward the hypothesis that the improvement in film quality with thickness is attributed to the formation of macrodefects, pores and dielectric inclusions, which may act as sinks for defects and superstoichiometric atoms and improve the electrophysical properties.[1] For the 3.6 μm thick sample (Fig. 3a) we can postulate that the presence of a highly developed surface relief has a negative influence on the structural quality, i.e., there is a certain optimum concentration of macrodefects (see the corresponding film characteristics in Figs. 1 and 2), which is achieved for films around 1.5 μm thick.

The surface layer of the films was investigated by Rutherford backscattering[5] and the results are plotted in Fig. 4. The parameter χ, which characterizes the ratio of channeled and random reflected signals, increases as the concentration of defects, grain boundaries, and lattice misorientation increases. It may be postulated that the dielectric inclusions influence the ratio of the channeled and random spectra in proportion to their concentration and size. The curves plotted in Fig. 4 give the parameter χ at a depth of $\sim$50 nm as a function of the film thickness, obtained at deposition rates of 3 and 15 Å/min. These results broadly confirm our hypothesis that the dielectric inclusions and the structural properties of the films are interrelated.

CONCLUSIONS

We have shown that YBCO films of thickness considerably exceeding $3-5\lambda_L$ can be obtained. The maximum film thickness giving satisfactory quality for microwave applications is $\sim$2 μm at a growth rate of 15 Å/min and deposition time of around 20 h. A film thickness of around 1 μm is sufficient for microwave applications and although such films of satisfactory quality were obtained in all the deposition regimes studied (deposition rates between 3 and 15 Å/min), the regime giving the better deposition rate is preferable.

This work was supported by the BMBF/VDI Project No. 029850 (Germany).

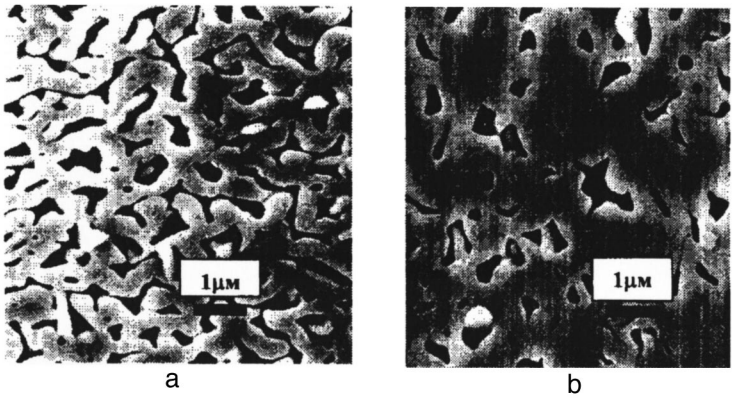

FIG. 3. Photomicrographs of the surface of films of different thickness (a—sample 1.8 μm thick and b—sample 1.26 μm thick.

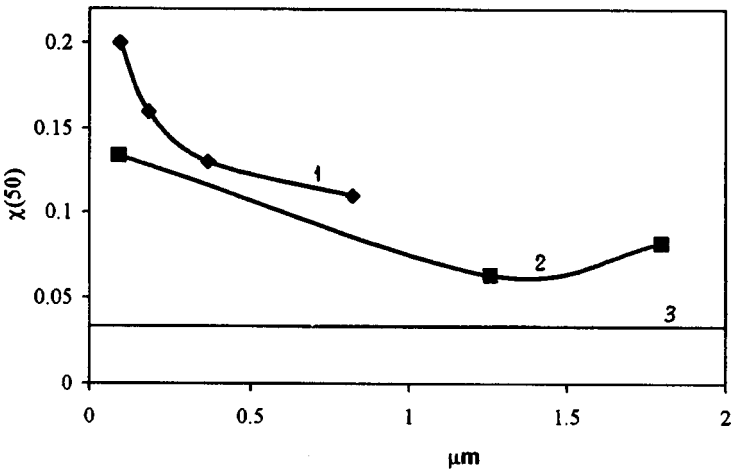

FIG. 4. Ratio of random and channeled RBS signals as a function of film thickness. Deposition rates: *1*—3, *2*—15 Å/min, *3*—for single crystal ~0.03.

The authors are grateful to I. T. Serenkov and R. I. Il'in for assistance with the investigations and discussions of the results.

[1] Y. J. Tian, L. P. Guo, L. Li *et al.*, Appl. Phys. Lett. **65**, 234 (1994).
[2] E. K. Hollmann, V. I. Gol'drin, V. E. Loginov *et al.*, Pis'ma Zh. Tekh. Fiz. **23**(5), 39 (1997) [Tech. Phys. Lett. **23**, 186 (1997)].
[3] E. K. Hollmann, D. A. Plotkin, S. V. Razumov *et al.*, Physica C (1998) (to be published).
[4] E. K. Hollmann, A. G. Zaitsev, V. E. Loginov *et al.*, J. Phys. Physica D **26**, 504 (1993).
[5] V. V. Afrosimov, E. K. Gol'man, R. N. Il'in *et al.*, Pis'ma Zh. Tekh. Fiz. **24**(1), 91 (1998) [Tech. Phys. Lett. **24**, 41 (1998)].

Translated by R. M. Durham

Physical model for shock-wave initiation of detonation in pressed fine crystalline explosives

K. F. Grebenkin

Scientific-Research Institute of Technical Physics, Snezhinsk
(Submitted February 3, 1998)
Pis'ma Zh. Tekh. Fiz. **24**, 1–5 (October 26, 1998)

A physical model is proposed for the reaction kinetics of heterogeneous explosives under shock-wave initiation of detonation. The model is based on the assumption that the molecular crystals of the explosive materials have semiconductor properties. The model can account for the experimentally observed strong dependence of the shock-wave sensitivity of pressed explosives on their initial density and temperature. The proposed model can be checked by measuring the band gaps of triaminotrinitrobenzene (TATB) and comparing with the value of 40 kcal/mole obtained in the present study from an analysis of explosion experiments.
 [S1063-7850(98)01810-2]

It is well known that the critical pressure for initiating detonation in heterogeneous explosives obtained by the pressing of fine-crystalline initial materials is several times lower than in single-crystal samples of the same materials. This is because the pressed explosives have porosity, and the pressure of the shock wave causes collapse of the pores, a local rise in temperature, and rapid burnup of the explosive in the overheated zones (hot spots). After this the combustion wave propagates from these hot spots into the remaining part of the explosive.[1]

Although the concept of ingnition from hot spots in the shock-wave initiation of heterogeneous explosives is not itself in doubt, some fundamental questions remain unanswered as to the physical mechanism that governs the velocity of the combustion wave, the microscopic description of the experimentally observed strong dependence of the delay in the initiation of heterogeneous explosives on their initial density and temperature, and, finally, the relation between the sensitivity and the molecular structure of the explosive.

In this paper we propose a physical model for the process of shock-wave initiation of a heterogeneous explosive, based on the assumption that the kinetics of the initiation is governed by the width of the band gap of the molecular crystals of the explosive material. Indeed, if it is assumed that the propagation of the combustion wave from the hot spots occurs on account of heat conduction, the velocity of the combustion wave can be estimated as[2]

$$D \approx \sqrt{\chi/\tau},$$

where χ is the thermal diffusivity of the explosive outside the hot spots, and τ is the time for the reaction to take place in the layer of explosive heated from the locus. The temperature dependence of the thermal conductivity of a nonmetal has the form[3]

$$\chi = \chi_0 \exp(-\varepsilon_g/2RT),$$

where ε_g is the width of the band gap and χ_0 is a constant. It follows that the velocity of the combustion wave can be written in the form

$$D = D_0 \exp(-\varepsilon_g/4RT),$$

where D_0 is a constant.

The characteristic burnup time of an explosive can be estimated as $t_x \approx R/D$, where R is twice the average distance between hot spots. If the characteristic size of a pore is r, then $R \approx r/\alpha^{1/3}$, where α is the porosity of the explosive, i.e., the volume fraction of pores.

Proceeding from these considerations, we can propose the following equation for the macrokinetics of the reaction of a heterogeneous explosive under shock-wave initiation:

$$-\frac{1}{W}\frac{dW}{dt} = \frac{1}{t_x} = Z\alpha^{1/3}\exp(-E_a/RT). \quad (1)$$

Here W is the concentration of the explosive, T is the temperature of the medium, R is Boltzmann's constant, and Z and E_a are parameters of the model.

Although expression (1) is outwardly similar to the Arrhenius law, this similarity is only formal, since the principal parameter of the model E_a is not related to any chemical reaction but is determined by the band structure of the molecular crystal of the explosive: $E_a = \varepsilon_g/4$.

We note that calculation of the temperature of the explosive material for insertion in Eq. (1) is a nontrivial problem and requires correct allowance for such factors as the initial porosity and the temperature dependence of the specific heat of the explosive.

The explosives of the greatest practical interest are based on nitro compounds, e.g., TNT, triaminotrinitrobenzene (TATB), HMX, RDX, etc. It is known that the molecular crystals of nitro compounds can have semiconducting properties with a band gap of the order of 1 eV.[4] Consequently, $E_a \approx 6$ kcal/mole, which is an order of magnitude lower than the activation energy for thermal initiation of an explosive.[5]

To verify model (1) we carried out a numerical simulation of the initiation of TATB under the experimental conditions of Ref. 6, using a one-dimensional Lagrangian gasdynamic code with chemical reaction kinetics in the form (1).

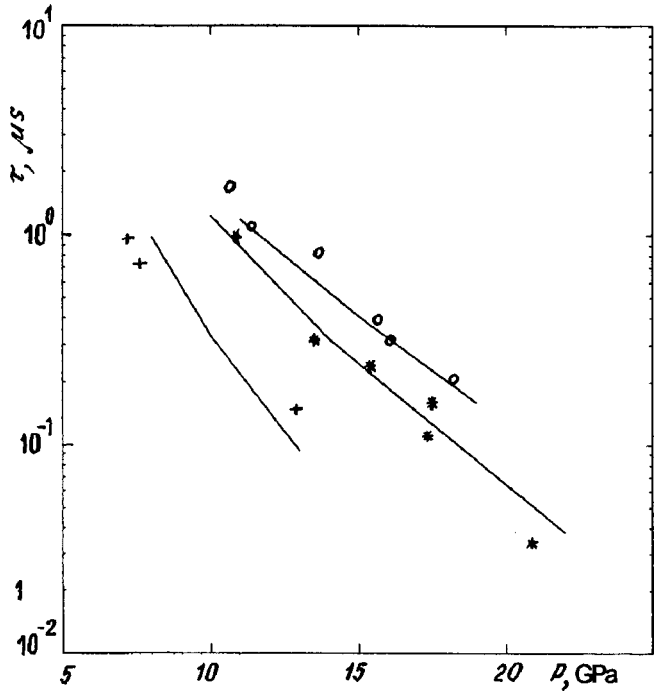

FIG. 1. Delay time of the initiation of detonation of TATB versus the pressure at the shock wave front for different values of the initial density: 1.92 g/cm^2 (○ — experiment,[6] top line — calculation), 1.90 g/cm^3 (* — experiment,[6] middle line — calculation), and 1.81 g/cm^3 (+ — experiment,[6] bottom line — calculation).

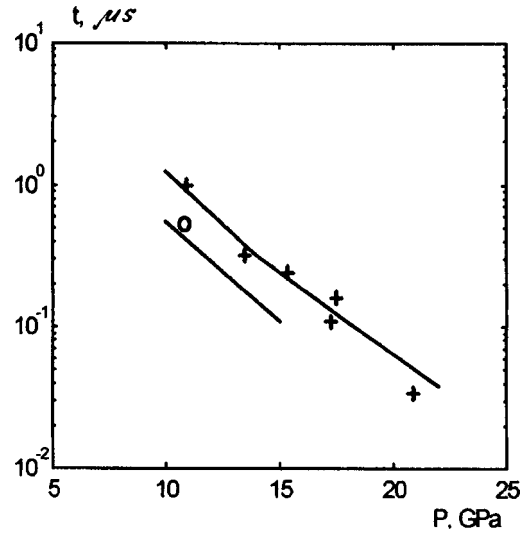

FIG. 2. Delay time for the initiation of detonation of TATB versus the pressure at the shock wave front for different values of the initial temperature and density: $T=+68°$C, $\rho=1.88$ g/cm^3 (○ — experiment,[6] upper line — calculation), $T=+20°$C, $\rho=1.90$ g/cm^3 (+ — experiment,[6] lower line — calculation).

Figure 1 shows a comparison of the calculated and experimental pressure dependence of the delay time of the initiation of detonation for various initial densities of the explosive. Figure 2 shows the analogous results obtained for a different initial temperature of the explosive. It can be stated that the proposed model reproduces the experimental data in an entirely satisfactory manner. The value of the apparent activation energy of TATB estimated from the results of the analysis was $E_a \approx 10$ kcal/mole, from which one can estimate that the band gap in the TATB crystals is around 40 kcal/mole. According to estimates, for RDX and HMX crystals the band gap is one-half as large as in TATB. This probably accounts for their higher shock-wave sensitivity as compared to TATB.

In summary, the proposed model makes it possible to establish a relation between the shock-wave sensitivity and band structure of high-energy molecular crystals. To check the proposed model it would be helpful to measure the band gaps of TATB crystals and other nitro compounds used as explosives.

[1] G. I. Kanel', S. V. Razorenov, A. V. Utkin, and V. E. Fortov, *Shock-Wave Phenomena in Condensed Media* [in Russian], Yanus-K, Moscow (1996).
[2] L. D. Landau and E. M. Lifshitz, *Fluid Mechanics*, 2nd ed., Pergamon Press, Oxford (1987) [Russian original, Nauka, Moscow (1986)].
[3] C. Kittel, *Introduction to Solid State Physics*, 4th ed., Wiley, New York (1976); Nauka, Moscow (1978).
[4] J. Simon and J.-J. Andre, *Molecular Semiconductors: Photoelectrical Properties and Photocells*, Springer-Verlag, Berlin–New York (1985); Mir, Moscow (1988).
[5] C. L. Mader, *Numerical Modeling of Detonations*, University of California Press, Berkeley (1979); Mir, Moscow (1985).
[6] P. Jackson, L. Green, R. Barlett *et al.*, ''Characteristics of the initiation and propagation of detonation in the explosive TATB,'' in *Detonation and Explosive Materials* [in Russian], Mir, Moscow (1981), pp. 323–342.

Translated by Steve Torstveit

Active microwave pulse compressor utilizing an axisymmetric mode of a circular waveguide

A. L. Vikharev, A. M. Gorbachev, O. A. Ivanov, V. A. Isaev, S. V. Kuzikov, A. L. Kolysko, and M. I. Petelin

Institute of Applied Physics, Nizhniĭ Novgorod
(Submitted April 14, 1998)
Pis'ma Zh. Tekh. Fiz. **24**, 6–11 (October 26, 1998)

A novel active microwave pulse compressor in the form of an axisymmetric cavity is implemented and investigated. The cavity is formed by: a) a Bragg reflector, b) a cylindrical section, and c) an output resonance reflector in the form of an electrically controlled gas-filled spark gap. The compressor is excited by the TE_{01} mode of a circular waveguide at a frequency of 9.4 GHz. Working at atmospheric pressure, the compressor produces output pulses with a power of 1.8 MW and duration 25 ns at a compression coefficient of around 20.
 [S1063-7850(98)01910-7]

1. INTRODUCTION

One of the ways currently employed to obtain high-power microwave pulses is to use Q-switched storage cavities[1–4] with interference Q-switches: electrically controlled or self-breakdown waveguide H-tees. Such compressors can yield microwave pulses with powers of up to 200 MW in single-stage compression at frequencies of the order of 3 GHz. However, on scaling to higher frequencies the power of such compressors falls off rapidly. In Ref. 5 it was proposed to use axisymmetric modes of oversized Bragg resonators to increase the power of the compressed high-frequency pulses. The switching of the Bragg reflector could be effected, in particular, by a distributed set of electrically controlled gas-discharge tubes. Here it is obviously necessary that the plasma arising upon breakdown in the gas have a high degree of homogeneity. This requirement can be relaxed somewhat if the electrodynamic structure of the output reflector has resonance properties such that a relatively small change in the parameters of the medium filling the tube is sufficient to destroy the resonance. This method can be implemented in an axisymmetric microwave compressor working on the TE_{01} mode and utilizing a controllable output reflector in the form of a waveguide expansion containing a gas-filled spark gap. In the expansion the blocked mode creates a reflection with a reflection coefficient close to unity in a frequency band determined by the loaded Q of the waveguide expansion.[6] By choosing the configuration of the waveguide expansion one can, without reaching the self-breakdown threshold of the gas-discharge tube, effect a controlled switching of the compressor with a minimal volume of gas-discharge plasma. We note that the use of the TE_{01} mode is favorable from the standpoint of achieving both high dielectric strength and low wall losses in the compressor.

2. CONSTRUCTION OF THE MICROWAVE COMPRESSOR

The axisymmetric compressor investigated in this study (Fig. 1) consisted of an input Bragg reflector, a section of cylindrical waveguide 1 m long and 50 mm in diameter, and an output reflector, based on an abrupt expansion of the circular waveguide[6] enclosing a gas-filled spark gap. The input Bragg reflector is a section of cylindrical waveguide with a diameter of 50 mm and a shallow sinusoidal corrugation. The center frequency of the reflector was equal to 9.4 GHz, and the width of the stop band (at half maximum of the transmitted power) was 600 MHz. Near the center frequency the power reflection coefficient was $98.5 \pm 0.5\%$. The output reflector (Fig. 2) was in the form of a cylindrical cavity 130 mm in diameter, resonant for the TE_{021} mode. Near the front wall of the cavity was a quartz gas-discharge tube in the form of a ring 120 mm in diameter. The tube had a cross

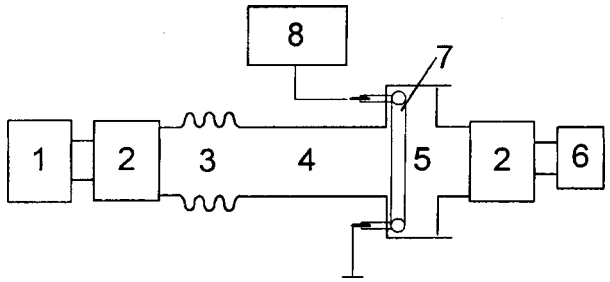

FIG. 1. Block diagram of the compressor: *1* — microwave oscillator, *2* — waveguide transformer, *3* — input Bragg reflector, *4* — cylindrical waveguide section, *5* — controlled reflector, *6* — load, *7* — gas-discharge tube, *8* — high-voltage pulse generator.

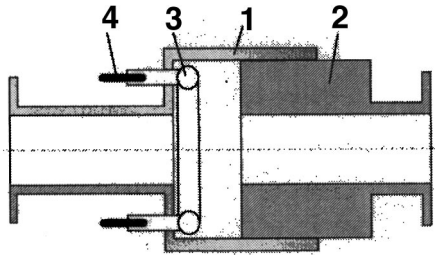

FIG. 2. Output resonance reflector: *1* — waveguide of diameter 130 mm, *2* — waveguide of diameter 50 mm, *3* — quartz ring tube, *4* — electrode.

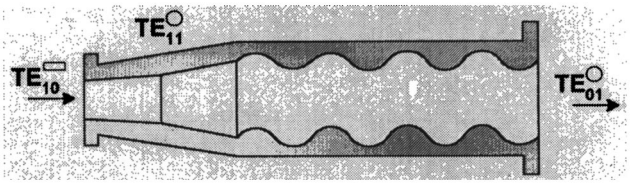

FIG. 3. Converter of the $TE_{10}^{\square}$ of a rectangular waveguide to the mode $TE_{01}^{\bigcirc}$ of a circular waveguide.

section of 10 mm and was fitted with two branch pipes for the admission and evacuation of air, the pressure of which was varied from 1 to 10 Torr. A discharge was struck in the tube through two diametrically opposed eds, on which a pulse of amplitude 40 kV, duration 100 ns, and rise time of 10 ns was applied. The width of the resonance curve of the storage cavity as a unit, measured at a frequency of 9.4 GHz, was $\Delta f = 0.6$ MHz, which corresponds to a loaded Q factor $Q = 1.5 \times 10^4$. The storage cavity was excited from a magnetron with an output power of up to 130 kW, a microwave pulse duration $\tau = 5\ \mu$s, and a repetition rate $F = 1$ Hz. The power was extracted from the magnetron in the TE_{10} mode of a rectangular waveguide. This wave was converted to the TE_{11} mode of a circular waveguide at an adiabatic transition, and the latter then entered a waveguide with a slight corrugation which was sinusoidal in the plane of the wide wall of the initial rectangular waveguide (Fig. 3), where it was converted[7,8] to the TE_{01} mode.

3. EXPERIMENTAL RESULTS

A preliminary tuning of the compressor was accomplished by adjusting the length of the cylindrical section with the aid of a sweep generator so that the minimum of the microwave signal reflected from the compressor lay at the working frequency of the magnetron. The tuned compressor was fed from the magnetron through a circulator. At the end of the supply pulse a pulse of high voltage was applied to the electrodes of the quartz tube. The appearance of a plasma in it altered the eigenfrequency and Q of the output reflector, leading to a rapid increase in the transmission coefficient. Energy was emitted from the compressor in the TE_{01} mode of a circular waveguide. In the experiment we varied both the air pressure in the spark gap and the magnitude of the high-voltage control pulse, so that, in addition to the rise time of the voltage, the propagation velocity of the ionization front in the tube was determined, according to Ref. 9. The maximum coefficient of compression (the ratio of the powers of the compressed and primary pulses) was 13–14 dB; the duration of the compressed microwave pulse at half maximum was 25–30 ns (Fig. 4). The results of the experiment are summarized in Table I. The width of the output spectrum of the magnetron used was 1.3 MHz, which is twice the width of the resonance curve of the storage cavity; this circumstance is mainly what limited the efficiency of the compressor. The power of the compressor was limited by the fact that its main volume was filled with air at atmospheric pressure. Estimates show that evacuating the compressor or, alternatively, increasing the gas pressure in it while increasing the power of the primary pulses to 1 MW and increasing the pressure in the gas-discharge tube to a value of the order of 100 Torr (to avoid self-breakdown), one can raise the output power level to several tens of megawatts.

TABLE I. Results of the compressor tests.

Frequency	9.4 GHz
Working mode	$TE_{01}^{\bigcirc}$
Q of the cavity	1.5×10^4
Input power	90 kW
Output power	1.8 MW
Duration of output pulse	25 ns
Efficiency	30%

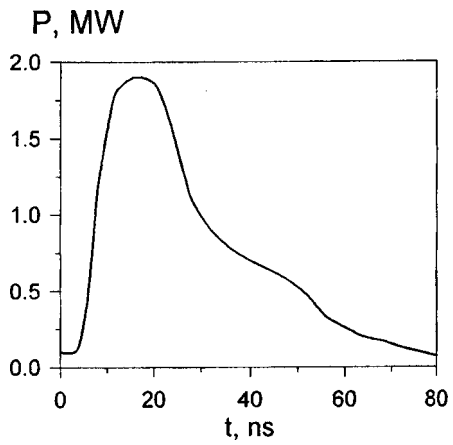

FIG. 4. Oscilloscope trace of the microwave output pulse.

The authors thank V. E. Balakin, N. F. Kovalev, A. G. Litvak, and D. Clooney (England), and J. Hirschfield (USA) for helpful discussions.

[1] A. N. Didenko and Yu. G. Yushkov, *High-Power Microwave Pulses of Nanosecond Duration* [in Russian], Énergoatomizdat, Moscow (1984), 112 pp.
[2] A. N. Didenko, S. A. Novikov, S. V. Razin, P. Yu. Chumerin, and Yu. G. Yushkov, Dokl. Akad. Nauk SSSR **321**, 518 (1991) [Sov. Phys. Dokl. **36**, 792 (1991)].
[3] R. A. Alvarez, D. P. Byrne, and R. M. Johnson, Rev. Sci. Instrum. **57**, 2475 (1986)].
[4] V. A. Avgustinovich, S. A. Novikov, S. V. Razin, and Yu. G. Yushkov, Izv. Vyssh. Uchebn. Zaved. Radiofiz. **28**, 1347 (1985).
[5] A. L. Vikharev, N. F. Kovalev, and M. I. Petelin, Pis'ma Zh. Tekh. Fiz. **22**(19), 41 (1996) [Tech. Phys. Lett. **22**, 795 (1996)].
[6] G. G. Denisov, S. V. Kuzikov, and D. A. Lukovnikov, Int. J. Infrared Millim. Waves **16**, 1231 (1995).
[7] N. F. Kovalev, I. M. Orlova, and M. I. Petelin, Izv. Vyssh. Uchebn. Zaved. Radiofiz. **11**, 783 (1968).
[8] S. V. Kuzikov *et al.*, in *Proceedings of the 7th International Woorkshop on Linear Coliders*, Zvenigorod, Russia (1997), Branch INP 97-07.
[9] É. I. Asinovskiĭ, L. M. Vasilyak, and V. V. Markovets, Teplofiz. Vys. Temp. **21**, 577 (1983).

Translated by Steve Torstveit

On the generation of radiation defects by accelerated ions in silicon

A. M. Ivanov and N. B. Strokan

A. F. Ioffe Physicotechnical Institute, Russian Academy of Sciences, St. Petersburg
(Submitted February 6, 1998)
Pis'ma Zh. Tekh. Fiz. **24**, 12–19 (October 26, 1998)

The introduction of centers of generation of charge carriers in pure Si is examined in the framework of the interaction of nonequilibrium defects and charge carriers directly in the track of an ion. An experiment on α particles with energies of 1.0–5.0 MeV is supplemented by the results of a numerical simulation of the stopping of such particles in Si. It is shown that the primary defects arising at the end of the track form a smaller number of generation centers. This is explained by the trapping of components of Frenkel pairs of charge carriers, the concentration of which in the track undergoes a 3-fold increase by the end of the range. Charge exchange between vacancies and interstitial atoms both accelerates recombination and lowers the number of primary defects participating in the subsequent complex-formation. © *1998 American Institute of Physics.* [S1063-7850(98)02010-2]

Radiation damage is commonly defined in terms of the number of electrically active centers that arise (as a rule, they lie deep in the band gap). However, it is helpful to trace the process of defect formation by proceeding from the initial state upon the temporally ''instantaneous'' formation of the primary Frenkel pairs (vacancy–interstitial atom) directly in the track.

The transport of the observation time means that between the time of creation of the primary defects in the ion track and the formation of the resulting centers comes a completely determinate stage of dispersal of the track. We recall that in the stopping of an ion its energy is expended predominantly on ionization. As a result, a significant number of nonequilibrium charge carriers – electron–hole pairs — are produced along with the defects in a microscopically small volume of the track (of the order of tens of μm^3 in the form of a cylinder of small radius).

1. Relaxation to equilibrium occurs primarily through the effective radial spreading of carriers by virtue of the high mobility and large concentration gradients between the track and the bulk of the crystal. The spreading is accompanied by recombination at existing centers in the material, and this leads to a loss in the number of carriers λ created by an ion. It has been shown[1,2] that as the mass of the ion increases, recombination of charge carriers directly at nonequilibrium defects takes on a governing role. An experiment was set up using the p^+–n structures of ion detectors with a variable value of the electric field F. It was observed that the hyperbolic dependence $\lambda \approx 1/F$ characteristic for light ions (see, e.g., Ref. 3) gave way to a logarithmic dependence $\lambda \approx \ln(1/F)$. It is just such a function that is obtained mathematically in the model of carrier recombination on defects arising in the track. Thus there is a quantitative description of the loss of carriers in the stage of spreading of the track. The situation in regard to the vacancy–interstitial (V–I) pairs is much less clear.

Obviously the (V–I) pairs, like the electrons and holes, will recombine and diffuse from the track into the bulk. In the bulk of the crystal both V and I participate in quasichemical reactions. These processes characterize the second stage of the recombination, when the formation of radiation centers is completed.

The quantitative aspects of defect formation are largely governed by the degree of importance of the cross interaction of nonequilibrium carriers and defects during the stage when the track still exists and their concentrations are high. This is due to the strong dependence of the interaction cross section of V and I on the charge state. It is known from calculations[4] that the critical distance between components for the occurrence of pair recombination in the neutral state $\langle I^0 - V^0 \rangle$ has the value $r_{cr} = 2a$, where a is the lattice constant. In the presence of partial charge exchange, when the charges of the pair are $\langle I^0 - V^- \rangle$, the critical distance is $r_{cr} = 4a$. Finally, for the case $\langle I^+ - V^- \rangle$ one has $r_{cr} = 7a$. This increase in r_{cr} is due to the Coulomb attraction of the components.

The loss in number of Frenkel pairs (FPs) can be expressed quantitatively (by analogy with the loss of carriers) by the ratio $\gamma = M/N_0 \leqslant 2$, where M is the number of centers formed. The ratio of M to the number N_0 of primary pairs arising is obviously an integral characteristic of the recombination of FPs in the track. In this approach the generation of FPs (which is uniquely related to the nature of the ion and of the crystal lattice) is treated separately from the subsequent quasichemical reactions. Indeed, the formation of complexes and their manifestation as centers M are predetermined by the impurity composition and structural defects of the material. In the final analysis, γ enters as a parameter which characterizes the ''yield'' of the FP components from the track in a given material in the stopping of ions of a specific type.

Unfortunately, it is difficult in practice to determine γ. The number N_0 of primary pairs can be found by a simulation of the stopping of an ion with the use of the TRIM code.[5] On the other hand, it is not possible to measure M, the number of centers (both shallow and deep), to sufficient ac-

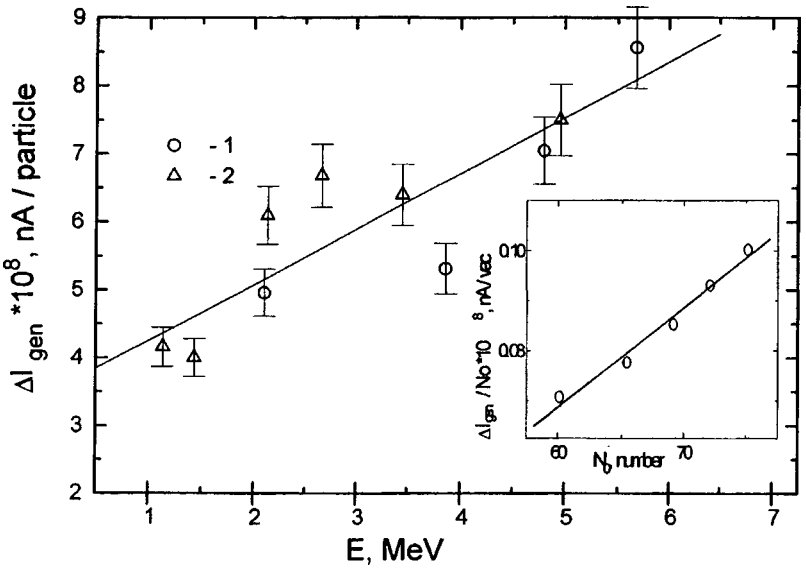

FIG. 1. Dependence of the increment of the generation current (normalized per α particle) as a function of the particle energy: *1* and *2* are the number of p^+-n structures based on pure Si. The inset shows the current increment of Fig. 1 in a normalization per vacancy as a function of the number of vacancies. The TRIM code was used to calculate N_0 at an energy of displacement of the Si atom of 40 eV.

curacy. The way out of this situation is to obtain comparative data for different ions.

In Ref. 6 the recombination of FPs in ion tracks was compared for two ions near opposite ends of the mass scale: ^{238}Pu α particles, and ^{252}Cf fission fragments, with mean energies of 5.48 and 80 MeV. The high efficiency of creating centers of generation in Si in the case of the fission fragments was explained by the configuration of the track, with the FPs and charge carriers distributed on opposite ends. Under such conditions the charge exchange of the FPs is hindered in comparison with the case of α particles, in the tracks of which the maxima of the distributions of the the charge carriers and the primary FPs coincide.

2. In this study the governing role of the track geometry in the efficiency of formation of radiation centers was checked for the case of ions of the same mass (α particles) but different energies.

The energy of the α particles was varied over the interval $E_\alpha = 1.0-5.7$ MeV. The α particles irradiated p^+-n detectors fabricated by planar technology on ''pure'' silicon (with a resistivity of several k$\Omega\cdot$cm). The irradiation was carried out at room temperature in a geometry close to orthogonal. The periphery of the sample was covered by a diaphragm. The dose and energy of the particles were determined directly by the detector through the counting rate and signal amplitude. As in Ref. 6, the number of centers introduced was determined from the increment of the generation current. The use of this parameter is justified by the fact that the system of deep levels introduced is identical, as was established from the spectra of the DLTS signal.

The observed curves of the dependence of the current increment (ΔI_{gen}) on the dose were linear. This permits one to find the normalized quantity ΔI_{gen} (nA) per particle for a series of α-particle energies (Fig. 1). The main error in the measurements was estimated as 7% and is due to the lack of temperature stabilization. For the subsequent analysis we used a linear approximation of the observed trend $\Delta I_{\text{gen}} = f(E_\alpha)$ (the continuous line in Fig. 1). This gives a slope of 0.82×10^{-8} nA/MeV on a per-particle basis.

3. The results of the numerical simulation of the stopping of α particles yield a distribution over the ion track of the energy E_{rec} transferred to recoil atoms and the energy E_{ion} dissipated on ionization. Figure 2 shows the result of a calculation using the TRIM code for $E_\alpha = 8.0$ MeV. The energy was chosen higher than the upper boundary of the experiment (5.7 MeV) in order to expand the range of the numerical simulation. The results were averaged over 650 particles. As we have said, the profiles of E_{rec} and E_{ion} have the form characteristic for light ions, with both the main part of the energy imparted to the lattice and the greatest ionization concentrated at the end of the range. One gets the impression that the overwhelming majority of E_{rec} comes in at coordinates near the maximum at 48.4 μm. Actually this is valid only for low energies.

The function $E_{\text{rec}} = f(E_\alpha)$ is obtained by integrating the distribution of dE_{rec}/dx (Fig. 2) from the value $48.4-R$ to 55 μm. Here R is the range of a particle of the given energy. It turned out that E_{rec} as a function of E_α increases linearly, the difference at the ends of the 1–8 MeV interval used reaching a factor of 1.5. As a result, with increasing E_α one should observe a noticeable increase in the number of primary defects. The inset in Fig. 2 shows E_{rec} versus the number N_0 of vacancies that arise at an energy of displacement of the Si atom taken as 40 eV (Ref. 7). The plot shows that the relation is linear, and the energy expended on the formation of FPs has an average value of 133 eV.

These results can be used to correct the experimental data by performing a normalization to the number N_0 of primary vacancies. A linear approximation of the dependence $\Delta I_{\text{gen}} = f(E_\alpha)$ was taken as the initial approximation (Fig. 1). However, the normalization did not lead to a constant ΔI_{gen}, i.e., the depend on N_0 was not eliminated. As before, one observes a linear rise at a rate of 2×10^{-11} nA per vacancy (inset in Fig. 1). The latter suggests that the primary FPs are not equivalent in respect to the formation of centers of generation. The experimental data definitely indicate that the efficiency of FPs is large in the case of high-

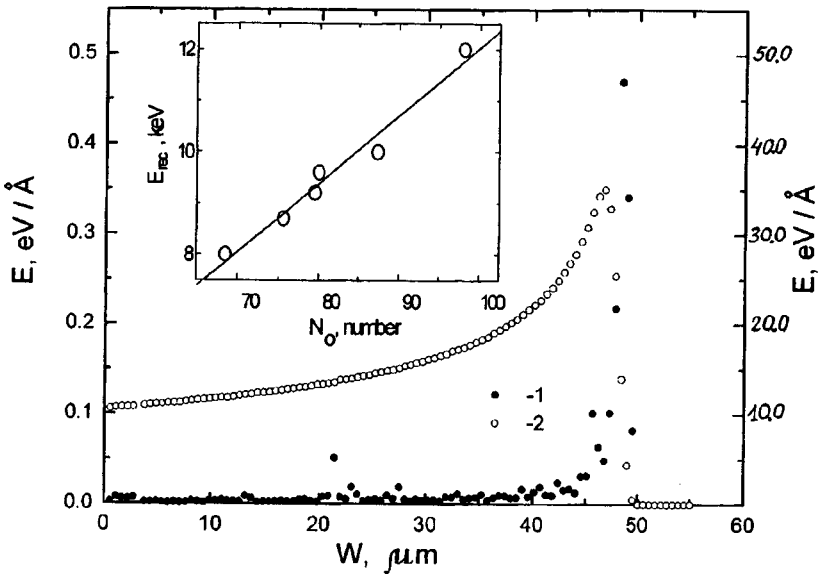

FIG. 2. Depth distribution of the energy loss expended on the displacement of atoms, E_{rec} (*1*, left-hand axis) and on ionization, E_{ion} (*2*, right-hand axis) in the stopping of α particles in Si. The inset shows the relation of the energy transferred to the atoms and the number of vacancies formed, according to a TRIM code calculation.

energy α particles; this can be explained qualitatively as follows.

Let us start with the case $E_\alpha = 1.0$ MeV, for which the range, $R = 3.4$ μm, fits inside the region of intense transfer for both E_{rec} and E_{ion}. For high energies, from the standpoint of stopping in Si, the difference is that FPs arise in the part of the track where the ionization has fallen by a factor of 3 from its maximum value (Fig. 2). In addition, this region comes at the beginning of the track, where the particle can transfer a significant portion of its energy to the δ electrons in an ionization event. This also lowers the density of nonequilibrium carriers. The net result is that charge exchange with the components of a FP and the possible subsequent recombination are slowed, and the FP is increasingly likely to pass out of the track into the bulk, where it forms generation centers.

A numerical estimate based on a comparison of the energies 1.0 and 5.0 MeV showed that the number of FPs increased by a factor of 1.27 and the current increments by a factor of 1.77. Thus the components of a FP created along the path of a stopping particle between 5.0 and 1.0 MeV are 2.85 times more active in forming centers than are the same components arising in the final stage of transferring the last 1.0 MeV of energy.

4. Let us conclude by returning to the observed values of the generation current. As we know, the value of I_{gen} per unit area S is proportional to the density m of deep centers and the width W of the electric-field region of the $p-n$ junction. In the simplest case, when the level of the centers is at the midpoint of the band gap and the cross sections for trapping of electrons and holes are equal, $\sigma_{n,p} = \sigma$, one has

$$I_{\text{gen}} = en_i WS/2\tau_{\text{gen}} = en_i v_{\text{th}} \sigma m V. \tag{1}$$

Here e is the charge of an electron, n_i is the intrinsic density, v_{th} is the thermal velocity, V is the volume supplying the carriers, and $\tau_{\text{gen}} = (v_{\text{th}}\sigma m)^{-1}$ is the carrier lifetime. We see that I_{gen} is determined by the total number of centers in the selected volume ($M = mV$) and does not depend on the specifics of the distribution. Therefore, in an experiment done at a fixed bias voltage on the structure of a layer $W > R$, one should observe a linear dependence $I_{\text{gen}}(M)$.

We recall that monitoring the onset of centers M from the ''recombination'' lifetime τ_R presents methodological difficulties. For example, in Ref. 9 a nonuniformity of τ_R that is specific for ions was noted. Specifically, in the transport of carriers the defects at the end of the range act as an internal boundary with a high rate of recombination. The method of determining M from the rate of generation has a wider domain of applicability. It is necessary only that the conditions conform to the model of an isolated center in an electric field.

To compare the number of centers and the measured currents we take as the initial value $dI_{\text{gen}}/dN_0 = 7\times10^{-19}$ A per vacancy (see the inset in Fig. 1). This corresponds to $E_\alpha = 1$ MeV, when the density of the charge carriers surrounding the primary FPs is the highest. The measured and expected values of dI_{gen}/dM are related through the parameter $\gamma = M/N_0 \leqslant 2$ as

$$dI_{\text{gen}}/dN_0 = \gamma(dI_{\text{gen}}/dM) = \gamma e n_i v_{\text{th}} \sigma_n \sigma_p \{\sigma_n \exp[\varepsilon] + \sigma_p \exp[-\varepsilon]\}^{-1}, \tag{2}$$

Here we have used the general form of Eq. (1) (see, e.g., Ref. 8), where $\varepsilon = (E - E_i)/kT$, E and E_i are the position of the level of center M and the midpoint of the band gap, k is Boltzmann's constant, and T is the absolute temperature. Let us compare the values of γ obtained from Eq. (2) for the three main generation levels: $E_c - 0.40$, $E_c - 0.44$, and $E_v + 0.33$ eV. These belong, respectively, to a divacancy, a vacancy–phosphor complex, and an interstitial carbon atom C_i and have the following cross sections: $\sigma_p = 4\times10^{-16}$, $\sigma_p = 2.7\times10^{-13}$, and $\sigma_n = 4.5\times10^{-16}$ cm^{-2}. The center C_i arises by a kick-out mechanism in the interaction of interstitial silicon with carbon atoms C_S located in lattice sites.

For the values of γ we obtain, in the respective order: $\gamma=15.6$, 0.005, and 0.22. Since by definition $\gamma\leqslant 2$, the center at $E_c-0.40$ eV does not participate in the generation. As to the center at $E_c-0.44$ eV, the number of these must saturate because of the small phosphorus content. We recall that in the experiment a linear dependence of ΔI_{gen} on the dose is observed, i.e., a single system of centers is manifested. We conclude that the generation of carriers is due to the center at $E_v+0.33$ eV, a finding in agreement with the results of Ref. 10. At the doses we used, $\approx 10^9$ cm^{-2}, a carbon content of 3×10^{16} cm^{-3} in the initial Si is sufficient to provide an ''unlimited source'' of C_S atoms. The value $\gamma=0.22$ obtained here is considerably higher than the expected[6] value, which is of the order of several percent.

5. In this letter the authors wished to call attention to the importance of the initial stage of dispersal of the ion track in the defect formation process. That stage depends on the nature of the ion (configuration of the track) and provides a sort of ''coefficient of injection'' of primary defects into the bulk of the crystal. As a consequence, the primary defects arising at different parts of the track have different efficiencies in respect to the formation of the resulting centers.

On the methodological front we have compared the possibilities for monitoring the introduction of defects from the observation of recombination and from the generation of charge carriers. We have shown that measurements of the increment of the generation current of a p^+-n structure as a function of the dose permit one to trace the introduction of interstitial carbon. Here one is actually monitoring the interstitial Si atoms that generate the carbon. We have determined the fraction comprised of the latter in the total number of primary Frenkel pairs in the track of an ion.

The authors express their gratitude to the seminar of the Laboratory of Nonequilibrium Processes in Semiconductors and to E. M. Verbitskaya for a helpful discussion.

[1] V. K. Eremin, I. N. Il'yashenko, N. B. Strokan, and B. Schmidt, Fiz. Tekh. Poluprovodn. **29**, 79 (1995) [Semiconductors **29**, 42 (1995)].
[2] B. Schmidt, V. Eremin, I. Ilyashenko, and N. Strokan, Nucl. Instrum. Methods Phys. Res. A **377**, 184 (1996).
[3] E. Verbitskaya, V. Eremin, N. Strokan, J. Kemmer, B. Schmidt, and J. Von Borany, Nucl. Instrum. Methods Phys. Res. B **84**, 51 (1994).
[4] V. V. Emtsev, T. V. Mashovets, and V. V. Mikhnovich, Fiz. Tekh. Poluprovodn. **26**, 20 (1992) [Sov. Phys. Semicond. **26**, 12 (1992)].
[5] J. F. Ziegler (Ed.), *Ion Implantation: Science and Technology*, Academic Press, Orlando (1984).
[6] A. M. Ivanov, I. N. Il'yashenko, N. B. Strokan, and B. Schmidt, Fiz. Tekh. Poluprovodn. **29**, 543 (1995) [Semiconductors **29**, 281 (1995)].
[7] L. S. Berman, N. A. Vitovskiĭ, V. N. Lomasov, and V. N. Tkachenko, Fiz. Tekh. Poluprovodn. **24**, 1816 (1992) [Sov. Phys. Semicond. **24**, 1131 (1992)].
[8] S. M. Sze, *Physics of Semiconductor Devices*, 2nd ed. Wiley, New York (1981); Mir, Moscow (1984), Vol. 1, p. 456.
[9] A. M. Ivanov, N. B. Strokan, and V. B. Shuman, Pis'ma Zh. Tekh. Fiz. **23**, 79 (1997) [Tech. Phys. Lett. **23**, 369 (1997)].
[10] A. M. Ivanov and N. B. Strokan, Fiz. Tekh. Poluprovodn. **31**, 674 (1997) [Semiconductors **31**, 575 (1997)].

Translated by Steve Torstveit

Features of the emission spectrum of relativistic electrons moving in an ultraintense laser field

A. Kh. Khokonov, M. Kh. Khokonov, and R. M. Keshev

Kabardino-Balkarian State University, Nal'chik
(Submitted October 17, 1997; resubmitted May 5, 1998)
Pis'ma Zh. Tekh. Fiz. **24**, 20–27 (October 26, 1998)

Important differences are found between the spectral characteristics of the radiation emitted by relativistic electrons moving the field of a terawatt laser and the case of their passage through a static transverse field. The role of nonlinear effects of higher-harmonic generation and of the quantum effects of recoil and spin in the emission of a hard photon is analyzed in the framework of the quasiclassical Baĭer–Katkov method. © *1998 American Institute of Physics.* [S1063-7850(98)02110-7]

1. The main features of the interaction of relativistic electrons with an electromagnetic plane wave were investigated in the mid-1960s (see the review[1] and the references cited therein). In recent years this topic has attracted renewed interest[2–5] in connection with the advent of high-power terawatt lasers ($1\ \mathrm{TW}=10^{12}$ W), for which the value of the Lorentz-invariant field parameter

$$\nu_0^2=\frac{e^2\mathcal{E}_0^2}{2m^2\omega_0^2c^2} \tag{1}$$

may be greater than unity. Here $\mathcal{E}_0$ is the amplitude of the electric field of the laser wave, which has frequency ω_0, e and m are the charge and mass of the electron, and c is the speed of light. We will refer to laser beams with $\nu_0>1$ as ultraintense. In particular, the first four harmonics in the interaction of electrons with energy 46.6 GeV with a circularly polarized laser beam, with a field parameter $\nu_0=0.6$ at the focus, were recently observed.[2]

In this paper we consider the emission of relativistic electrons in a terawatt laser radiation field on the basis of the quasiclassical method of Baĭer and Katkov.[6] This approach has certain advantages over that taken in recent papers by other authors (see, e.g., Ref. 5): it permits a relatively simple incorporation of the quantum effects of recoil in the emission of a hard photon, the influence of spin on the emission, and of nonlinear effects due to the onset of higher harmonics in the emission spectra.

2. In comparing the radiation emitted by electrons moving in the field of a plane wave with the case of motion in a static transverse field, an important circumstance is that the invariant known as the nondipolarity parameter $\beta_\perp\gamma$ is the same as the field parameter (1) (here $\beta_\perp$ is the velocity component transverse to the direction of the average velocity of the electron).[7] For example, for an electron moving counter to a linearly polarized plane wave one has the relation $\overline{\beta_\perp^2\gamma^2}=\nu_0^2$, where the overbar denotes averaging over the period of the transverse motion of the electron. This relation is indicative of the substantial difference between the radiation in the field of a plane wave and in static transverse fields. As a typical example of the emission in static transverse fields we shall consider the radiation emitted during channeling.[8]

In a plane wave, where the radiation is the result of the scattering of real photons on electrons, the nondipolarity parameter is independent of the electron energy, i.e., for $\nu_0 \ll 1$ the dipole approximation is applicable even when the energies of the emitted photons is of the order of the energy of the electrons, and since the transverse motion in the field of a plane wave is essentially harmonic, only a single harmonic is radiated, with a sharp dipole maximum in the spectrum. For motion in a static transverse field, on the other hand, where the radiation is the result of the scattering of virtual photons on electrons, such a situation is not realized in practice, since the nondipolarity parameter $\beta_\perp\gamma$ increases with increasing energy (for channeling radiation, e.g., $\beta_\perp\gamma \sim \gamma^{1/2}$), and when the angle of deflection of the electron by the external field exceeds the characteristic emission angle (i.e., when $\beta_\perp\gamma\gg1$), the radiation of higher harmonics becomes important, and the spectrum is given by formulas of the synchrotron type.[6,9]

At the electron energies attainable in today's accelerators ($E\sim300$ GeV) the contribution of the spin to the channeling radiation is unimportant although not negligible.[10] The reason is that the emission spectrum is dominated by relatively soft photons, and the number of photons with $\hbar\omega \sim E$ is comparatively small. For motion in the field of a plane wave, however, the energy of the emitted photons increases with increasing E more rapidly than during channeling, and if the field parameter (1) is not too much greater than unity, we shall see that the spin contribution to the hard part of the spectrum is the dominant one. A similar comparison of the channeling radiation with the radiation emitted during motion in the field of a plane wave for the case when the emission spectrum is dipolar and lies in the x-ray region has recently been presented in Ref. 7.

3. Besides the field parameter (1), we shall be interested in two other Lorentz invariants: $a=2\hbar k_0^\mu p_\mu/(m^2c^2)$ and $\chi=e\hbar|F_{\mu\nu}p^\eta|/(m^3c^4)$, where k_0^μ is the wave 4-vector of the incident plane wave, p^μ is the 4-momentum of the electron,

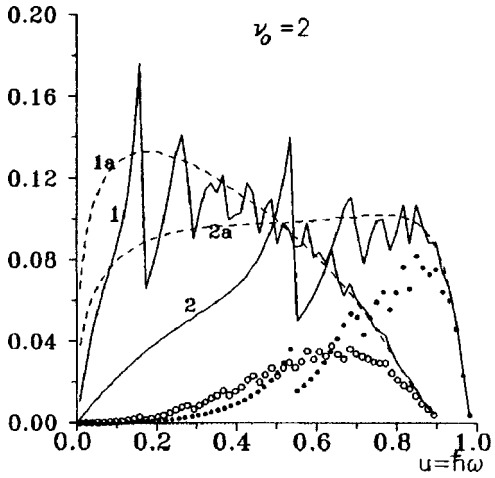

FIG. 1. Emission spectra of electrons moving counter to a linearly polarized plane wave with $\nu_0=2$. The solid curves *1* and *2* correspond to the values $a=1$ and $a=6$, respectively. The dashed curves *1*a and *2*a correspond to the synchrotron approximation for these same values of a. The points show the spin contribution: ○ for $a=1$, and ● for $a=6$.

and $F^{\mu\nu}$ is the electromagnetic field tensor. For $\gamma \gg 1$ we have to an accuracy of $\beta_\perp^4$:

$$a \approx 2\hbar\Omega_0\gamma^2/E, \quad \chi \approx e\mathcal{E}\hbar c(1+\beta)/(m^2c^2\gamma), \tag{2}$$

where $\mathcal{E}=\mathcal{E}_0\cos\omega_0(t+z/c)$ is the magnitude of the electric field in the plane wave. The quantity $\Omega_0=\omega_0(1+\beta)$ has the meaning of the frequency of the transverse oscillations of an electron in the field of a plane wave. In Eq. (2) the quantity α is independent of time, and the time dependence of the invariant χ enters only through $\mathcal{E}=\mathcal{E}(t)$. The parameter χ is well known in the theory of electromagnetic processes in static external fields.[1,6]

4. The results for electrons moving counter to a linearly polarized laser beam with a wavelength of 1 μm are presented in Figs. 1 and 2. In this case the Baĭer–Katkov method leads to an exact analytical expression analogous in form to the case of planar channeling of positrons (see Ref. 8, Sec. 3.3). The corresponding expressions are awkward but straightforward and will not be given here (see also Appendix A in Ref. 1). The shape of the emission spectrum in the field of a plane wave is determined in the general case by two parameters, a and ν_0, but the situation simplifies substantially in the two limiting cases $\nu_0 \ll 1$ (weak external field) and $\nu_0 > 1$ (strong field).

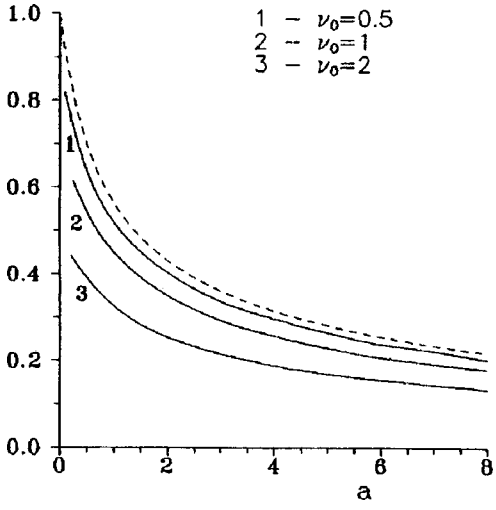

FIG. 2. Total number of photons emitted per unit length in units of N_0 (Eq. (4)) as a function of the parameter a (Eq. (2)). The dashed curve is the dipole approximation: $\nu_0 \ll 1$. Curves *1*, *2*, and *3* are for the values $\nu_0=0.5$, 1, and 2, respectively.

5. The case $\nu_0 \ll 1$ corresponds to the dipole approximation. In this case the spectrum is determined by just one invariant, a. The quantum dipole formulas are well known in the theory of the interaction of a plane wave with moving electrons (see Ref. 11, Sec. 101). Unlike the case of static transverse fields, for motion in the field of a plane wave the dipole approximation is valid for arbitrarily high electron energies, provided only that $\nu_0 \ll 1$. In channeling, for example, the situation in which quantum effects would play a role and the emission spectrum would be described by the dipole formulas is never realized in practice, and therefore at high enough energies, when the role of quantum recoil and spin becomes important (this is for energies $E>50$–100 GeV), the dipole radiation condition is inevitably violated. In this sense the method of obtaining hard polarized photons with $\hbar\omega \sim E$ by means of lasers with $\nu_0 \sim 0.2$–0.5 has advantages over channeling radiation in that the emission spectrum has a higher degree of monochromaticity and there is no multiphoton background in the soft part of the spectrum. Such a background, which is due to the high multiplicity of the emission, is unavoidable in the channeling of electrons and positrons with energies $E \geqslant 50$–100 GeV.[12] At lower or higher values of ν_0 these advantages of emission in the field of a plane wave are lost. For example, at $\nu_0 \ll 1$ the total probability of emission in the field of a plane wave is comparatively small. For $\nu_0 > 1$ nonlinear effects play a greater role in the Compton scattering, and the spectrum broadens. In addition, in ultraintense laser fields the multiplicity of the emission becomes more important,[2] and such destructive factors as the ejection of the electron from the laser beam on account of the nonuniformity of the spatial distribution of the intensity over the transverse cross section of the beam play an increasing role.[13,14]

6. The form of the emission spectrum in the field of a plane wave is also simplified in the limit $\nu_0 > 1$, when the higher harmonics become governing. In this case the spectrum is also determined by a single parameter (now χ) and is given by the well-known quantum synchrotron formula[15] averaged over the period of the transverse motion $T=2\pi/\Omega_0$, the parameter χ being related to the invariants a and ν_0 as $\chi = a\nu_0\sin(\Omega_0 t)/\sqrt{2}$. It can be shown that this synchrotron approximation is valid under the condition

$$\nu_0^2 u a^{-1}(1-u)^{-1} > 1, \tag{3}$$

where $u=\hbar\omega/E$ is the dimensionless frequency of the emitted photon.

The synchrotron approximation has been applied successfully for calculating the channeling radiation spectra for electrons with energies above 100 GeV,[6,9,12] and the higher the electron energy, the higher the degree of accuracy of the synchrotron approximation. In the case of a plane wave,

however, at a fixed value of the field parameter ν_0 the condition of applicability of the synchrotron approximation is violated as the electron energy increases, as follows from Eq. (3).

7. Figure 1 shows the energy spectra of the radiation emitted by electrons moving counter to a linearly polarized laser beam with $\nu_0=2$. The values $a=1$ (curve *1*) and $a=6$ (curve *2*) correspond to electron energies of ~ 50 and 300 GeV. The scale on the ordinate is uN_u/N_0, where N_u is the number of photons with the specified frequencies emitted per unit length, and N_0 is the total number of photons emitted per unit length in a weak laser field, when $\nu_0 \ll 1$:

$$N_0=(2/3)\alpha\nu_0^2\Omega_0/e, \tag{4}$$

where $\alpha=1/137$.

Calculations in the synchrotron approximation are shown by the dashed curves *1a* (for $a=1$) and *2a* (for $a=6$) in Fig. 1. It is seen that the synchrotron approximation gives a good description of the hard part of the spectrum if condition (3) is satisfied. The points show the contribution of the spin term to the spectrum.

Increasing the electron energy at a fixed ν_0 degrades the accuracy of the synchrotron approximation, in accordance with what we have said above (cf. curves *1* and *2* in Fig. 1). On the other hand, as the energy increases, so does the role of the spin in the hard part of the spectrum. For example, at the values $\nu_0=2$ and $a=6$ the spin term has come to dominance in the hard part of the spectrum. We note for comparison that at the same values of the electron energy the role of the spin term in oriented crystals is significantly smaller, and the complex structure of the spectrum due to the contribution of individual harmonics does not appear at all.[10,12]

8. Figure 2 shows how the total number N of photons emitted per unit length depends on the parameter a for various values of ν_0, as calculated according to the exact formulas (solid curves) and in the dipole approximation (dashed curve). The ratio N/N_0 is plotted on the ordinate.

In practice one is interested in the number of hard photons emitted per electron at energies $0.8u_m<u<u_m$, where $u_m\sim a/(1+a)$ is the maximum energy of an emitted photon (for estimation we just use the dipole approximation). The number of such photons $N_1\sim 0.1\times N_0$ for $a>3$, where N_0 is given by formula (4). For a laser with a power of 1 TW and wavelength 1 μm, interacting with 150-GeV electrons, we obtain $N_1\approx 1.1\times 10^{-4}$ photons over a length $L=0.5$ mm at a transverse area of the laser beam $\Sigma=1\ \mathrm{mm}^2$ (here $u_m=0.75E$ and $\nu_0^2\approx 3.7\times 10^{-5}$). This number increases significantly as the transverse cross section of the beam decreases. For example, at $\Sigma=100\ \mu\mathrm{m}^2$ ($\nu_0^2\approx 0.37$) at the same length, one already has $N_1\sim 1$. This latter value is comparable to that which can be attained in oriented crystals at the same electron energy. This is not unexpected, since the energy density of the field at the focus of a terawatt laser can be comparable to the electrostatic energy density in the field of a continuous crystalline potential.[7]

The emission spectrum of relativistic electrons in the field of a plane wave has a pronounced oscillatory character. This is due to the interference of the waves emitted at different parts of the strictly periodic transverse trajectory (see the solid curves in Fig. 1). The synchrotron approximation takes into account the emission contribution of only the small part of the trajectory which can be approximated by a circular arc. Such a spectrum does not describe oscillations. As the intensity of the laser field is increased at a fixed electron energy, the role of the higher harmonics in the spectrum increases, and in the limit of large ν_0 (at the energies under consideration, this is for $\nu_0>3-4$) the spectrum ever more closely approaches the synchrotron spectrum.

9. In summary, we have shown that the character of the radiation emitted by relativistic electrons moving in the field of an intense laser wave differs substantially from the case of electron motion in a static transverse field. This is particularly true of the spectral characteristics of the radiation as functions of the electron energy and in regard to the role of spin in the emission. From the standpoint of obtaining hard gamma rays it is in practice most preferable to use lasers with $\nu_0\sim 0.2-0.5$. In turn, the use of oriented crystals is preferable for problems in which a large total number of photons is required without regard for the degree of monochromaticity of the spectrum, e.g., for the purpose of obtaining intense positron beams.[16]

The authors thank R. A. Carrigan of Fermilab for stimulating their interest in this problem and gratefully acknowledge helpful discussions with J. W. Anderson and especially with J. Lindhard of the Institute of Physics in Aarhus, Denmark.

[1] V. I. Ritus, Tr. Fiz. Inst. Akad. Nauk SSSR (FIAN) **111**, 5 (1979).
[2] C. Bula, K. T. McDonald, E. J. Prebys *et al.*, Phys. Rev. Lett. **76**, 3116 (1996).
[3] P. Eisenberger and S. Suckewer, Science **274**, 201 (1996).
[4] R. W. Schoenlein, W. P. Leemans, A. H. Chin *et al.*, Science **274**, 236 (1996).
[5] Y. I. Salamin and F. H. M. Faisal, Phys. Rev. A **54**, 4383 (1996).
[6] V. N. Baĭer, V. M. Katkov, and V. M. Strakhovenko, *Electromagnetic Processes at High Energy in Oriented Single Crystals* [in Russian], Nauka, Novosibirsk (1989).
[7] R. A. Carrigan and M. Kh. Khokonov, Fermilab Preprint Pub-97/115 (1997).
[8] V. V. Beloshitsky and F. F. Komarov, Phys. Rep. **93**, 117 (1982).
[9] J. C. Kimball and N. Cue, Phys. Rev. Lett. **52**, 1747 (1984).
[10] A. H. Sorensen, Nucl. Instrum. Methods Phys. Res. B **119**, 1 (1996).
[11] V. B. Berestetskiĭ, E. M. Lifshits, and L. P. Pitaevskiĭ, *Quantum Electrodynamics*, 2nd ed., Pergamon Press, Oxford (1982) [cited Russian original, Nauka, Moscow, 1989]. Nucl. Instr. Methods B **119**, 1 (1996).
[12] M. Kh. Khokonov, Zh. Éksp. Teor. Fiz. **103**, 1723 (1993) [JETP **76**, 849 (1993)].
[13] T. W. B. Kibble, Phys. Rev. **150**, 1060 (1966).
[14] J. Lindhard, Private communication.
[15] N. G. Klepikov, Zh. Éksp. Teor. Fiz. **26**, 19 (1954).
[16] X. Artru, V. N. Baier, T. V. Baier *et al.*, Nucl. Instrum. Methods Phys. Res. B **119**, 246 (1996).

Translated by Steve Torstveit

Study of the surface of diamondlike carbon films doped with copper

V. I. Ivanov-Omskiĭ, S. G. Yastrebov, O. A. Golubok, S. A. Masalov, and V. V. Rozanov

A. F. Ioffe Physicotechnical Institute, Russian Academy of Sciences, St. Petersburg
Institute of Analytical Instrumentation, Russian Academy of Sciences, St. Petersburg
(Submitted March 25, 1998)
Pis'ma Zh. Tekh. Fiz. **24**, 28–34 (October 26, 1998)

A study of the surface of copper-doped diamondlike carbon films by the methods of scanning tunneling microscopy and spectroscopy is reported. It is found that the introduction of copper modifes both the microstructure and the electronic properties of the films.
 [S1063-7850(98)02210-1]

Films of amorphous hydrogenated carbon (*a*-C:H), sometimes called diamondlike *a*-C:H, are of interest primarily because of their unique properties as a universal coating.[1] Recently, however, their emission properties have attracted attention, particularly those of doped films, for which the field emission is appreciable at comparatively low electric fields $E \sim 10^4$ V/cm.[2]

The goal of this study was to investigate the microtopography and local electron emission of *a*-C:H layers doped with cooper.

The *a*-C:H layers were formed on Si (111) substrates on which a chromium buffer sublayer 1.5 μm thick had been deposited by magnetron sputtering to provide reliable trapping of the tunneling current in subsequent studies of the surface with a scanning tunneling microscope (STM). After an outgassing of the substrates prepared in this manner, layers of *a*-C:H:Cu were deposited on them in a growth chamber at a temperature $T = 200°$C and a pressure of 10^{-6} Torr by the method of magnetron cosputtering of graphite and copper targets in an argon–hydrogen plasma (80%Ar, 20%H; $P = 10$ mTorr).[3] the power released in the magneton was ~400 W (the current through the magnetron was maintained at 1 A). The thickness of the film was determined by ellipsometry. The rate of film growth was 220–300 nm/h, and the deposition time was 30 min.

The surface topology and local electronic properties of the grown films were investigated on a scanning tunneling microscope (STM) with an Ir probe in the topographic mode and in the mode of measurement the local current–voltage characteristics $I(V)$. The topography was studied in the constant-tunneling-current mode. On different parts of the samples we obtained reproducible STM images and made local measurements of $I(V)$.

The measurements were made at atmospheric pressure on two series of samples: undoped and copper-doped. The copper concentration in the films of the second series was determined by secondary-ion mass spectroscopy and was found to be 9 at.%.

Figure 1a shows typical STM images of the surface of an undoped samples, taken at a bias of $V_T = -1$ V and a current $I_T = 0.05$ nA. Figure 1b gives the transverse cross section of the STM image along the line A–B in Fig. 1a. The STM image of the undoped sample and its transverse section demonstrate spatial uniformity of the surface of the film with a random variation of the relief along the z coordinate on a scale of ~10 nm, having the form of easily visible peaks. At the achievable resolution there was no pronounced structuring in the (x,y) plane.

Figure 1c shows a local $I(V)$ characteristic measured at one spatial point of the sample during a pause of the scanning with a voltage sweep from -2 to $+5$ V with the feedback loop open. Similar curves were obtained at different points on the sample surface.

The $I(V)$ characteristic (Fig. 1c) has a pronounced asymmetric (''diode'') character with a small tunneling current at positive bias on the sample and a sharply rising tunneling current at negative biases $V_T < -1$ V.

The asymmetric character of the $I(V)$ curve is indicative of *p*-type conductivity of the diamondlike film. The Fermi level lies near the top of the valence band and makes for a difference in the potential barriers for electrons tunneling from the sample to the Ir tip and from the Ir tip to the sample in the system ''Ir tip/air gap/diamondlike film/Cr chrome.''

Figure 2a,b shows a typical STM image of the surface of a doped sample and the transverse section corresponding to the line A–B. It is seen that the copper-doped sample exhibits a granular structure of the surface with a sharper drop in height along the z axis (~40 nm) as compared to the undoped sample. In the (x,y) plane one observes granules with several characteristic spatial dimensions ~1 nm (fine granules), ~40 nm (medium granules), and ~80 nm (large granules). The medium and large granules contain structures having the dimensions of the fine granules, suggesting a fractal mechanism of formation of the observed surface profile arising when finely disperse copper acts on the surface. The chemical composition and structure of the observed granules require further study.

Figure 2c shows the typical $I(V)$ characteristic of a copper-doped sample. One notices that in this case the $I(V)$ curve is more symmetric than those measured for the undoped samples, which indicates important differences in the electronic spectra of the doped and undoped samples. The symmetric nature of the $I(V)$ characteristic of the doped sample presumably argues in favor of an inversion of the

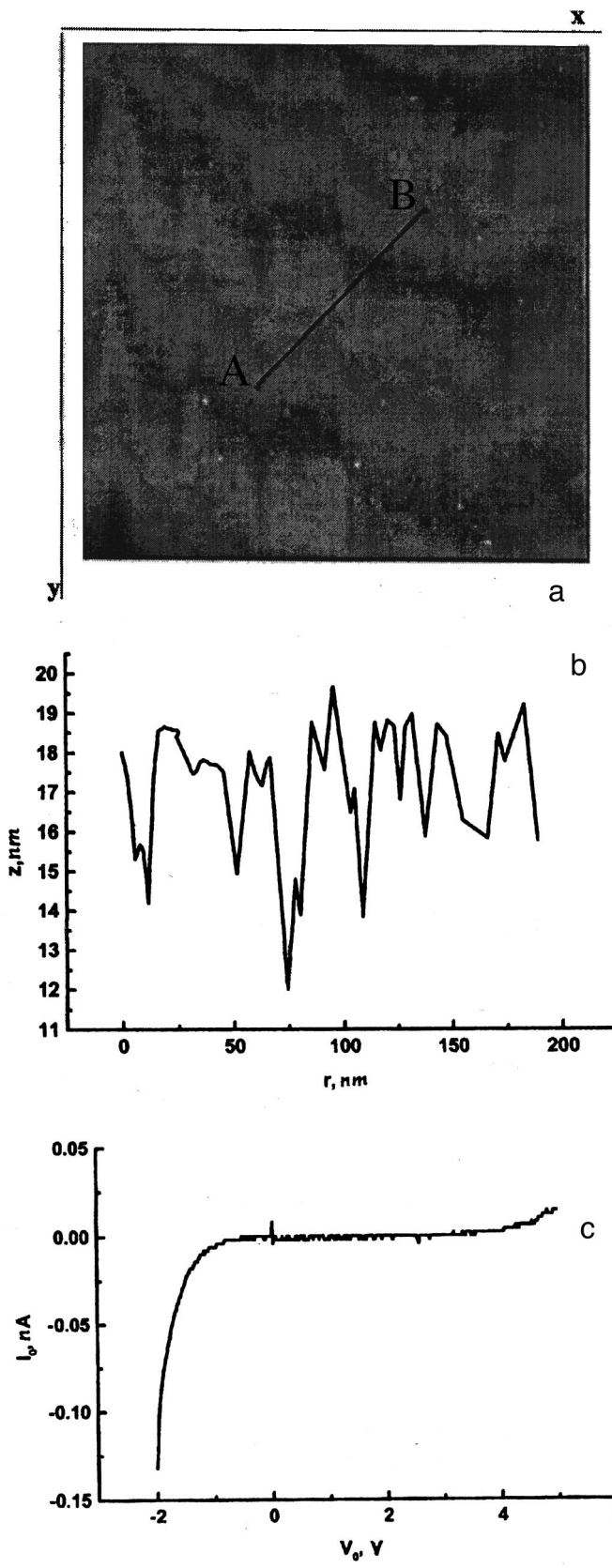

FIG. 1. Diagnostic results (topography, spatial section, current–voltage characteristic) of a typical surface of an undoped *a*-C:H film. a: Typical STM image taken near the ''undusted'' part of the substrate (dark spot on the image). The image was taken by an STM with $V_T = -1$ V and $I_T = 0.05$ nA, scanning area 0.4×0.4 μm; b: transverse section of the investigated film; c: local current–voltage characteristic.

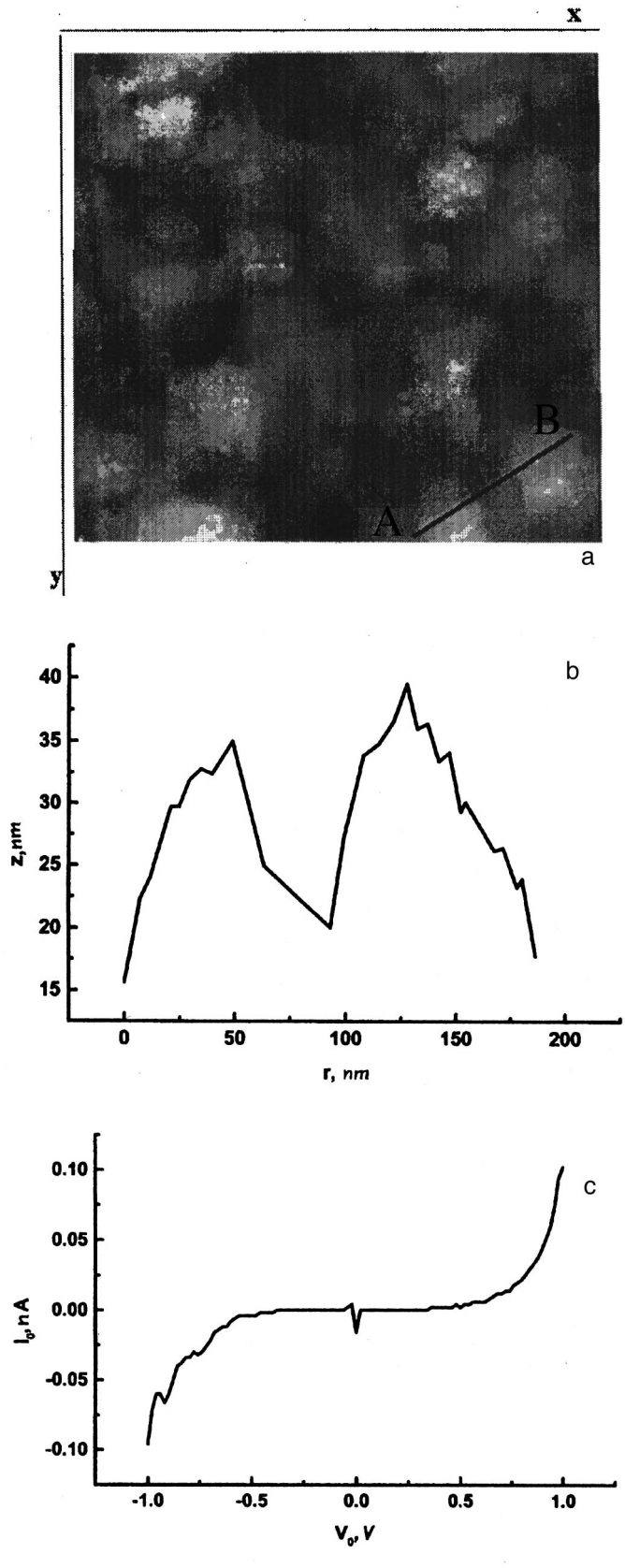

FIG. 2. Diagnostic results (topography, spatial section, current–voltage characteristic) of a typical surface of a copper-doped *a*-C:H film. a: Typical STM image of a copper-doped *a*-C:H film. The image was taken by an STM with $V_T = -1$ V and $I_T = 0.05$ nA, scanning area 0.4×0.4 μm; b: transverse section of the investigated film; c: local current–voltage characteristic. The feature at the center is the zero-bias anomaly.

type of conductivity under the influence of copper doping of the graphitic component of *a*-C:H.

In summary, doping of the material with copper substantially modifies both the structure of the surface of the film and its electronic properties.

This study was supported in part by Grants No. 97-02-18100-a and 97-03-32273-a from the Russian Fund for Fundamental Research, by a grant from the University of Arizona, and by grants No. 980024 (''Gel'') and 94007 (''Film'') from the program ''Fullerenes and Atomic Clusters'' of the Ministry of Science of the Russian Federation.

[1] J. C. Angus and C. C. Hayman, Science **241**, 913 (1998).
[2] A. J. Gehan Amaratunga and S. R. P. Silva, Appl. Phys. Lett. **68**, 2529 (1996).
[3] V. I. Ivanov-Omskii, A. V. Tolmatchev, and S. G. Yastrebov, Philos. Mag. B **73**, 715 (1996).

Translated by Steve Torstveit

Investigation of the characteristics of an ionization–neutron calorimeter in 4–70 GeV hadron beams at the IHEP accelerator

V. V. Ammosov, G. I. Merzon, T. Saito, K. Sasaki, V. A. Ryabov, A. P. Chubenko, and A. L. Shepetov

P. N. Lebedev Physics Institute, Russian Academy of Sciences, Moscow
Institute of High-Energy Physics, Russian Academy of Sciences, Moscow
Tokyo University, Japan
Kochi University, Japan
(Submitted August 15, 1997; resubmitted April 10, 1998)
Pis'ma Zh. Tekh. Fiz. **24**, 35–42 (October 26, 1998)

As a step in the development of an ionization–neutron calorimeter, a device which combines the properties of ionization and neutron calorimeters, measurements are made of the mean values and fluctuations of the neutron yield from a lead target 60 cm thick and 20×20 cm in area. The measurements were made at the U-70 accelerator in pion and proton beams with energies of 4 and 70 GeV, respectively. The mean values of the neutron yield are in good agreement with the data calculated using the SHIELD code. [S1063-7850(98)02310-6]

INTRODUCTION

The ionization calorimeter, which was first proposed over 30 years ago[1,2] for measuring the energy of cosmic rays, is now widely used in accelerator experiments as well.[3–5] The working principle of the ionization calorimeter is based on measurement of the ionization produced by cascades of ionizing particles formed by primary particles as a result of the interaction with the nuclei of atoms of the medium.

Another method of measuring energies, based on the detection of the evaporative neutrons from fissions of nuclei by cascade particles, was also proposed more than 30 years ago[6] and is used in the analysis of data from the world-wide network of neutron monitors.[7] However, total-absorption neutron calorimeters, notwithstanding proposals for their employment,[8] have not yet come into wide use.

It is advantageous to combine the two principles of measurement of the energy of a particle in a single device — an ionization–neutron calorimeter (INC). Such a calorimeter would be substantially more informative than separate ionization and neutron calorimeters.

The point is that in addition to determining the energies by two independent methods, an INC would be capable of distinguishing gamma rays, electrons, and hadrons in a mixed stream of particles, since the neutron yield in electromagnetic cascades is not more than 5–10% of the yield for a nuclear cascade.[9,10] If the method of moderation to thermal energies is used for neutron detection in the INC, the construction of the INC will be practically the same as for an ordinary ionization calorimeter. In that case the neutron signals will be delayed relative to the ionization signal by tens and hundreds of microseconds on account of the thermalization and diffusion processes in the moderator material, and the ionization and neutron signals can be registered by the same detectors (e.g., gas-filled proportional neutron counters) with a time shift.

The characteristics of the ionization signal in an ionization calorimeter are well known.[3–5] In this paper we investigate the main properties of the neutron signal: 1) the dependence of the average neutron yield ν on the primary hadron energy E_0; 2) fluctuations of the neutron yield at different energies E_0; 3) the thermalization and diffusion time of neutrons in the layered structure of the calorimeter; 4) the depth profile of the neutron signal in a combined absorber containing light and heavy materials.

EXPERIMENTAL APPARATUS

In the experiment we used an INC with an absorber containing 6 layers of lead 10 cm thick and 20×20 cm in area, with interlayers of polyethylene 6 cm thick. The neutron detectors were helium-filled (^{3}He) SNM-18 counters 30 cm long and 3 cm in diameter. Channels were drilled in the polyethylene interlayers to accomodate three counters under each layer of absorber of the INC, arranged in such a way that the distance between centers of two adjacent counters was 6 cm and between two counters in neighboring layers was 15 cm; the total number of counters in the INC was 18.

To improve the efficiency of detection of the evaporative neutrons generated in the INC, the lead absorber was covered on all sides with a polyethylene reflector–moderator having a thickness of $\cong 10$ cm. To determine the detection efficiency ε for evaporative neutrons we made calibration measurements with Po–Be sources with activities of 2.25×10^5 and 2.25×10^6 Bq. The sources were placed alternately at different points of the INC, and the total neutron count in the 18 channels of the INC was determined. The average detection efficiency obtained for 20 different positions of the source in the INC was $\langle\varepsilon\rangle = 7.4\pm 0.4\%$.

Working measurements were made with pion and proton beams from the U-70 accelerator at the Institute of High-Energy Physics (IHEP) in Moscow, with energies $E_{\pi^+} = 4$ GeV and $E_p = 70$ GeV. A ''drawn-out'' beam was used, with the hadron dump occurring uniformly over the course of

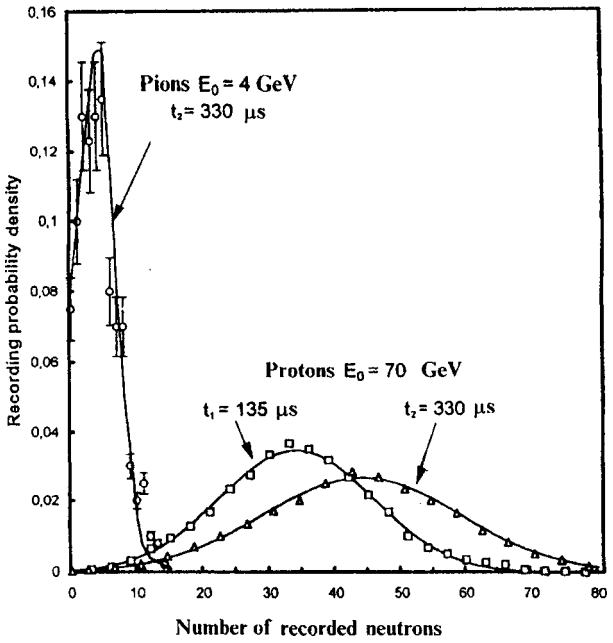

FIG. 1. Distribution of the number of recorded evaporative neutrons from cascades generated in a lead absorber ($20\times20\times60$ cm) by pions ($E_\pi = 4$ GeV) and protons ($E_p = 70$ GeV). The characteristic lifetime of the moderated neutrons in the ionization–neutron calorimeter was found to be $\tau \approx 135$ μs from a comparison of the results of measurements with the duration of the time gates $t_1 = 135$ μs and $t_2 = 330$ μs.

2 s and the total number of particles in each dump not exceeding 10 000, so that the average time between hadron passages was $\geqslant 200$ μs.

The triggering of the INC ensured the following: 1) discrimination of the neutron signal from a single beam particle passing through the center of the INC; 2) no overlap of the neutron signals from two or more particles, and 3) elimination of the signals of background particles.

The trigger signal was formed with the use of four scintillation counters: S_1, S_2, S_3, and S_4, on a base line of 20 m. Counter S_1 was placed directly in front of the exit window of the beam collimator, and S_3 directly in front of the calorimeter. Coincidences $S_2S_2S_3$ discriminated events corresponding to the passage of a beam particle through the apparatus. To separate out phonon events and passages of additional beam particles we used an anticoincidence counter S_4 of large size (30×30 cm) with a central aperture 2 cm in diameter.

Each trigger signal $S_1S_2S_3\overline{S_4}$ with a delay of 10 μs opened a time gate for lengths of time varying from 30 to 420 μs (in different series of experiments), within which the neutron signals were registered in the INC channels.

RESULTS OF THE MEASUREMENTS

Figure 1 shows the fluctuation curves for the number m of neutrons registered by the INC in cascades of protons with $E_p = 70$ GeV and pions with $E_{\pi^+} = 4$ GeV. For protons the distribution is well approximated by a Gaussian curve, while for pions it is a superposition of two Poisson distributions, a circumstance which reflects the complex character of the process of generation of nuclear fissions in the absorber.

TABLE I. Pb absorber, $20\times20\times60$ cm.

Particle	E_0, GeV	$\langle m\rangle$	$\sigma(m)$	$\langle \nu_{\rm exp}\rangle$	$\sigma_{\rm exp}(\nu)$	$\langle \nu_{\rm th}\rangle$
π meson	4	4.35 ± 0.22	2.2 ± 0.1	63 ± 3	9.5 ± 4	78
Proton	70	43.2 ± 0.08	14.3 ± 0.7	624 ± 12	171 ± 12	650

The characteristic lifetime of the neutrons in the INC was determined from the dependence of the average values $\langle m\rangle$ on the duration t of the time gates and had the value (130 ± 10) μs. All the values of $\langle m\rangle$ given below correspond to a gate duration $t = 330$ μs, in which case the neutron collection efficiency was around 95%.

Since each neutron is registered independently, the distribution $P(m)$ of the number m of neutrons registered is related to the distribution $P(\nu)$ of the number ν of neutrons generated in the absorber of the INC by the simple expression

$$P(m) = \sum_{\nu=m}^{\infty} P(\nu) C_\nu^m \varepsilon^m (1-\varepsilon)^{\nu-m}.$$

From this expression it is not difficult to obtain the relations between the average values and the variances of the number of observed and generated neutrons:

$$\langle \nu\rangle = \langle m\rangle/\varepsilon; \quad \sigma^2(\nu) = \sigma^2(m) - \varepsilon(1-\varepsilon)\langle \nu\rangle.$$

Table I gives the experimentally measured values of $\langle m\rangle$ and $\sigma(m)$ and the values $\langle \nu_{\rm exp}\rangle$ and $\sigma_{\rm exp}(\nu)$ calculated according to the relations given above for $\varepsilon = 7.4\%$. Only the statistical errors are indicated; our estimates show that the systematic errors are $\pm5\%$. Also shown for comparison in Table I are data on the average values of the number of evaporative neutrons $\langle \nu_{\rm th}\rangle$ calculated for protons with energies $E_0 = 4$ and 70 GeV using the SHIELD code,[11] in which a cascade-evaporation model of nuclear fission is implemented.[12] Calculations were carried out for a lead target 60 cm thick and 20 cm in diameter.

It follows from Table I that: 1) the experimental values $\langle \nu_{\rm exp}\rangle$ correspond to an energy dependence $\langle \nu\rangle \sim E^\alpha$, where $\alpha \cong 0.8$, and 2) within the error limits of the measurements $\langle \nu_{\rm exp}\rangle$ is in good agreement with the calculated value $\langle \nu_{\rm th}\rangle$ for $E_0 = 70$ GeV, but it is 20% lower for $E_0 = 4$ GeV. This result was to be expected, since π mesons on average lose less energy to nuclear fissions than do protons on account of the possibility of charge exchange $\pi^\pm \to \pi^0$ on nuclei.

The growth of $\sigma_{\rm exp}(\nu)$ as one goes from $E_0 = 4$ GeV to $E_0 = 70$ GeV is apparently due to the relatively small absorber thickness in the INC ($\sim 3\lambda_{\rm Pb}$) and to the fact that the points of interaction of the primary particles are distributed over depth according to the law $\exp(-x/\lambda_{\rm Pb})$, which should lead to large fluctuations of the energy release in the absorber. Here, as we know, the energy release of the cascade depends on E_0; specifically, the relative fraction of the energy released falls off with increasing E_0 at a fixed absorber depth.[13,14] We propose to explore the nature of the observed large fluctuations in the energy release with the aid of the SHIELD code.

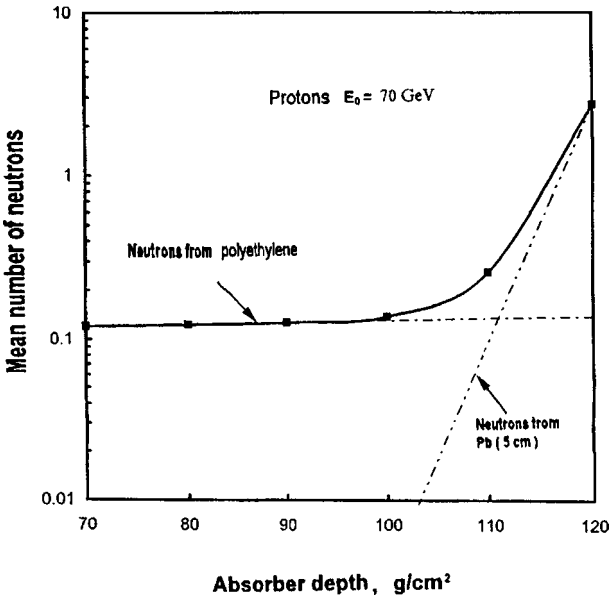

FIG. 2. Mean number of neutrons recorded in the INC versus the polyethylene absorber depth when a layer of lead 5 cm thick is inserted into the 6th layer. (The dashed line shows the distribution of the neutrons from the lead and was obtained by subtracting the number of neutrons generated in the polyethylene).

In our experiment we also measured the distribution of the neutron signal in the INC with an absorber consisting of a combination of light and heavy materials. For this purpose a part of the polyethylene absorber in the 6th layer was replaced by a layer of lead 5 cm thick. Measurements were made in a proton beam with $E=70$ GeV.

The results of the experiment are presented in Fig. 2. We see that replacing the polyethylene with lead increases sharply (20-fold) the number of neutrons registered in the 6th layer relative to the first four layers. This sort of polyethylene–lead transition effect is due to the fact that the number of evaporative neutrons depends substantially on the atomic number A of the absorber. From our data it is easy to estimate the relative number of neutrons generated in the carbon and in lead by using the relation

$$\frac{\langle \nu_C \rangle}{\langle \nu_{Pb} \rangle} = \left(\frac{\Delta x_{Pb}}{\Delta x_C} \right) \left(\frac{\lambda_C}{\lambda_{Pb}} \right) \left(\frac{n_4}{n_6} \right),$$

where λ is the range for interaction of a proton, and n_i is the number of neutrons registered in the ith layer. Taking $\Delta x_{Pb} = 55$ g/cm^2 and $\Delta x_C = 10$ g/cm^2 (Δx is the moderation length), we find that $\langle \nu_C \rangle / \langle \nu_{Pb} \rangle \approx 1/8$. This value corresponds to a dependence $\langle \nu \rangle (A) \sim A^{2/3}$.

The existence of a transition effect for the neutron signal allows one to use absorbers with low atomic numbers A in the INC (the limiting value is $A=1$) and to enhance the signal by interlayering them with thin layers of a heavy absorber ($A \sim 200$). Such a construction of the INC is important for experiments aboard artificial satellites, where the weight of the calorimeter must be minimized while maintaining its luminosity.

The results of this experiment enabled us to carry out a calibration of the SHIELD code, which will be used to design INC structures for Earth satellite measurements of primary electrons and γ rays with energies above 300 GeV and measurements of the composition and energy spectrum of primary particles in the energy interval 10^{14}–10^{16} eV.

The authors are deeply grateful to V. A. Tsarev for his steady interest and support of this study.

This study was carried out with the financial support of the Russian Fund for Fundamental Research under Grant No. 97-02-17867.

[1] N. L. Grigorov, *High-Energy Particles in Cosmic Rays* [in Russian], Nauka, Moscow (1973), 296 pp.
[2] V. S. Murzin and L. I. Sarycheva, *Cosmic Rays and Their Interactions* [in Russian], Atomizdat, Moscow (1968), 356 pp.
[3] W. J. Willis and V. Radeka, Nucl. Instrum. Methods **120**, 221 (1974).
[4] C. Fabjan and R. Wigmans, Rep. Prog. Phys. **52**, 1519 (1989).
[5] D. Bintinger, *Proceedings of the Workshop on Calorimetry for the Supercollider*, Tuscaloosa, Alabama, March 13–17, 1989, p. 91.
[6] J. A. Simpson, W. Fongen, and S. B. Treiman, Phys. Rev. **90**, 934 (1953).
[7] L. I. Dorman, *Experimental and Theoretical Foundations of the Astrophysics of Cosmic Rays* [in Russian], Nauka, Moscow (1975), 256 pp.
[8] V. F. Volovik and I. G. Kozyr', Prib. Tekh. Eksp. No. 2, 38 (1984).
[9] O. G. Ryazhskaya, Doctoral Dissertation [in Russian], Institute of Nuclear Research, Academy of Sciences of the USSR, Moscow (1986).
[10] R. I. Enikeev, G. T. Zatsepin, E. V. Korol'kova *et al.*, Yad. Fiz. **46**, 1492 (1987) [Sov. J. Nucl. Phys. **46**, 883 (1987)].
[11] A. V. Dementyev, N. M. Sobolevsky, and Yu. Yu. Stavissky, Nucl. Instrum. Methods Phys. Res. A **374**, 70 (1996).
[12] V. S. Barashenkov and V. D. Toneev, *Interaction of Particles and High- and Superhigh-Energy Atomic Nuclei with Nuclei* [in Russian], Atomizdat, Moscow (1972), 643 pp.
[13] H. Blumer, Diplomarbeit, Dortmund (1982).
[14] K. Kleinknecht, *Detectors for Particle Radiation*, Cambridge University Press, Cambridge–New York (1986); Mir, Moscow (1990), 220 pp.

Translated by Steve Torstveit

Experiments on interferometric enhanced scattering in a plasma with a nonuniform magnetic field

E. Z. Gusakov, N. M. Kaganskaya, M. Kraemer, P. Morsinchik, and V. L. Selenin

A. F. Ioffe Physicotechnical Institute, Russian Academy of Sciences, St. Petersburg
Ruhr University, Bochum, Germany
(Submitted May 15, 1998)
Pis'ma Zh. Tekh. Fiz. **24**, 43–51 (October 26, 1998)

Results are presented from the first experiments on interferometric enhanced scattering (IES) in a plasma in a nonuniform magnetic field. Measurements of the lower hybrid fluctuations of the plasma density by the IES and rf probe methods in an experimental geometry that models a tokamak configuration are found to be in satisfactory agreement. © *1998 American Institute of Physics.* [S1063-7850(98)02410-0]

The increase in the efficiency of scattering of an electromagnetic wave in the region of its hybrid resonance has been widely used in the last decade for studying fluctuations and waves in magnetized plasmas. [1] The method of enhanced scattering (ES), which is based on this effect, has a high sensitivity to small-scale fluctuations and has good spatial resolution. An important advantage of the method is that it is an integral method with respect to wave numbers, a property which lessens the requirements on the necessary amount of prior information about the properties of the investigated wave phenomena and simplifies the design of experiments. At the same time, of course, the integral nature of the method means it has a lower resolution with respect to the wave vectors of the fluctuations under study.

Recently two modifications of the diagnostics of enhanced scattering were proposed, which combine the main advantages of the method with the possibility of making wave-vector-resolved measurements of the oscillations under study. The first, the time-of-flight modification of the enhanced scattering method, is based on the linear dependence of the delay time of the radiation scattered from the hybrid resonance on the wave vector of the scattering vibrations. [2] The second, the correlation or interferometric modification (IES), uses the dependence of the scattered signal A_{ES} on the phase of the fluctuations at the point of the hybrid resonance. [3,4]

According to Ref. 4, in the case when the launching antenna is simultaneously the receiving antenna, the backscattered signal has the form

$$A_{\mathrm{ES}}(t,x_r)=\frac{i\omega_i A_i}{16\pi}\int\frac{d\Omega d^3\mathbf{q}dk_{iy}dk_{iz}}{(2\pi)^6}\frac{\delta n_{\Omega,\mathbf{q}}}{n_e}\times e^{i\Omega t-iqx_r(\omega_i)-iq_z z_i-iq_y y_i}f(k_{iy},k_{iz})\times f(q_y-k_{iy},q_z-k_{iz})\cdot\Theta\cdot I(\mathbf{q}),\qquad(1)$$

where $|A_{\mathrm{ES}}|^2$ and $|A_i|^2$ are the powers of the scattered and probe radiation, $\delta n_{\Omega,q}$ is the Fourier harmonic of the electron density fluctuation; q is the projection of the wave vector of a fluctuation onto the direction of inhomogeneity of the plasma, q_z and q_y are the projections of the wave vector of the fluctuation onto, respectively, the magnetic field direction and onto the direction perpendicular to both the magnetic field and the direction of inhomogeneity of the plasma, $f(k_{iy},k_{iz})$ is the directional pattern of the transmitting and receiving antenna, z_i and y_i are the coordinates of the antenna, Θ is the fraction of the power of the probe radiation that is absorbed at the upper hybrid resonance, and $I(q)$ is the enhancement factor describing the efficiency of the enhanced scattering. [1,5]

In the case of enhanced scattering at the upper hybrid resonance in a cold plasma having small geometric dimensions $l=[(l/n)(dn/dx)]^{-1}\ll c/\omega_i$, $q<(l\rho_{\mathrm{He}}^2)^{-1}$, one has $I(q)\sim q$, according to Ref. 1. As we see from Eq. (1), the enhanced scattering signal depends on the position of the hybrid resonance $x_r(\omega_i)$. If the density perturbation is harmonic and one-dimensional, $\delta n_\Omega\sim\delta(\Omega-\Omega_0)\delta q_y\delta q_z$, this dependence can be used to reconstruct the relative density perturbation of the plasma in the wave from interferometric measurements. [4] Indeed, in that case

$$\delta n_\Omega(x)\sim N_{\mathrm{IES}}(x)=\int_{-\infty}^{+\infty}\frac{dq}{2\pi q}e^{-iqx}\int_{-\infty}^{+\infty}dx_r e^{iqx_r}A_{\mathrm{IES}}(x_r),\qquad(2)$$

where $A_{\mathrm{IES}}(x_r)=\langle e^{-i\Omega t}A_{\mathrm{ES}}(t,x_r)\rangle_t$.

In the case of more complex non-one-dimensional density perturbations, IES can be used to estimate the characteristic wavelengths of harmonic oscillations propagating in the plasma.

In this paper we use the IES method for the first time in a situation in which the magnetic field is nonuniform and the region of the upper hybrid resonance is accessible to waves excited from outside. The results of measurements of the spatial distribution of test waves of the lower hybrid frequency range are compared with the data of independent measurements made by the interferometric probe technique. The experiments were carried out on the linear apparatus ''Boxes,'' [6] in which a tokamak-like magnetic field configuration was produced by a certain rotation of the magnetic coils with respect to each other. The effective major radius of the tokamak was 70 cm. The plasma was created by a pulsed

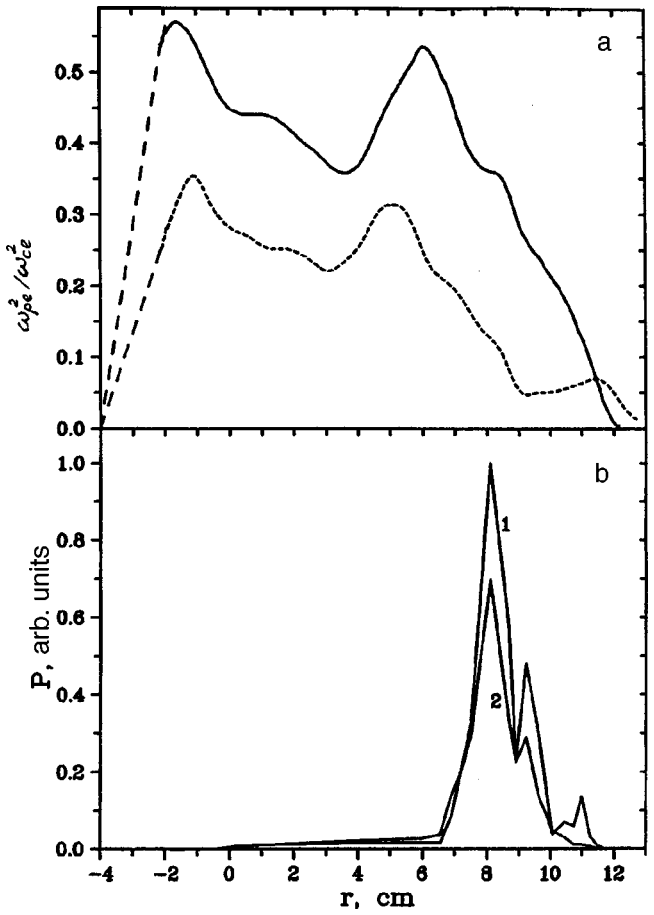

FIG. 1. a: Distribution of the electron density of a plasma along the direction of nonuniformity of the magnetic field. The solid curve corresponds to the time of the rf pulse, while the dashed curve corresponds to some time after the end of the pulse, when the interferometric measurements were made. b: The backscattered signal from spontaneous fluctuations of the plasma versus the position of the upper hybrid resonance. The red-shifted (curve *1*) and blue-shifted (curve *2*) components of the scattering spectrum.

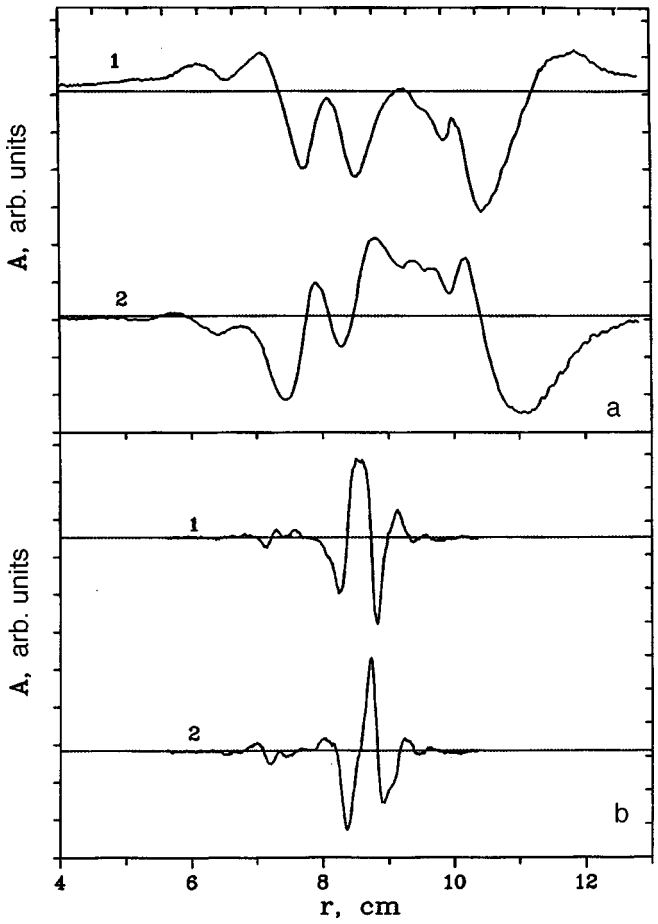

FIG. 2. Interferograms obtained using rf probes (a) and the IES method (b) for a lower hybrid test wave at frequency $f_0=23$ MHz for two values of the phase of the reference signal shifted relative to each other by 90° (curves *1* and *2*).

rf discharge between two plane electrodes placed at the ends of the chamber ($f_{\mathrm{rf}}=55$ MHz, $P_{\mathrm{rf}}<200$ W, $\tau_{\mathrm{rf}}=20$ μs). The parameters of the plasma during the pulse are $n_e \leqslant 2\times10^{10}$ cm^{-3}, $T_e<4$ eV, $P=1$ Pa.

The distribution of the electron density of the plasma along the direction of nonuniformity of the magnetic field is shown in Fig. 1a. The solid curve corresponds to the time of the rf pulse, while the dashed curve corresponds to some time after the end of the pulse, when the interferometric measurements were made. The lower hybrid antenna exciting the test wave was placed on the low-magnetic-field side of the apparatus at $x=9$ cm (Fig. 1a) and was shifted by 12 cm along the magnetic field relative to the symmetry plane of the apparatus. The scheme used to excite the probe wave is analogous to tokamak experiments. Microwave radiation at a frequency $f_i=2.45$ GHz with a power $P_i=100$ mW was brought into the plasma from the high-magnetic-field side with the aid of a waveguide antenna placed in the equatorial plane at $x=-2$ cm. The behavior of the enhanced scattering signal corresponded to the case of a tokamak geometry of the magnetic field, as was demonstrated with particular clarity in an experiment on the scattering on spontaneous fluctuations of the plasma. Figure 1b shows how the signal of radiation backscattered on spontaneous fluctuations of the plasma depends on the position of the upper hybrid resonance, calculated according to the formula $\omega_i^2=\omega_{pe}^2(x_r)+\omega_{ce}^2(x_r)$. The position of the upper hybrid resonance was scanned by changing the frequency of the probe radiation. Both components of the scattering spectrum, the red-shifted (curve *1*) and blue-shifted (curve *2*), were observed only under the condition such that the upper hybrid resonance exists inside the plasma. The ES signal reached its maximum value in the region $6\,\mathrm{cm}<x_r<10$ cm, where the electron cyclotron layer lies within the plasma and the upper hybrid resonance is accessible. Such behavior of the enhanced scattering signal is characteristic for tokamak experiments. [1]

The results of an IES experiment for a lower hybrid test wave at frequency $f_0=23$ MHz are shown in Fig. 2b. The interferograms were taken at two values of the phase of the reference signal, shifted with respect to each other by 90° (curves *1* and *2*). We see that the IES signal is localized at the outer part of the plasma density profile (Fig. 1a). At the same time, the interferograms obtained with rf probes (Fig. 2a) have a wider spatial distribution and occupy the entire gradient region (curves *1* and *2* also correspond to reference signals with a phase shift of 90° between them).

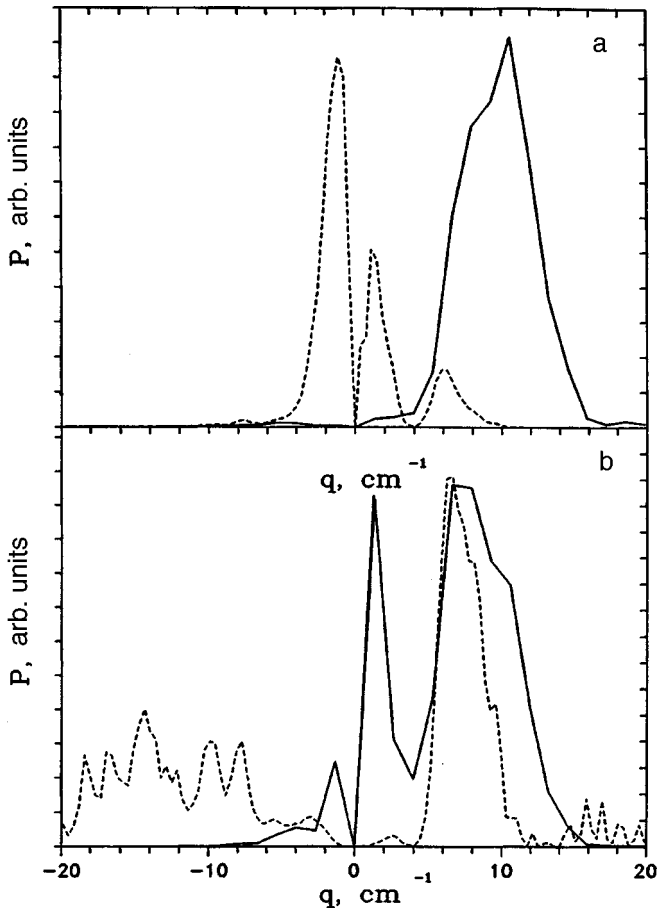

FIG. 3. a: Spatial Fourier spectra obtained from the interferograms shown in Fig. 2. The dashed curve is the IES spectrum, while the solid curve is the spectrum from the rf probes. b: The spectra $\tilde{N}_{\mathrm{IES}}(q)$ (solid curve) and $\tilde{N}_{\mathrm{rf}}(q)$ (dashed curves) ($P\sim\tilde{N}^2(q)$) obtained from the data in Fig. 3a.

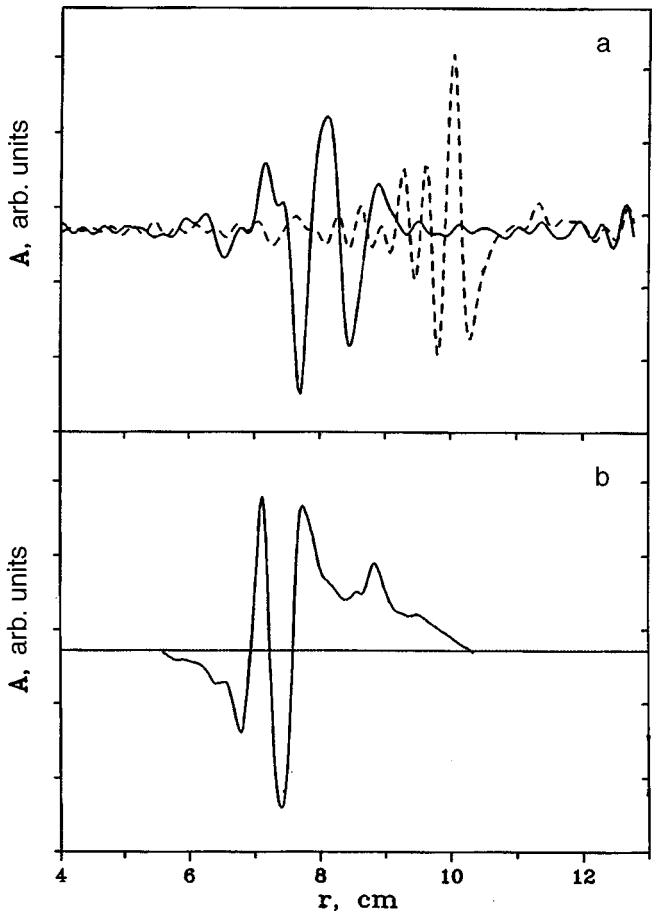

FIG. 4. a: Spatial structure of the perturbation of the electron density $\delta N_{\mathrm{rf}}(x)$ recovered from the rf probe data in Fig. 3b: $\delta N_{\mathrm{rf}}(x)^{q>0}$ (solid curve), $\delta N_{\mathrm{rf}}(x)^{q<0}$ (dashed curve). b: Spatial structure of the perturbation of the electron density $\delta N_{\mathrm{IES}}(x)$ recovered from the IES data of Fig. 3b.

The Fourier spectra obtained from these interferograms (Fig. 3a) differ strongly from each other. The spatial spectrum $P(q)$ of the ES signal ($P\sim\tilde{A}^2_{\mathrm{IES}}$) (solid curve) is localized in the region of positive wave vectors q, which corresponds to the phase of the wave propagating out of the plasma. The spatial spectrum $P(q)$ of the signal from the rf probe ($P\sim\tilde{A}^2_{\mathrm{rf}}$) (dashed curve) is also asymmetric, but it has a dominant component localized in the region of negative q. Another important difference in the ES spectrum is its comparatively short-wavelength character. This difference can be explained by considering the different sensitivities of the given diagnostics in different wavelength ranges. The rf probes measure the plasma potential and are more sensitive to long-wavelength perturbations of the plasma density, whereas the ES method, because the enhancement factor has the linear dependence $I(q)\sim q$, is more sensitive in the short-wavelength part of the spectrum. The difference in sensitivity of these diagnostics to fluctuations on different spatial scales can be taken into account in the reconstruction of the spatial structure of the density perturbations. Indeed, it follows from the Poisson equation $\Delta\varphi=-4\pi(\rho_i+\rho_e)$ that the density perturbations have the behavior $\tilde{N}_{\mathrm{rf}}(q)\sim q^2\tilde{A}_{\mathrm{rf}}$, while expression (2) gives $\tilde{N}_{\mathrm{IES}}(q)\sim q^{-1}\tilde{A}_{\mathrm{IES}}$.

The parts of the spectra $\tilde{N}_{\mathrm{IES}}(q)$ (solid curve) and $\tilde{N}_{\mathrm{rf}}(q)$ (dashed curve) ($P\sim\tilde{N}^2(q)$) lying in the region of positive q both have the same behavior, while the parts in the region of negative q do not, as can be seen from Fig. 3b. The reason for this disparity can be explained on the basis of Fig. 4, which shows plots of the depenences $\delta N_{\mathrm{rf}}(x)^{q<0}$ (dashed curve in Fig. 4a), $\delta N_{\mathrm{rf}}(x)^{q>0}$ (solid curve in Fig. 4a), and $\delta N_{\mathrm{IES}}(x)$ (Fig. 4b), which were each recovered from the Fourier spectra in Fig. 3b. We see from Fig. 4 that the position and spatial structure of the density perturbation recovered from the IES data $\delta N_{\mathrm{IES}}(x)$ basically match that recovered from the positive part of the Fourier spectrum of $\delta N_{\mathrm{rf}}(x)^{q>0}$ obtained with the rf probes. They lie along the upper part of the density profile (Fig. 1a), which is accessible to microwave probing in the ES method. The density perturbation $\delta N_{\mathrm{rf}}(x)^{q<0}$ lies in the region of the small ''hump'' on the density profile in Fig. 1a. This part of the plasma is inaccessible to the probe wave (Fig. 1b). This is apparently the reason for the suppression of the negative part of the spectrum in the IES signal.

In closing it should be noted that the results presented here represent the first application of IES under conditions where the magnetic field configuration approaches that in a tokamak. We have shown that the results on the fluctuations of the plasma density in the lower hybrid wave as obtained

by the IES and rf probe diagnostics are in good agreement with each other, so that one is justified in using them for investigation of short-wavelength oscillations in a toroidal plasma.

This study was supported by DFG Grants SFB 191 and 146 113/146, Grant No. 96-02-17913 From the Russian Fund for Fundamental Research, and ''Scientific School'' Grant No. 96-15-96367.

[1] K. M. Novik and A. D. Piliya, Plasma Phys. Controlled Fusion **35**, 357 (1993).

[2] V. I. Arkhipenko *et al.*, Plasma Phys. Controlled Fusion **37**, 347 (1995).

[3] V. I. Arkhipenko, V. N. Budnikov, E. Z. Gusakov, V. L. Selenin, and L. V. Simonchik, Pis'ma Zh. Tekh. Fiz. **19**(11), 20 (1993) [Tech. Phys. Lett. **19**, 333 (1993)].

[4] E. Z. Gusakov, N. M. Kaganskaya, M. V. Lvov, and V. L. Selenin, *International Conference on Plasma Physics*, Nagoya, Japan, September 9–13, 1996, Contributed papers, Vol. 2.

[5] B. Bruesenhaber, E. Z. Gusakov, M. Kraemer, and A. D. Piliya, Plasma Phys. Controlled Fusion **36**, 997 (1994).

[6] B. Bruesenhaber and M. Kraemer, Plasma Phys. Controlled Fusion **39**, 389 (1997).

Translated by Steve Torstveit

On the epitaxy of aluminum nitride on silicon substrates in a chloride–hydride process

A. N. Efimov, A. O. Lebedev, and A. M. Tsaregorodtsev

A. F. Ioffe Physicotechnical Institute, Russian Academy of Sciences, St. Petersburg
(Submitted March 27, 1998)
Pis'ma Zh. Tekh. Fiz. **24**, 52–57 (October 26, 1998)

The technological conditions under which the silicon surface interacts with vapor-phase reactants present in a chloride–hydride system for the epitaxial growth of aluminum nitride are determined. The method of electron channeling patterns is used to show that the growth of single-crystal layers of AlN on silicon substrates in the chloride–hydride system is hindered by the interaction of the silicon with NH_3 in the presence of HCl at $T \geqslant 800\,^{\circ}C$, with the formation of an amorphous layer of Si_3N_4. To obtain a high-quality texture it is important that prior to deposition of the AlN layers the silicon substrates be held in an NH_3 atmosphere in order to form a dense layer of Si_3N_4. Single-crystal growth of AlN can be achieved in a chloride–hydride system of chemical deposition from the vapor phase at a reduced pressure, since the deposition temperature is then substantially lower (down to 550 °C) and the chemical interaction with the substrate is hindered. © *1998 American Institute of Physics.* [S1063-7850(98)02510-5]

The heteroepitaxy of aluminum nitride on silicon is of significant interest for fabricating rf and SAW (surface acoustic wave) devices.[1] One of the preferred methods of obtaining AlN epitaxial layers is the chloride–hydride method of chemical deposition from the vapor phase in the Al–HCl–NH_3 system.[2–4] This method gives a high rate of deposition and high structural perfection of the AlN layers in epitaxy on sapphire or silicon carbide substrates,[3,4] but the growth of single-crystal layers of aluminum nitride on silicon by the chloride–hydride method has not yet been achieved.

There has been a report[5] of the growth of textured layers of AlN with a predominantly azimuthal orientation on Si(111): AlN(0001)//Si(111), AlN$(11\bar{2}0)$//Si(220), at a substrate temperature of 1150 °C in the system $AlCl_3-NH_3-H_2$ (Ref. 5). At the same time, these data are contrary to the results of a number of papers (Refs. 6 and 7, and others), which have in common the ''low-temperature'' ($T = 850\,^{\circ}C$) growth of textured (0001) layers of AlN with the complete absence of azimuthal orientation. Because the (0001) texture has been grown without visible differences on Si(111), Si(100), $SiO_2/Si(111)$, and quartz glass substrates, it is clear that the substrate does not have any orienting effect. At temperatures above 1300 °C the predominant orientation in the layers vanished, evidently on account of the induced temperature instability of the substrate and its reaction with ammonia to form an amorphous layer of Si_3N_4 (Ref. 5). It should be noted, however, that temperatures of the order of 1100–1200 °C and amounts of ammonia similar to those used in the chloride–hydride method have been used successfully for the growth of single-crystal layers on silicon by the method of metalorganic synthesis (e.g., in the system $Al(CH_3)_3-NH_3$; Ref. 1). In Ref. 8 it was conjectured that the conditions for the formation of an amorphous Si_3N_4 layer are improved in the presence of significant quantities of oxygen and hydrogen chloride.

The goal of the present study was to determine the technological conditions under which an interaction of the silicon surface with vapor-phase reactants present in the chloride–hydride system will occur. Silicon substrates with the orientations (100) and (111) were placed in the reactor described in Ref. 3 in the temperature-gradient zone ($T = 600-1100\,^{\circ}C$), where they were held for several hours in different gaseous media (Ar, $Ar+NH_3$, $Ar+NH_3+HCl$, $Ar+AlCl_3+H_2$). The $AlCl_3$ was obtained directly in the reactor in the interaction of aluminum with a flow of hydrogen chloride (in accordance with the technological scheme for this process set forth in Ref. 3). The efficiency of conversion of hydrogen chloride in the chlorination reaction ($2Al+6HCl = 2AlCl_3+3H_2$) is at least 98%. The state of the substrate surface after the experiment was investigated by the method of electron channeling patterns.[9,10]

The method of electron channeling patterns can be used for solving the same problems as the electron diffraction method, but, unlike the latter, it is local (spot diameter ~100 Å). The channel patterns were observed directly under an REM-100U scanning electron microscope. Scanning of the beam in wave-vector k space was effected by varying the angle of incidence of the electrons on the sample while the point of incidence of the beam remained constant. The set of lines corresponding to satisfaction of the Bragg condition for the different crystallographic planes was observed on a video monitor. The contrast of the channeling patterns was generally low. Therefore, to observe the patterns it was necessary to meet a number of experimental conditions,[9] in particular, to use methods of image processing to heighten the contrast.[10]

It turns out that for analyzing the conditions corresponding to corrosion of the silicon surface, a simple comparison of the degree of resolution of the channeling patterns can be used. Figure 1 shows as an example the electron channeling patterns from silicon samples held in ammonia at temperatures of 850 °C (a) and 950 °C (b). The results of a qualita-

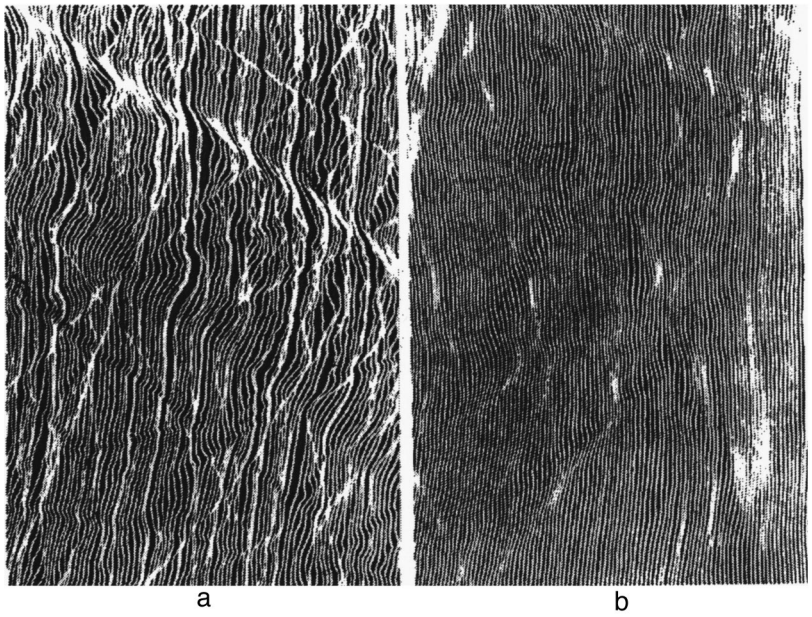

FIG. 1. Electron channeling patterns from silicon samples held in a medium of ammonia (see text).

tive study of the channeling patterns are presented in Table I. The temperatures given in Table I are practically independent of the substrate orientation, (111) or (100).

We did a thermodynamic calculation of the equilibrium constants of the some of the proposed reactions between silicon and the vapor-phase reactants. The initial data for the calculation were taken from Ref. 11, and the results are presented in Table II.

The lowering of the contrast in an ammonia medium is due to the forward reaction of the nitriding of silicon by ammonia, the starting temperature of which is estimated as 900 °C (Ref. 12), and the lowering of the nitriding reaction rate at temperatures below 900 °C is due not to thermodynamic but to kinetic limitations (reaction 1, Table II). At the same time, in spite of the fact that the thermodynamic equilibrium of the nitriding reaction is shifted quite strongly toward the nitride side, upon the formation of a dense layer of silicon nitride the reaction slows down.[12] The addition of hydrogen chloride to the reaction flux intensifies the process, probably on account of a continual renewal of the reaction surface (e.g., in the chloriding of silicon by reaction 2 in Table II) and the decompactification of the nitride layer by chlorine derivatives of silicon. A thermodynamic analysis of the chemical reactions in the system Si–H–Cl in Ref. 13 permits identification of the most probable reaction products of the chloriding of silicon: in addition to H_2 and $SiCl_4$, there is also $SiHCl_3$, $SiCl_2$, and SiH_2Cl_2.

Placing silicon in a medium containing $AlCl_3$ and H_2 led to etching of the substrate surface and to the formation of deep etch pits having a symmetric shape and a dimension of 10–100 μm. We interpret this as being the result of an interaction of the substrate with microscopic droplets of aluminum, but the concrete mechanism of the process is unclear: since from $K_p < 10^{-10}$ for reactions 3 and 4 in Table II, the hydrogenation of silicon is also hindered.[13]

In closing, it should be said that the growth of single-crystal films of aluminum nitride on silicon substrates in the chloride–hydride system is made difficult by the interaction of the silicon with NH_3 in the presence of HCl at $T \geqslant 800\,^{\circ}C$, with the formation of an amorphous layer of Si_3N_4. At the same time, for a number of applications, in particular, in acoustoelectronic devices based on AlN, it is

TABLE I. Temperatures of the lowering of the contrast of the electron channeling patterns.

Gaseous medium	Temperature at which the lowering of the contrast begins, °C	Temperature at which the sharp degradation of the contrast occurs, °C	Notes
Ar	Lowering of contrast absent all the way up to 1000°C		
$Ar+NH_3$ (ammonia partial pressure <0.7 bar)	880−900	950	
$Ar+NH_3+HCl$	700−800	880	
$Ar+AlCl_3+H_2$	>950		Etching of the surface and silicon

TABLE II. Equilibrium constants for chemical reactions corroding the substrate

Reaction No.	Reaction	T, K	K_p, bar^n
1	$3Si_{(s)}+4NH_{3(g)}=Si_3N_{4(s)}+6H_{2(g)}$	1073	6.8×10^{32}
		1173	5.4×10^{30}
		1273	3.5×10^{28}
2	$Si_{(s)}+4HCl_{(g)}=SiCl_{4(g)}+2H_{2(g)}$	1073	3.1×10^{5}
		1173	2.7×10^{4}
		1273	2.2×10^{3}
3	$Si_{(s)}+2AlCl_{3(g)}=2AlCl_{(g)}+SiCl_{4g}$	1073	8.9×10^{-14}
		1173	3.4×10^{-12}
		1273	1.1×10^{-10}
4	$3Si_{(s)}+4AlCl_{3(g)}=4Al_{(l)}+3SiCl_{4(s)}$	1073	3.5×10^{-28}
		1173	1.9×10^{-26}
		1273	7.2×10^{-25}

sufficient to use (0001) textured films of aluminum nitride. To obtain a high-quality texture it is important to subject the silicon substrates prior to deposition of the AlN layers to a hold in an NH_3 atmosphere for the formation of a dense layer of Si_3N_4. The single-crystal growth of AlN can be achieved with the use of a chloride–hydride system of chemical vapor deposition at reduced pressure, so that the deposition temperature will be substantially lower (down to 550 °C; Refs. 14 and 15) and the chemical interaction with the substrate will be hindered.

[1] S. Strite and H. Morkoc, J. Vac. Sci. Technol. **10**, 1237 (1992).
[2] M. P. Callaghan, E. Patterson, B. P. Richards *et al.*, J. Cryst. Growth **22**, 85 (1974).
[3] F. Bugge, A. N. Efimov, I. G. Pichugin *et al.*, Cryst. Res. Technol. **22**, 65 (1987).
[4] A. O. Lebedev, Yu. V. Mel'nik, and A. M. Tsaregorodtsev, in *Proceedings of the First International Conference on Epitaxial Crystal Growth*, Budapest (1990), pp. 116–118.
[5] A. J. Noreika and D. W. Ing, J. Appl. Phys. **39**, 5578 (1968).
[6] F. F. Grekov, D. M. Demidov, and A. M. Zykov, Zh. Prikl. Khim. **51**, 1450 (1978).
[7] I. Bauer, L. Biste, and D. Bolze, Phys. Status Solidi A **39**, 173 (1977).
[8] E. Butter, Thin Solid Films **59**, 25 (1979).
[9] V. I. Petrov (Ed.), *Practial Scanning Electron Microscopy* [in Russian], Mir, Moscow (1978), 656 pp.
[10] A. N. Efimov and V. Yu. Florinskiĭ, Zh. Tekh. Fiz. **61**(8), 188 (1991) [Sov. Phys. Tech. Phys. **36**, 954 (1991)].
[11] V. P. Glushko (Ed.), *Thermodynamic Properties of Individual Substances* [in Russian], Vols. 1–4, Nauka, Moscow (1978).
[12] V. I. Belyĭ, L. P. Vasil'eva, and V. A. Grishchenko *et al.*, *Silicon Nitride in Electronics* [in Russian], Nauka, Novosibirsk (1978), 112 pp.
[13] I. M. Skvortsov, I. I. Lapidus, and B. V. Orion *et al.*, *Technology and Apparatus of Vapor-Phase Epitaxy of Silicon and Germanium* [in Russian], Energiya, Moscow (1978), 136 pp.
[14] Y. G. Roman and A. P. M. Adriaansen, Thin Solid Films **169**, 241 (1989).
[15] K. Kaya, Y. Kanno, H. Takahashi *et al.*, Jpn. J. Appl. Phys. **35**, 2782 (1996).

Translated by Steve Torstveit

Apparatus for growing GaN films on large-area substrates by the method of chloride–hydride vapor-phase epitaxy

S. I. Stepanov, D. V. Tsvetkov, and A. E. Cherenkov

A. F. Ioffe Physicotechnical Institute, Russian Academy of Sciences, St. Petersburg
Center for Research on Crystal Growth, St. Petersburg
(Submitted April 21, 1998)
Pis'ma Zh. Tekh. Fiz. **24**, 58–65 (October 26, 1998)

A prototype industrial apparatus for growing gallium nitride (GaN) epitaxial films by the method of vapor-phase epitaxy in the chloride–hydride system is designed and built. Epitaxy is carried out simultaneously on 3 silicon carbide (SiC) substrates 35 mm in diameter. The distribution of growth rates along the gas flow and over the transverse cross section of the reactor is investigated. The epitaxial films are studied by x-ray diffraction and photoluminescence methods. © *1998 American Institute of Physics.* [S1063-7850(98)02610-X]

Nitrides of group-III metals (AlN, GaN, InN) are promising materials for fabricating high-efficiency blue and green light-emitting diodes,[1–3] short-wavelength injection lasers,[4] and other electronic devices. Significant progress in the epitaxy of these compounds from metalorganic compounds[4] and by molecular-beam epitaxy[5] has been reported. The chloride–hydride method of growing epitaxial layers of group-III nitrides is also of great interest, since it has a number of advantages over the methods mentioned: a wide range of growth rates ($0.05-2\ \mu$m/min),[6] and a rather low cost of equipment and experimentation. Previously our group has demonstrated the possibility of growing high-quality epitaxial films of AlN on sapphire[7] and silicon carbide (SiC)[12] substrates, GaN films on silicon carbide substrates,[8] and a GaN $p-n$ junction[9] and solid solutions of AlGaN on silicon carbide substrates[10] by a modified chloride–hydride method. However, these results have all be obtained on laboratory apparatus. In this paper we describe a prototype of an industrial chloride–hydride apparatus and present the results of the first experiments on the use of this apparatus to grow GaN epitaxial films on silicon carbide substrates.

The main requirements on the construction of the chloride–hydride apparatus were that it permit: 1) growth on substrates up to 80 mm in diameter; 2) growth on three or more substrates up to 50 mm in diameter; 3) carrying out up to 10 growth processes in a single technological cycle. These requirements guided the design of the reactor whose plan is shown in Fig. 1. It is based on the scheme of a horizontal reactor of the blow-through type with hot walls. The apparatus consists of a quartz reactor, multizone furnace with resistive heating, and a vapor unit. The furnace was divided into two temperature zones: a source zone and a growth zone. The temperature in the growth zone can be varied from 900 to 1150°C. Argon with a purity of 99.997% was used as the carrier gas. The sources were metallic Ga (99.9997%) and gaseous NH_3 (99.999%). HCl with a purity of 99.998% was used for chloriding the Ga. In the source zone the hydrogen chloride interacts with the metallic gallium to form gaseous gallium chloride. In the growth zone the GaCl vapor reacts with the ammonia to form GaN. The gallium nitride that is formed settles on the walls of the reactor and on the substrates. In the growth zone the substrates are placed on a pedestal parallel to the gas flow. The dimensions of the working growth zone are 200×80 mm.

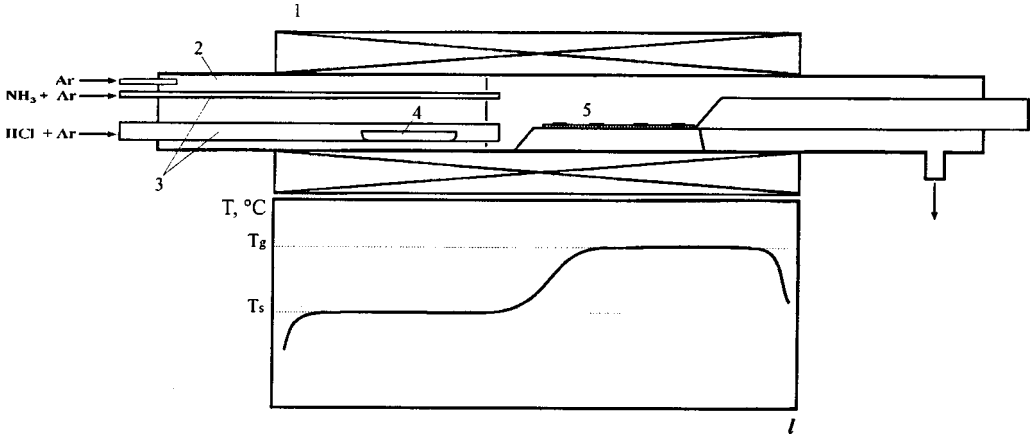

FIG. 1. Diagram of the apparatus for growing group-III nitrides by the chloride–hydride method: *1* — multizone furnace with resistive heating; *2* — quartz reactor; *3* — gas-channel pipes; *4* — boat containing the group-III metal; *5* — pedestal with substrates.

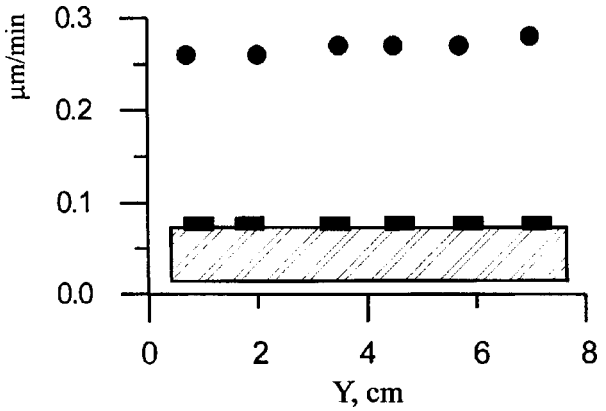

FIG. 2. Distribution of the growth rate of GaN films on SiC substrates over the transverse cross section of the reactor.

In this reactor design the grown structures can be cooled in an inert gas flow and removed without cooling the entire reactor.

The apparatus was used in experiments on the growth of gallium nitride films on silicon carbide substrates. The epitaxy was carried out on 6*H*-SiC substrates 35 mm in diameter, produced by Cree Research, Inc. Small companion substrates, which were SiC crystals grown by the Lely method or fragments of the Cree Research substrates, were placed next to the main substrates. The gallium nitride epitaxy was done without the use of buffer layers.[11] The epitaxial layers were not deliberately doped. Growth was carried out for 5–10 min.

The thickness of the epitaxial film was measured gravimetrically (from the difference of the weights of the substrates before and after the growth) and with an interference microscope, by observation of the interference fringes from the heterointerface and surface of the film. The uncertainty in the determination of the thickness by these methods was not more than 10%.

The distribution of the growth rate of the GaN along the length of the pedestal (in the direction parallel to the gas flow) showed that there is a region within the growth zone about 15 cm long in which the growth rate does not vary by more than 10%. Figure 2 shows the distribution of the growth rate in the direction perpendicular to the gas flow. It can be seen that there are practically no edge effects, and the scatter in the values of the growth rate lies within the error of measurement (10%).

To assess the capabilities of the epitaxy apparatus we performed an experiment on the growth of GaN films on three SiC substrates with diameters of 35 mm. On all three substrates located in the working growth zone the GaN films had a smooth mirror surface. The GaN films were investigated by the x-ray diffraction and photoluminescence methods. The half-width of the x-ray rocking curve measured in the ω-scanning geometry lay in the interval from 72 to 150″ (seconds of arc), values indicative of a high structural perfection of the films. The value 72″ stands as the best result obtained to date for GaN films grown on SiC without a buffer layer. A typical rocking curve for epitaxial GaN on SiC, measured in the ω-scanning geometry, is shown in

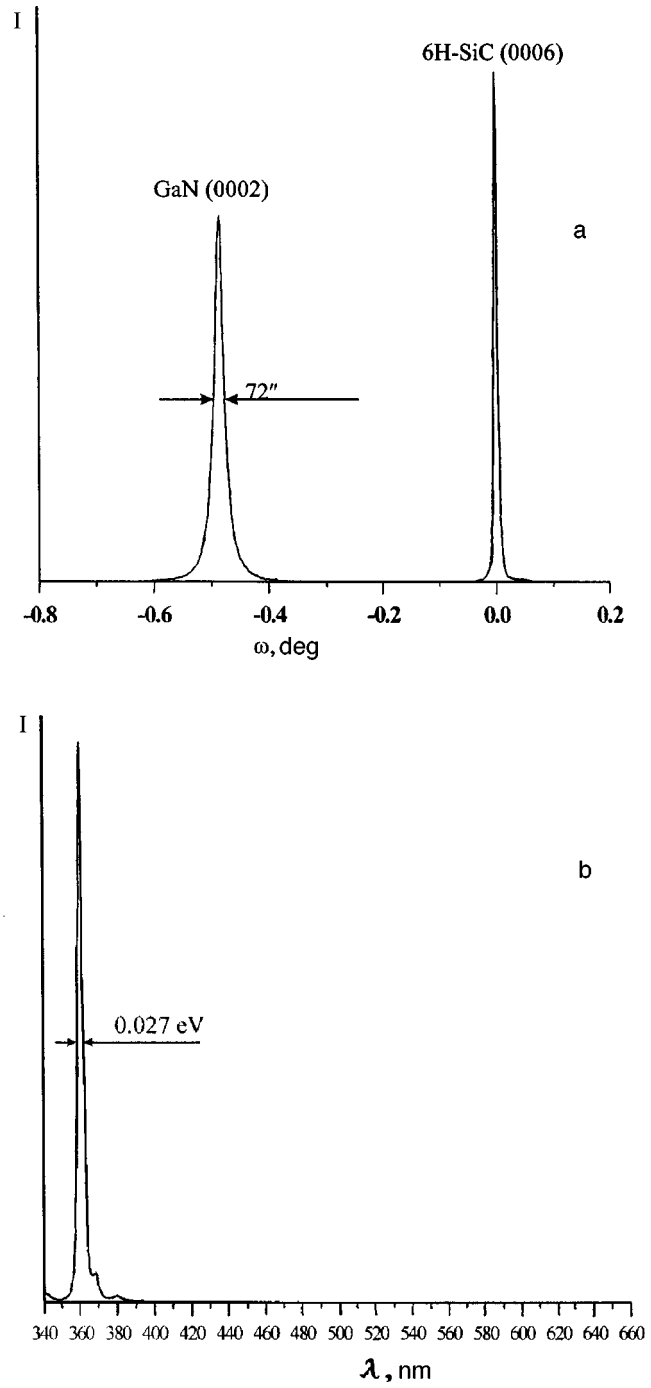

FIG. 3. a: X-ray rocking curve measured in the ω-scanning mode for a GaN epitaxial film grown on SiC; b: photoluminescence spectrum of a GaN epitaxial film grown on SiC. The photoluminescence spectrum was taken at a temperature of 100 K using a N_2 laser.

Fig. 3a. The photoluminescence spectra of all the samples are dominated by the exciton luminescence band (Fig. 3b). The half-width of the edge peak at 100 K lies in the interval from 27 to 30 meV. The films had *n*-type conductivity. The typical concentration $N_d - N_a$, measured by a mercury probe, lay in the interval $1\times10^{17}-5\times10^{17}$ cm^3.

For estimating the uniformity of the GaN films on the three SiC wafers (35 mm in diameter) we measured the half-widths of the x-ray rocking curves and the half-widths and intensities of the edge peak of the photoluminescence. The

measurements were made on each wafer at several points along the gas-flow direction and perpendicular to it. The half-width of the photoluminescence edge peak measured at 100 K on the wafer that had been in the first position along the gas flow varied within the limits 0.020–0.022 eV over the area of the wafer. For the second and third wafers the ranges of variation were 0.023–0.027 eV and 0.024–0.028 eV, respectively. The half-widths of the x-ray rocking curves varied over the area of the three wafers within the range 72–170″. This scatter may arise because the epitaxial films follow the structural quality of the substrates.[11] For the SiC wafers used as substrates in this experiment the half-width of the x-ray rocking curves varied in the range 17–40″, which, under otherwise equal conditions, would entail a broadening of the rocking curves of the epitaxial films grown on the less perfect substrates.

In summary, we have built a prototype industrial apparatus for the epitaxial growth of group-III nitrides by the chloride–hydride method on large-diameter substrates (up to 80 mm). This apparatus was used to grow high-quality epitaxial films of GaN on SiC substrates with a diameter of 35 mm. The data on the uniformity of the characteristics of the films and of the growth rate of the GaN epitaxial films over the length of the working growth zone (15–20 cm) suggest that it should be possible to grow epitaxial films of gallium nitride on several substrates with diameters up to 80 mm in a single growth process.

The authors thank Yu. Mel'nik, A. Nikolaev, and I. Nikintina for helpful discussions, N. Seredova for doing the optical studies on the samples, and the University of Arizona for support of this study.

[1] S. Nakamura, M. Senoh, and T. Mukai, Appl. Phys. Lett. **62**, 2390 (1993).
[2] H. Morkoc, S. Strite, G. B. Gao, M. E. Lin, B. Sverdlov, and M. Burns, J. Appl. Phys. **76**, 1363 (1994).
[3] S. Nakamura, M. Senoh, N. Isawa, and S. Nahagama, Jpn. J. Appl. Phys. Lett. **34**, L797 (1995).
[4] S. Nakamura, M. Senoh, S. Nagahama, N. Iwasa, T. Yamada, T. Matsushita, H. Kiyoku, Y. Sugimoto, T. Kozaki, H. Umemoto, M. Sano, and K. Chocho, *Proceedings of the Second Internationl Conference on Nitride Semiconductors. ICNS'97*, Tokushima, Japan, October 27–31, 1997, p. 444.
[5] M. Schauler, C. Kirchner, M. Mayer, A. Pelzmann, F. Eberhard, M. Kamp, P. Unger, and K. J. Ebeling, MRS Internet J. Nitride Semicond. Res. **2**, 44 (1997).
[6] T. Detchprohm, K. Hiramatsu, H. Amano, and I. Akasaki, Appl. Phys. Lett. **61**, 2688 (1992).
[7] A. O. Lebedev, Yu. V. Melnik, and A. M. Tsaregorodtsev, Inst. Phys. Conf. Ser. 137 (1994), Chap. 4, p. 405.
[8] Yu. Melnik, I. P. Nikitina, A. S. Zubrilov, A. A. Sitnikova, Yu. G. Musikhin, and V. A. Dmitriev, Inst. Phys. Conf. Ser. 142 (1996), Chap. 5, p. 863.
[9] A. E. Nikolaev, Yu. V. Melnik, N. I. Kuznetsov, A. M. Strelchuk, A. P. Kovarsky, K. V. Vassilevski, and V. I. Dmitriev, ''GaN *pn*-structures grown by hydride vapor phase epitaxy,'' Presented at the MRS 97 Fall Meeting.
[10] Yu. Melnik, A. Nikolaev, S. Stepanov, A. Zubrilov, I. Nikitina, and V. Dmitriev, *Book of Abstracts of the E-MRS Spring Meeting* (1997), L 22.
[11] Yu. V. Melnik, I. P. Nikitina, A. E. Nikolaev, and V. A. Dmitriev, Diamond Rel. Mater. **6**, pp. 1532–1535 (1997).
[12] Yu. Melnik, A. Nikolaev, S. Stepanov, I. Nikitina, K. Vassilevski, A. Ankudinov, Yu. Musikhin, and V. Dmitriev, in *Silicon Carbide, III-Nitride and Related Materials*, edited by G. Pensl, H. Morkoc, B. Monemar, and E. Janzen (Materials Science Forum Vols. 264–268), Trans Tech Publications, Zürich, Switzerland (1998), pp. 1121–1124.

Translated by Steve Torstveit

Observation of self-modulation regimes of generation in high-power backward-wave tubes

N. S. Ginzburg, N. I. Zaĭtsev, E. V. Ilyakov, I. S. Kulagin, Yu. V. Novozhilova, A. S. Sergeev, and A. K. Tkachenko

Institute of Applied Physics, Russian Academy of Sciences, Nizhniĭ Novgorod
(Submitted April 9, 1998)
Pis'ma Zh. Tekh. Fiz. **24**, 66–71 (October 26, 1998)

In an experiment done on a specially constructed backward-wave tube for centimeter waves, with a power level of 100 kW, it is observed that increasing the electron beam current leads to more complicated forms of self-modulation of the output radiation: the modulation is initially sinusoidal, then becomes a periodic sequence of spikes, and finally loses periodicity.
 [S1063-7850(98)02710-4]

The multifrequency dynamics of backward-wave oscillators was first investigated theoretically in Refs. 1 and 2. It was found that as the current is increased above the starting value, the regime of stationary single-frequency generation gives way to a regime of periodic self-modulation, which is initially sinusoidal but then takes the form of a sequence of spikes. As the current is increased further the shape of the signal becomes more complicated, loses periodicity, and the generation ultimately becomes stochastic. The sequence of bifurcations described above has been observed experimentally [3] on a laboratory model backward-wave tube (BWT) with a power level of tens of milliwatts.

The subject of the present paper is a theoretical and experimental investigation of the possibility of realizing self-modulation regimes of generation in a BWT with a power level of up to 100 kW. The electrodynamic system used was a smoothly corrugated axisymmetric waveguide with a cutoff narrowing at the cathode end and diffractional extraction of the radiation from the collector end. As we know, such systems have an increased dielectric strength and a simple construction and are widely used in relativistic BWTs. [4]

In the present experiment the BWT was designed for a frequency of 8 GHz. The lowest mode TE_{11} was chosen as the working mode; this choice allowed us to avoid synchronous interaction of the electron beam with other modes and the concomitant problems of mode selection with respect to the transverse mode index. The waveguide had a mean radius of 1.2 cm, a corrugation period of 1.7 cm, and a corrugation depth of 0.25 cm and was smoothly matched with the exit section on the collector end. Two structures were fabricated, differing in the length of the interaction space: 29 and 44 cm. An annular electron beam was formed in a magnetron-injector gun. A low velocity spread was ensured by a high magnetic field, with a value of 2.5 T in the interaction space. The accelerating voltage was around 70 kV, and the beam current emitted by the thermionic cathode varied from 3 to 35 A.

A preliminary modeling of the steady-state processes in a BWT oscillator was carried out using a self-consistent system of equations consisting of the equation describing the evolution of the field amplitude[1]:

$$\frac{\partial A}{\partial \tau}-\frac{\partial A}{\partial \zeta}=-\frac{J}{\pi}\int_0^{2\pi} e^{-i\vartheta}d\vartheta_0 \tag{1}$$

and the relativistic equations of motion of the electrons:

$$\frac{d\vartheta}{\partial \zeta}=\frac{1}{\sqrt{1-\gamma^{-2}}}-\frac{1}{\sqrt{1-\gamma_0^{-2}}}, \tag{2}$$

$$\frac{\partial \gamma}{\partial \zeta}=\mathrm{Re}(A(\zeta,\tau)e^{i\vartheta}). \tag{3}$$

Here $A=eE_z(mc\omega)$ is the dimensionless amplitude of the synchronous (-1)st harmonic of the field, $\tau=\omega(t-z/v_0)/(1/\beta_0+1/\beta_{gr})$, and $\zeta=\omega z/c$ are the dimensionless time and longitudinal coordinate, $\vartheta=\omega t-hz$ is the phase of the electron relative to the synchronous harmonic of the field, $J=eI|Z|/(2\beta_0^2mc^2)$, Z is the coupling impedance for this harmonic, [5] I is the beam current, γ is the relativistic mass factor of the electrons, ω is the frequency of exact synchronism, and $\beta_0=v_0/c$, $\beta_{gr}=v_{gr}/c$, where v_0 is the initial translational velocity of the electrons and ν_{gr} is the group velocity of the wave. The boundary and initial conditions on equations (1)–(3) have the form

$$A|_{\zeta=l}=0, \quad A|_{\tau=0}=A_0(\zeta),$$
$$\vartheta|_{\zeta=0}=\vartheta_0\in(0,2\pi), \quad \gamma|_{\zeta=0}=\gamma_0, \tag{4}$$

where l is the dimensionless length of the interaction space.

The calculations of the coupling impedance and starting currents were based on the use of the results of Ref. 5. The starting current of the BWT with the periodic structure 29 cm long was around 3 A, while that for the structure 44 cm long was reduced to 1 A. We note that since the BWT operated in a regime quite close to the cutoff frequency, the calculated value of the starting current depended strongly on the beam voltage.

Figure 1 shows the results of a numerical simulation of the time dependence of the amplitude of the output signal and the spectrum of the signal at different values of the current for the BWT 44 cm long, the corresponding normalized length being $l=70$. The periodic self-modulation arises at a current of the order of 3 times the threshold. The stochastic

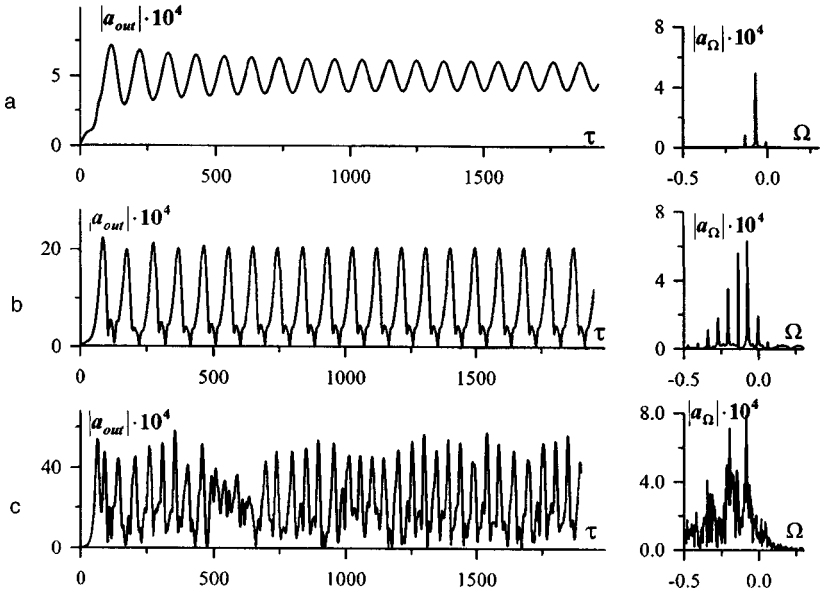

FIG. 1. Results of modeling of the time dependence of the amplitude of the output radiation and its spectrum for $l = 70$. a: $J = 1.15 \times 10 - 5$; b: $J = 3.2 \times 10^{-5}$; *c*: $J = 1.2 \times 10^{-4}$.

regime comes about when the current reaches 10–15 times the threshold. Figure 1a illustrates the sinusoidal modulation of the input signal, and Fig. 1b corresponds to the more complicated self-modulation in the form of a periodic sequence of spikes. In dimensionless variables the self-modulation period is of the order of 10^2. At a wave group velocity of 0.2 s and a particle translational velocity of 0.5 s, the self-modulation period in dimensionless quantities is 13 ns. For the estimates the value of group velocity was found from the dispersion characteristic of a smooth waveguide, ignoring the decrease in group velocity due to the deformation of the dispersion curve that is typical for corrugated waveguides. In the case of the sinusoidal self-modulation the relative width of the emission spectrum is 0.7%. Figure 1c shows a version of the stochastic self-modulation corresponding to a current of 30 times the starting current. In this version the calculated width of the spectrum reaches 5%.

The radiation was taken off from the collector end of the interaction space. The frequency of the radiation was measured with the use of a tunable filter with a bandwidth of 60 MHz and was found to be in good agreement with the calculated frequency. The detected output signal was recorded by a Tektronix 540A digital oscilloscope, which permitted storage of the entire envelope of an rf pulse up to 10 μs long for subsequent inspection of its individual parts.

In the BWT with the interaction space 44 cm long the sinusoidal self-modulation occurred at currents as low as a few amperes (Fig. 2a); as the current was increased, the modulation became complex-periodic (Fig. 2b,c), and at currents above 30 A it went over to stochastic (Fig. 2d). It should be noted that in the sequence of oscillograms given above there is no steady-state generation regime. This is because decreasing the current below 3 A was met with significant technical problems. At the same time, a steady-state generation regime was observed in the short tube with the 29-cm-long interaction length, at currents ranging from 3 to 20 A.

Comparing the oscilloscope traces of the envelope of the rf pulse as obtained from the results of the numerical simulation (Fig. 1) and the physical experiment (Fig. 2), one can

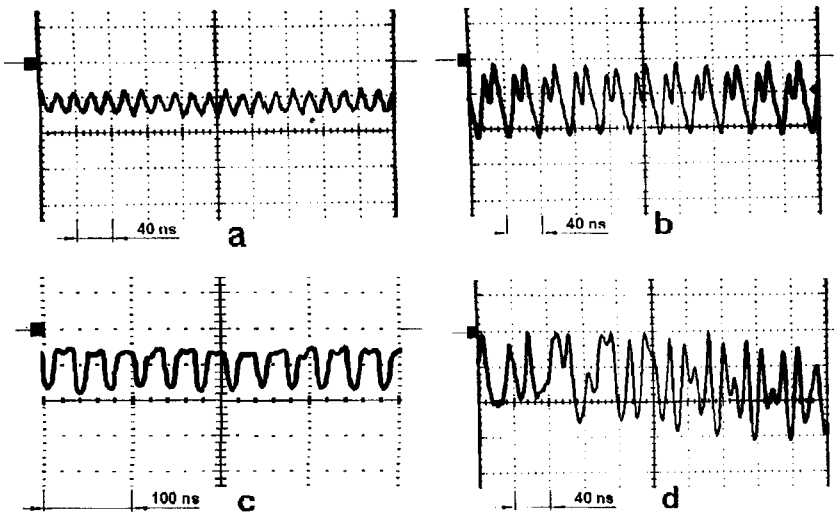

FIG. 2. Envelope of the output radiation for different values of the current. a: $I = 3$ A; b: $I = 21$ A; c: $I = 28$ A; d: $I = 35$ A.

easily see that there is qualitative agreement. Consequently, one can also assume that their spectral characteristics agree. We note, however, that the interpretation of the experimental data was based on a simplified theoretical model that left out the effect on the electrons of the asynchronous components of the rf field and of the space-charge fields and the presence of parasitic reflections at the collector end of the BWT.

It should also be emphasized that the beam voltage and beam current were chosen on considerations of restricting the output power to a level of around 100 kW, since at higher powers the microwave pulses were found to be cut short, probably because of rf breakdown inside the electrodynamic system, which was made of copper by an electrochemical plating method. It is clear that the admissible fields at the walls of the electrodynamic system can be increased significantly by using technologies ordinarily employed in industrial electronics. This would permit increasing the injection current and the supercriticality parameter and, accordingly, the average power of the stochastic radiation.

The authors are grateful to É. B. Abubakirov, L. Altgilbers, N. F. Kovalev, and M. I. Petelin for helpful discussions.

This study was supported by the Russian Fund for Fundamental Research under Grant No. 97-02-1761.

[1] N. S. Ginzburg, S. P. Kuznetsov, and T. N. Fedoseeva, Izv. Vyssh. Uchebn. Zaved. Radiofiz. **21**, 1037 (1978).
[2] V. P. Bezruchko, S. P. Kuznetsov, and D. I. Trubetskov, Izv. Vyssh. Uchebn. Zaved. Radiofiz. **21**, 1037 (1978).
[3] V. P. Bezruchko, S. P. Kuznetsov, and D. I. Trubetskov, JETP Lett. **29**, 162 (1979).
[4] N. F. Kovalev, M. I. Petelin, and M. D. Raĭzer, JETP Lett. **18**, 138 (1973).
[5] N. F. Kovalev, Élektron. Tekhn. Ser. 1. Élektron. SVCh **3**, 102 (1978).

Translated by Steve Torstveit

Influence of a shock-wave pressure gradient on the appearance of a microhardness maximum in α-Fe irradiated by a high-power ion beam

A. N. Valyaev, A. D. Pogrebnyak, S. N. Bratushka, V. I. Lavrent'ev, S. N. Volkov, and S. V. Plotnikov

Sumy Institute of Surface Modification, Sumy, Ukraine
Technical University, Ust-Kamenogorsk, Kazakhstan
Institute of Electrophysics, Urals Branch of the Russian Academy of Sciences, Tomsk, Russia
A. O. ''Vostokmash,'' Ust-Kamenogorsk, Kazakhstan
(Submitted November 20, 1997; resubmitted June 18, 1998)
Pis'ma Zh. Tekh. Fiz. **24**, 72–77 (October 26, 1998)

The results of research on the defect structure and microhardness in α-Fe irradiated by a pulsed high-power ion beam are presented. The results are obtained with the use of positron annihilation, electron microscopy, and a nanoindenter. It is shown that the pressure gradient and the depth of formation of the shock wave front in α-Fe irradiated by a high-power ion beam have an influence on the formation and location of the maximum of the dislocation density and microhardness in the modified layer. © *1998 American Institute of Physics.* [S1063-7850(98)02810-9]

High-power ion beams have well-known uses in the modification of surfaces, ion mixing, and the deposition of films and coatings. [1–4] However, there are unsolved problems that preclude making predictions as to the effect on the physicochemical and service characteristics of metallic materials. The main difficulty is to take into account all the processes that occur under irradiation by a high-power ion beam, mainly their effect on the change in the defect structure, the microhardness, and their final profile in the material. A list of the processes occurring in a metal under irradiation by a high-power ion beam includes heating, melting, evaporation, expansion of a vapor–plasma cloud (ablation), the formation of a shock wave (SW), quenching from the liquid and gaseous states, mass transport, etc.

In the present letter we report a study of the defect structure and microhardness in α-Fe after irradiation by a high-power ion beam and investigate the relationships influencing the change in the depth of the modified layer.

As objects of study we used annealed samples of α-Fe with dimensions of $14\times14\times2$ mm with a large grain size (1.5–3 mm). The irradiation by the high-power ion beam was carried out on an accelerator with beam parameters $F_{av}=300$ keV, duration $\tau=100$ ns, and current density varying from 10^6 to 2.5×10^7 A/m^2 (Ref. 5). The composition of the beam was $C^+\approx50\%$, $H^+\approx50\%$. The residual pressure in the accelerator chamber was 10^{-5} torr. The beam cross section was much larger than the size of the samples.

For electron microscope studies of the dislocation structure formed in the subsurface layers of a target under irradiation by a high-power ion beam, we prepared foils at a specified distance from the surface. The technique used to prepare the foils is described in Ref. 6. The positron lifetime was measured on a spectrometer with a time resolution of 220 ps, with a fixed width at half maximum $\Delta\tau=208$ ps. The positron source was ^{22}Na(β^+,γ) evaporated onto aluminum foil in a Mylar packet. The source intensity was $\tau_r=150$ ns; $I_1=6.6\%$; $\tau_2=450$ ps; $I_2=26\%$. The spectrum was corrected with the use of ^{207}Bi. The microhardness measurements were made on a Micromet apparatus. Measurement of the spectra of Rutherford backscattering with channeling (RBS/C) was carried out using a beam of $^4He^+$ ions with an energy of 2 MeV. In the melting zone of a surface layer of iron the defect profile was measured using a beam of slow positrons with energies of 0.2–30 keV, which permitted analysis of layers with thicknesses ranging from several nanometers to 1.2 μm.[7]

A detailed analysis of the subsurface layer that was melted as a result of the irradiation of α-Fe by a high-power ion beam was carried out using a beam of slow positrons and Rutherford backscattering of ions with channeling (RBS/C).

As a result of quenching from the liquid state (and possibly also from the gaseous state) a high concentration of vacancy clusters, impurity complexes, and dislocations is formed in a surface layer up to 1.2 μm thick; this is evidenced by the increase in the *S* parameter of the curves of the Doppler broadening of the annihilation spike in comparison with the initial (unirradiated) sample of α-Fe (Fig. 1a). A high density of vacancy clusters, $5\times10^{17}-10^{18}$ cm^{-3}, forms in the layer in which the maximum thermomechanical stresses occur (the boundary of the liquid and solid phases), and a developed dislocation structure arises (having a scalar density of 6.5×10^9 cm^{-2}; Fig. 1a, curves *2* and *3*). The results obtained by the RBS/C method (Fig. 1b) attest to the fact that the concentration of interstitial atoms has also risen, as is indicated by the increase in χ for the $\langle100\rangle$ and $\langle001\rangle$ directions as compared with the initial oriented crystal (a large grain). It should be noted that significantly more interstitial defects are formed in the $\langle100\rangle$ direction. In a subsurface layer up to 5 μm thick the dislocation structure consists of uniformly distributed individual dislocations. Right next to the surface the mean density of dislocations reaches 3.6×10^9 cm^{-2}. Substantial changes in the dislocation structure

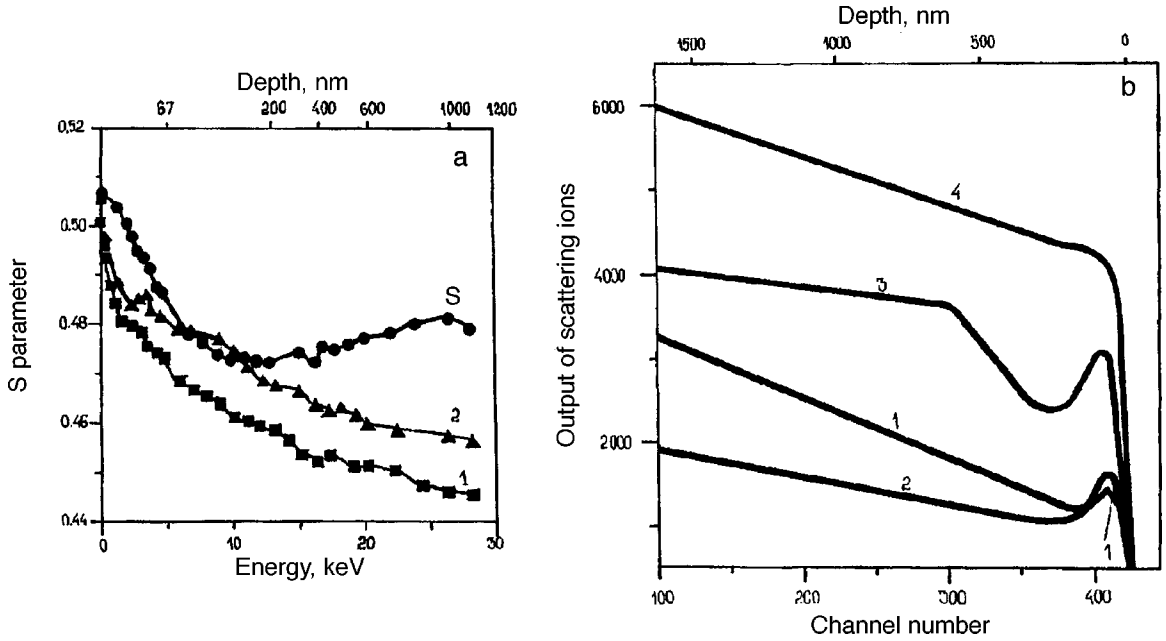

FIG. 1. a: The *S* parameter of the curves of the Doppler broadening of the annihilation spike versus depth in the α-Fe layer: *1* — initial state; *2* — irradiation by a high-power ion beam at $j=100$ A/cm^2 and $\tau=100$ ns; *3* — at $j=400$ A/cm^2 and $\tau=100$ ns. b: Energy spectra of the Rutherford backscattering of ions with channeling ($^4He^+$ ions with energy 3 MeV): *1* — the ⟨100⟩ orientation in the initial state; *2* — the ⟨001⟩ orientation, irradiation by a high-power ion beam at $j=400$ A/cm^2 and $\tau=100$ ns; *3* — the ⟨100⟩ orientation, irradiation at $j=400$ A/cm^2 and $\tau=100$ ns; *4* — misoriented grain of α-Fe.

of the sample begin at a depth of 30–40 μm, where the dislocation structure becomes extremely nonuniform. In addition to the chaotic dislocation structure made up of individual dislocations and dislocation tangles, low-angle boundaries appear in the structure, these varying from a uniform distribution of dislocations to complex interweavings of dislocations and boundaries with misorientation angles of 5–7°. Under irradiation by a high-power ion beam the thermal relaxation time is substantially less than the duration of the irradiation, and therefore the practically instantaneous heating of the metal gives rise to thermal stresses in the solid-state matrix in the subsurface region, resulting in melting and ejection of the material from the irradiated surface. The recoil momentum creates an additional compression of the material in the solid phase. We shall show that the wave generated in this case is a shock wave. A criterion of shock wave formation has been obtained for laser irradiation; [8] for our case it will have the form

$$\frac{IS}{\tau_U} > C_e^4 \rho_0 R_0, \tag{1}$$

$$Q = IS\tau \tag{2}$$

$$\mu_\lambda = R_0^{-1} \tag{3}$$

$$n = 1,$$

where I is the intensity, S is the irradiated area, and R_0 is the range of ions in the material.

For the irradiation regimes used, $I \cong 10^8$ W/cm^2 $=10^{12}$ W/m^2, $\tau=10^{-7}$ s, $S\cong 10^{-4}$ m, and the parameters of our targets, $C_e=5\times10^3$ m/s, $\rho_0=7.8\times10^3$ kg/m^3, R_0 $\cong 1\,\mu$m$=10^{-6}$ m, we obtain $(IS/\tau)\cong 10^{15}$ and $C_e^4\rho_0 R_0$ $\cong 10^{12}$.

Thus the criterion of shock wave formation is met, and its initial pressure is several GPa, i.e., the wave is weak (from 2 to 10 GPa). The pressure in the shock wave as it propagates into the depths of the target falls off, so that H_V

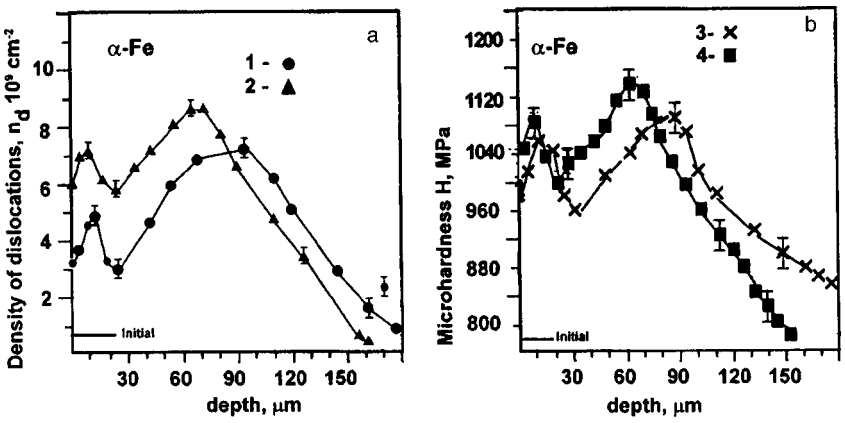

FIG. 2. Density of dislocations (a) and microhardness (b) in α-Fe irradiated by a high-power ion beam as functions of the depth of the hardened layer: *1,3* — $j=100$ A/cm^2, $\tau=100$ ns; *2,4* — $j=400$ A/cm^2, $\tau=100$ ns.

decreases with depth (Fig. 1). However, the shock wave front becomes steeper (this is confirmed by our calculations) and the gradient increases, reaching a maximum in the region of formation of the shock wave front.

The most intense generation of both intrinsic and extrinsic defects will occur in the region of the shock wave front. Since interstitial defects are substantially more mobile than vacancies, their sinking to dislocations pins the latter, lowering their mobility. A shock wave impulse is imparted to both the atoms of the matrix and the defects (scattering centers).

Figure 2a and 2b shows the mean density of dislocations (curves *1*,*3*) and microhardness (*2*,*4*) as functions of the distance from the ion-irradiated surface of the α-Fe. The curves have pronounced maxima near the surface and in the interior of the modified layer. Increasing the energy flux (and current density) of the high-power ion beam causes the second maximum to shift closer to the surface, i.e., there is an influence of the shock-wave pressure gradient and of the location at which the shock wave front forms.

This study was supported in part by the State Commission of Science and Technology of Ukraine (Project 75.4/73-93 ''Raduga'').

The authors are grateful to the staffs of Sandia National Laboratories and the Los Alamos Laboratory for discussion of the results in seminars.

[1] A. D. Pogrebnjak and Sh. M. Ruzimov, Phys. Lett. A **120**, 259 (1987).
[2] A. D. Pogrebnjak, Phys. Status Solidi A **117**, 17 (1990).
[3] A. Davis, G. Remnev, R. Stinnett, and K. Yatsui, MRS Bull. **21**, 58 (1996).
[4] K. Yatsui, C. Grigoriu, H. Kubo, K. Masugata, and Y. Shimotori, Appl. Phys. Lett. **67**, 1214 (1995).
[5] A. D. Pogrebnyak, Yu. P. Sharkeev, N. A. Makhmudov, G. I. Perevalova, and Sh. M. Tukhtaev, Poverkhnost', No. 3 (1993).
[6] Yu. F. Ivanov, A. D. Pogrebnyak, V. A. Martynenko, and R. Oshner, Fiz. Khim. Obrab. Mater. **6**, 13 (1996).
[7] A. Zecca, R. Brusa, V. Paridaens, D. Naia, A. D. Pogrebnjak, A. D. Markov, and V. P. Rotstein, Phys. Lett. B **175**, 433 (1993).
[8] B. Steverding and A. H. Werkheiser, J. Phys. D **4**, 545 (1971).

Translated by Steve Torstveit

Monitoring the deposition of an interference film by differential reflection of light

P. V. Adamson

Institute of Physics, Tartu
(Submitted January 15, 1998)
Pis'ma Zh. Tekh. Fiz. **24**, 78–86 (October 26, 1998)

The change in the reflection (differential reflection) of light from an interference film as a result of the deposition of an ultrathin layer on it is investigated. Formulas describing the differential reflection around the reflectivity minima and maxima of the film are obtained by a perturbation method. It is shown that these formulas and the corresponding differential measurements can be used for an easy and unambiguous determination of the thickness and refractive index not only of ultrathin surface layers but also of the interference films themselves. The proposed method is especially convenient for monitoring the deposition of thin-film structures. © *1998 American Institute of Physics.* [S1063-7850(98)02910-3]

Among the many optical methods for investigating the subsurface region of various materials and for monitoring the deposition (growth) of thin-film structures, extensive use is made of differential reflection methods, in which one records the change in the reflected signal due to the influence of the surface layer under investigation.[1–6] Since the most vital applications of optical probing methods are found primarily in semiconductor technology, most of the methods that have been developed work only in the presence of absorption (in a surface layer or in the substrate). Moreover, owing mainly to the incorrect theoretical analysis given in Ref. 7 for weakly absorbing and transparent materials, the opinion is often expressed in the literature that the differential reflection method can in general be used to study ultrathin layers only in the case of strongly absorbing materials.[8,9]

However, as was shown in Ref. 10 and 11, this point of view is incorrect, and the change in reflectivity due to the deposition of an ultrathin insulating layer on a transparent substrate is also measurable under certain conditions. Moreover, the existence of extensive interference in transparent films opens up a number of new possibilities, e.g., for improving the signal-to-noise ratio and sensitivity of the method of differential reflection.[12]

The goal of this study is to show how one can use the differential reflection of *p*- and *s*-polarized light to determine simultaneously the parameters of transparent interference films and ultrathin insulating layers deposited on them.

Let us consider the reflection of a linearly polarized electromagnetic plane wave with vacuum wavelength λ from an interference film f of thickness d_f on a semi-infinite substrate s in a surrounding medium a. We will treat a small change in the reflectivity of the film f due to the deposition on it of an ultrathin layer c of thickness $d_c \ll \lambda$. All of the media are assumed to be homogeneous and isotropic and perfectly transparent, with real macroscopic dielectric constants $\varepsilon_{a,c,f,s} \equiv n_{a,c,f,s}^2$, and the magnetic permeability of all the materials is assumed equal to unity. We also assume that all of the interfaces are ideal planes — there are no transition layers or interfacial roughness. Then, using the standard calculation technique for layered media,[13] we find that under the condition $4\pi n_c d_c/\lambda \ll 1$ the relative change in the intensity of the reflected signal, viz.,

$$(\Delta I/I_0)^{(s,p)} \equiv [(I_1-I_0)/I_0]^{(s,p)} = [(R_1 I_g - R_0 I_g)/R_0 I_g]^{(s,p)} = [(R_1-R_0)/R_0]^{(s,p)} \equiv (\Delta R/R_0)^{(s,p)},$$

where $R_1\{I_1\}$ and $R_0\{I_0\}$ are the reflection coefficients {intensities} of the *s*- and *p*-polarized light from the film f with and without a surface layer c, respectively, and I_g is the intensity of the incident light, can be expressed to first order in d_c/λ as follows:

$$(\Delta R/R_0)^{(s,p)} \simeq -32\pi n_a n_f^3 n_s \cos\varphi_a \cos^3\varphi_f \cos\varphi_s \times \sin 2\beta (L/M)(d_c/\lambda), \quad (1)$$

$$L = (\varepsilon_c t_a - \varepsilon_a t_c)(\varepsilon_s t_f - \varepsilon_f t_s), \quad (2)$$

$$M = [(\varepsilon_f t_a + \varepsilon_a t_f - v)(\varepsilon_s t_f - \varepsilon_f t_s) + (\varepsilon_f t_s + \varepsilon_s t_f - v) \times (\varepsilon_f t_a - \varepsilon_a t_f)\cos 2\beta]^2 + 4\varepsilon_f \varepsilon_s \cos^2\varphi_f \cos^2\varphi_s \times (\varepsilon_f t_a - \varepsilon_a t_f)^2 \sin^2 2\beta, \quad (3)$$

where $t_i = 1$ and $v = 2\varepsilon_a \sin^2\varphi_a$ for s polarization and $t_i = \cos^2\varphi_i = 1-(\varepsilon_a/\varepsilon_i)\sin^2\varphi_a$ and $v = 0$ for p polarization $(i = a,c,f,s)$, $\beta = (2\pi/\lambda) n_f d_f \cos\varphi_f$, and φ_a is the angle of incidence of the light ray in the surrounding medium a.

Figure 1 shows $(\Delta R/R_0)_{\text{ex}}^{(s,p)}$ as a function of d_f and φ_a according to calculations using the exact classical formulas (without expansion in the small parameter d_c/λ) for a plane-layered medium and also the relative errors

$$V^{(s,p)} = [(\Delta R/R_0)_{\text{ex}}^{(s,p)} - (\Delta R/R_0)^{(s,p)}]/(\Delta R/R_0)_{\text{ex}}^{(s,p)}$$

(where $(\Delta R/R_0)^{(s,p)}$ was calculated according to the approximate expression (1)). Comparative calculations of this kind show that formula (1) does not work in the region where $(\Delta R/R_0)^{(s,p)} \to 0$, but in the neighborhood of interference extrema one can get sufficient accuracy by taking into account only the first-order terms in the expansion.

Let us next consider the form that Eq. (1) takes near the minima and maxima of the reflection coefficient $R_0^{(s,p)}$. If the thickness of the interference film $d_f = d_f^{(N)} + \Delta d_f$, where

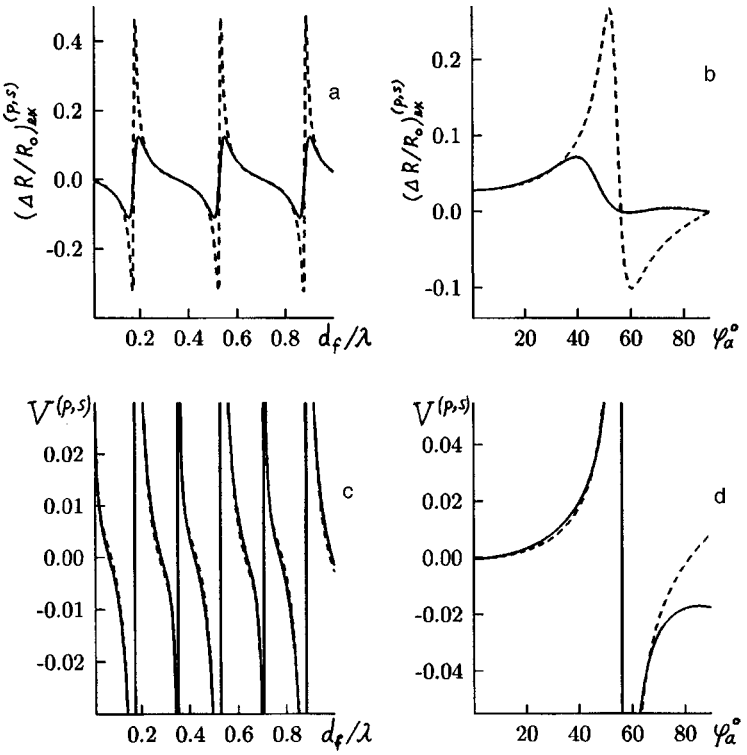

FIG. 1. Relative change in the reflection coefficient $(\Delta R/R_0)_{\text{ex}}^{(p,s)}$ and the relative error $V^{(p,s)}$ for p polarization (solid curves) and s polarization (dashed curves) as functions of the thickness d_f of the interference film (a,c) and the angle of incidence φ_a of the light (b,d). $n_a=1.0$, $n_c=2.0$, $n_f=1.5$, $n_s=2.5$, $d_c/\lambda=10^{-3}$, $\varphi_a=30°$ (a,c), $d_f/\lambda=0.6$ (b,d).

$d_f^{(N)}=N\lambda/(4n_f\cos\varphi_f)$, N is an integer, and the conditions $4\pi n_f|\Delta d_f|\lambda^{-1}\ll 1$ and $\Delta d_f\gg d_c$ hold, then for even $N=2j$, $j=0,1,2,\ldots$ we have

$$(\Delta R/R_0)_{2j}^{(s,p)}\simeq -\mathcal{K}L/(\varepsilon_s t_a-\varepsilon_a t_s)^2(d_c\Delta d_f/\lambda^2), \tag{4}$$

where $\mathcal{K}=32\pi^2 n_a n_s\cos\varphi_a\cos\varphi_s$. In the case of p polarization formula (4) does not work if the light is incident at the Brewster angle for the substrate, i.e., for $\varphi_a=\varphi_B=\tan^{-1}(n_s/n_a)$, at which point $\varepsilon_s t_a-\varepsilon_a t_s=0$. Then

$$(\Delta R/R_0)_{2j}^{(p)}\simeq 2[\varepsilon_f(\varepsilon_c-\varepsilon_a)(\varepsilon_s-\varepsilon_c)]/[\varepsilon_c(\varepsilon_f-\varepsilon_a)\times(\varepsilon_s-\varepsilon_f)](d_c/\Delta d_f). \tag{5}$$

For odd $N=2j+1$ we have

$$(\Delta R/R_0)_{2j+1}^{(s,p)}\simeq \mathcal{K}\varepsilon_f^2\cos^4\varphi_f(L/M_{s,p}^2)(d_c\Delta d_f/\lambda^2), \tag{6}$$

$$M_s=\varepsilon_a\varepsilon_s-\varepsilon_f^2+\varepsilon_a(2\varepsilon_f-\varepsilon_a-\varepsilon_s)\sin^2\varphi_a, \tag{7}$$

$$M_p=\varepsilon_a\varepsilon_s-\varepsilon_f^2+(\varepsilon_a\varepsilon_f^2\varepsilon_s^{-1}+\varepsilon_f^2-2\varepsilon_a^2\varepsilon_f^{-1}\varepsilon_s)\sin^2\varphi_a+(\varepsilon_a^3\varepsilon_f^{-2}\varepsilon_s-\varepsilon_a\varepsilon_f^2\varepsilon_s^{-1})\sin^4\varphi_a. \tag{8}$$

However, formula (6) is incorrect for s polarization when $M_s\to 0$ and for p polarization when $M_p\to 0$. If the angle of incidence and the layer parameters are chosen such that the condition $M_s=0$ or $M_p=0$ holds, then

$$(\Delta R/R_0)_{2j+1}^{(s,p)}\simeq 2(n_a\cos\varphi_a/n_s\cos\varphi_s)\times L/(\varepsilon_f t_a-\varepsilon_a t_f)^2(d_c/\Delta d_f). \tag{9}$$

We note that the conditions $M_{s,p}=0$ do not always hold, e.g., in the case of s polarization at oblique incidence it would be necessary to have $n_f<\sqrt{n_a n_s}$ (for normal incidence $n_f=\sqrt{n_a n_s}$; Ref. 13).

Which kind of extremum (maximum or minimum) corresponds to even N and which to odd N is determined for $\varepsilon_{f,s}>\varepsilon_a\sin^2\varphi_a$ by the conditions

$$(-1)^N(n_a-n_f)(n_f-n_s)\begin{matrix}<0\\>0\end{matrix} \tag{10}$$

for s polarization, and

$$(-1)^N(n_a\cos\varphi_f-n_f\cos\varphi_a)(n_f\cos\varphi_s-n_s\cos\varphi_f)\begin{matrix}<0\\>0\end{matrix} \tag{11}$$

for p polarization, where the upper sign corresponds to a minimum and the lower to a maximum. For example, it follows from these conditions that formula (5) and (9) always describe the change in reflection around a minimum of $R_0^{(s,p)}$ (this last assertion if also clear, of course, from the simpler arguments that at $M_s=0$ the reflection coefficient $R_0^{(s)}=0$ for s polarization, while for $\varphi_a=\varphi_B$ or $M_p=0$ one has $R_0^{(p)}=0$ in the case of p polarization). As we see from Eqs. (5) and (9), around these minima the relative change in the reflection coefficient is inversely proportional to Δd_f and altogether independent of the wavelength of the light (if dispersion is neglected). As a concrete example, Fig. 2 shows $(\Delta R/R_0)_{\text{ex}}^{(s,p)}$ and $V^{(s,p)}$ as functions of Δd_f around the minima and maxima of $R_0^{(s,p)}$ for incidence at the Brewster angle $\varphi_a=\varphi_B$.

Let us call attention to the following circumstance, which is extremely important in practice. It is known[14] that in the case of a semi-infinite substrate the method of differential reflection can give a high sensitivity only with p-polarized light incident at the Brewster angle, since the reflection coefficient for a smooth substrate with no surface

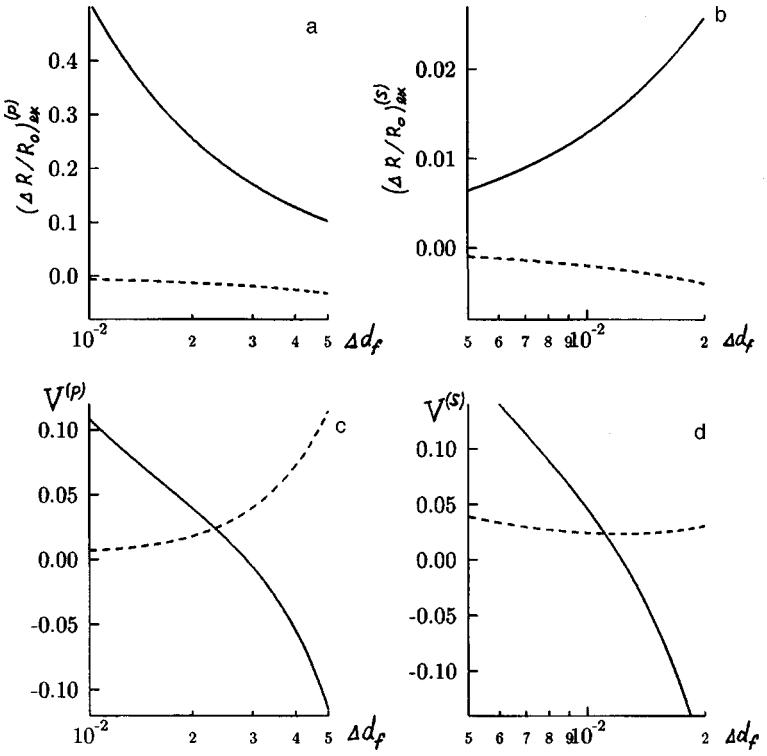

FIG. 2. $(\Delta R/R_0)^{(p,s)}_{ex}$ and $V^{(p,s)}$ as functions of Δd_f around interference minima (solid curves) and maxima (dashed curves) if $n_a=1.0$, $n_c=2.5$, $n_f=2.0$, $n_s=1.5$, $\varphi_a=\tan^{-1}1.5$, and $d_c/\lambda=10^{-3}$.

layer then approaches zero. In the case of an interference film, however, the same possibility is afforded for *s*-polarized light as well, since under the condition $n_f<\sqrt{n_a n_s}$ one can find an angle of incidence such that the original reflection coefficient for a clean film $R_0^{(s)}\to 0$.

The main utility of formulas (4)–(9) is that they make it easy to solve the inverse problem — to determine uniquely the parameters of a film f and surface layer c with known ε_s and ε_a solely by measuring $(\Delta R/R_0)^{(s)}$ and $(\Delta R/R_0)^{(p)}$ about the minimum and maximum of the reflectivity $R_0^{(s,p)}$. The parameter ε_f is obtained most simply with the use of *s*-polarized light, by determining the experimental value of $g_f=[-(\Delta R/R_0)^{(s)}_{2j}/(\Delta R/R_0)^{(s)}_{2j+1}]^{1/2}/2$ and then calculating ε_f from the formula

$$\varepsilon_f=g_f(\varepsilon_s-\varepsilon_a)+\varepsilon_a\sin^2\varphi_a+[g_f^2(\varepsilon_s-\varepsilon_a)^2+\varepsilon_a\cos^2\varphi_a(\varepsilon_s-\varepsilon_a\sin^2\varphi_a)]^{1/2}. \quad (12)$$

The dielectric constant ε_c can be determined as follows: measure the ratio $g_c=(\Delta R/R_0)^{(p)}_{2j}/(\Delta R/R_0)^{(s)}_{2j}$ and use the expression

$$\varepsilon_c=\varepsilon_a[(g_c'+1)+((g_c'+1)^2-4(g_c'+\cos^2\varphi_a)\sin^2\varphi_a)^{1/2}]\times[2(g_c'+\cos^2\varphi_a)]^{-1}, \quad (13)$$

where

$$g_c'=g_c(\varepsilon_s\cos^2\varphi_a-\varepsilon_a\cos^2\varphi_s)^2(\varepsilon_f-\varepsilon_s)/[(\varepsilon_s\cos^2\varphi_f-\varepsilon_f\cos^2\varphi_s)(\varepsilon_s-\varepsilon_a)^2].$$

Using the relation

$$\Delta d_f/\lambda=\frac{g_\Delta(\varepsilon_a+\varepsilon_s)^{1/2}(\varepsilon_f^2+\varepsilon_a\varepsilon_f+\varepsilon_f\varepsilon_s-\varepsilon_a\varepsilon_s)}{4\pi\varepsilon_f(\varepsilon_a\varepsilon_f+\varepsilon_f\varepsilon_s-\varepsilon_a\varepsilon_s)}, \quad (14)$$

where $g_\Delta=[-(\Delta R/R_0)^{(p)}_{2j+1}/(\Delta R/R_0)^{(p)}_{2j}]^{1/2}$ and is determined experimentally at the angle of incidence $\varphi_a=\varphi_B$, we obtain the value of $\Delta d_f/\lambda$. Here it proves very useful that formula (14) does not depend on the parameters of the surface layer being deposited, so that if ε_f is known, one can determine $\Delta d_f/\lambda$ provided only that the layer being deposited is a insulator and is ultrathin.

Differential reflection diagnostics of this kind are especially convenient to use for monitoring a cyclic film deposition process, where the thickness of the film increases steadily by a small step and the values of $(\Delta R/R_0)^{(s,p)}$ around the minima and maxima of the reflection coefficient $R_0^{(s,p)}$ can easily be measured for each cycle. If the growth process contains two different cycles 1 and 2, during which, respectively, two surface layers with parameters ε_{c1}, d_{c1} and ε_{c2}, d_{c2} are deposited on the surface of the film, then for a qualitative analysis one may also use the relation

$$(\Delta R_1/\Delta R_2)^{(s)}\simeq(d_{c1}/d_{c2})(\varepsilon_{c1}-\varepsilon_a)(\varepsilon_{c2}-\varepsilon_a)^{-1} \quad (15)$$

around the maxima (or around minima near which $M_s\neq 0$) for any angle of incidence, or the relation

$$\left(\frac{\Delta R_1}{\Delta R_2}\right)^{(p)}\simeq\frac{d_{c1}\varepsilon_{c2}(\varepsilon_{c1}-\varepsilon_a)(\varepsilon_{c1}-\varepsilon_s)}{d_{c2}\varepsilon_{c1}(\varepsilon_{c2}-\varepsilon_a)(\varepsilon_{c2}-\varepsilon_s)} \quad (16)$$

around the minima for an angle of incidence $\varphi_a=\varphi_B$. Since $(\Delta R_1/\Delta R_2)^{(s,p)}$ does not depend on the thickness of the film being grown, in the case of a stable process they should have constant values. It is also seen from Eq. (15) that $(\Delta R_1/\Delta R_2)^{(s)}$ does not depend on the type of substrate, while at the same time from measurements of $(\Delta R_1/\Delta R_2)^{(p)}$ for different substrates one can also determine the parameters of the surface layers. This one again shows that from the

standpoint of diagnostics it is most efficacious to work with *p*-polarized light at the Brewster angle. We also note that in principle an interference film whose thickness is only slightly different from $d_f^{(N)}$ can be used as a simple and extremely sensitive element in various kinds of remote optical sensing systems.

In closing, let us state the main result of this study: We have shown that the idea of differential measurements, which has its theoretical basis in the perturbation method, is applicable not only for studying ultrathin surface layers but also for determining the parameters of interference films.

[1] I. P. Herman, *Optical Diagnostics for Thin Film Processing*, Academic Press, New York (1996), 783 pp.
[2] G. Bauer and W. Richter (Eds.), *Optical Characterization of Epitaxial Semiconductor Layers*, Springer-Verlag, Berlin (1996), 429 pp.
[3] L. Mantese, U. Rossow, and D. E. Aspnes, Appl. Surf. Sci. **107**, 35 (1996).
[4] K. Uwai and N. Kobayashi, Appl. Surf. Sci. **107**, 42 (1996).
[5] L. Bleckmann, O. Hunderi, W. Richter, and E. Wold, Surf. Sci. **351**, 277 (1996).
[6] H. Brunner, U. Mayer, and H. Hoffmann, Appl. Spectrosc. **51**, 209 (1997).
[7] J. P. E. McIntyre and D. E. Aspnes, Surf. Sci. **24**, 417 (1971).
[8] J. F. McGilp, J. Phys.: Condens. Matter **2**, 7985 (1990).
[9] M. E. Pemble, S. R. Armstrong, S. M. Curry *et al.*, Faraday Discuss. **95**, 199 (1993).
[10] P. V. Adamson, Opt. Spektrosk. **80**, 512 (1996) [Opt. Spectrosc. **80**, 459 (1996)].
[11] A. Rosental, P. Adamson, A. Gerst, and A. Niilisk, Appl. Surf. Sci. **107**, 178 (1996).
[12] P. V. Adamson, Opt. Spektrosc. **82**, 440 (1997) [Opt. Spectrosc. **82**, 403 (1997)].
[13] M. Born and E. Wolf, *Principles of Optics*, 4th ed., Pergamon Press, Oxford (1969); Nauka, Moscow (1973), 720 pp.
[14] P. Schaaf, Ph. Dejardin, and A. Schmitt, Rev. Phys. Appl. **21**, 741 (1986).

Translated by Steve Torstveit

Spin–orbit interaction in the field of an optical vortex of a few-mode fiber

A. V. Volyar, V. Z. Zhilaĭtis, and V. G. Shvedov

Simferopol State University
(Submitted April 3, 1998)
Zh. Tekh. Fiz. **24**, 87–93 (October 26, 1998)

A quantum-mechanical analog of the spin–orbit interaction operator $\hat{\mathbf{V}}$ is constructed for the fields of optical CV vortices and TE and TM modes in an optical fiber. It is shown that the polarization correction $\delta\beta$ to the propagation constant, which is the mean value of this operator, is a measure of the ''level splitting'' of the propagation constant $\tilde{\beta}$ in the scalar case. The difference in the operation of the individual parts of the operator $\hat{\mathbf{V}}$ on the fields of CV vortices and on the fields of TM and TE modes is indicative of the presence of two different physical processes — circular and linear birefringence in the locally isotropic optical fiber. The conversion of the ''scalar'' field $\tilde{\mathbf{e}}$ to a vector field $\mathbf{e}_1$ as a consequence of the spin–orbit interaction operator can be regarded as resulting from a re-radiation of the additional field $\mathbf{e}_1$ by the vortex field $\tilde{\mathbf{e}}$, which rotates around the optical axis of the fiber. In this picture the additional field $\mathbf{e}_1$ can be regarded as being a ''relativistic'' correction to the vortex field for the distortions of the main field $\tilde{\mathbf{e}}$ and arising as a result of the rotation of the field of the optical vortex in the medium of the few-mode fiber.
[S1063-7850(98)03010-9]

The propagation of an optical vortex along a few-mode optical fiber is accompanied by precession of the Poynting vector of the electromagnetic field around the axis of the fiber.[1] This precession is the result of a nonholonomic constraint between the electromagnetic analog of the orbital and spin angular momenta of the field of the directed vortex. A measure of this nonholonomic constraint is the topological phase,[2] which takes the form of a polarization correction $\delta\beta$ to the propagation constant $\tilde{\beta}$ of the optical vortices of the fiber.[3] In this picture the polarization correction $\delta\beta$ characterizes the size of the splitting of the ''unperturbed level'' of the propagation constant $\tilde{\beta}$. The process causing the splitting of the level $\tilde{\beta}$ can be associated (by analogy with the atomic model[4]) with the spin–orbit interaction in the field of the optical vortex. Then one of the split sublevels will correspond to a propagation constant $\beta_{\mathrm{CV}}=\tilde{\beta}_{\mathrm{CV}}+\delta\beta_{\mathrm{CV}}$ for a CV vortex, and the other sublevel will correspond to the propagation constants β_{TE} and β_{TM} of the TE and TM modes of the fiber (for $l=1$).

The goal of this paper is to construct a spin–orbit interaction operator $\delta\hat{\mathbf{H}}$ for the field of optical CV vortices and TE and TM modes. The problem is considered in the framework of the formal quantum-mechanical approach that was used for the electromagnetic field in Refs. 5–7.

We write the vector wave equation for light in an inhomogeneous medium as[8]

$$(\nabla_\perp^2+n^2(r)k^2-\beta^2)\mathbf{e}_\perp=-\nabla_\perp(\mathbf{e}_\perp\nabla_\perp\ln n^2(r)), \tag{1}$$

where the subscript $\perp$ indicates the transverse components of the vectors, β is the propagation constant of the eigenmodes in an optical fiber with a gradient refractive index profile $n^2(r)=n_{\mathrm{co}}^2(1-2\Delta f(r))$, where Δ is the height of the profile $n(r)$. If the refractive indices of the core n_{co} and cladding n_{cl} are close in value, i.e., if the parameter Δ is small, then Eq. (1) can be written to first order in perturbation theory as[8]

$$(\nabla_\perp^2+n^2(r)k^2-\tilde{\beta}^2)\tilde{\mathbf{e}}_\perp=0. \tag{2}$$

Equation (2) does not take into account the polarization properties of the field and is therefore called a scalar wave equation. The vector properties of the fields are taken into account by a transformation of the scalar amplitude of the field to a vector amplitude $\tilde{\mathbf{e}}\rightarrow\mathbf{e}$, where $\mathbf{e}\approx\tilde{\mathbf{e}}+\Delta\mathbf{e}_1$ and the propagation constant $\tilde{\beta}\rightarrow\beta$, so that $\beta=\tilde{\beta}+\delta\beta$, where $\delta\beta$ is the polarization correction.

Let us find an expression for $\delta\beta$. The desired equation for the polarization correction $\delta\beta$ can be obtained by taking the conjugate of Eqs. (1) and (2) multiplied by $\tilde{\mathbf{e}}$ and $\mathbf{e}$, respectively. Then, by making use of the Hermitian property of the operator ∇^2, we obtain (the subscript $\perp$ will be dropped from now on):

$$\delta\beta=A\int_S\{\partial_i[(\tilde{e}_ie_k^*+\tilde{e}_i^*e_k)\partial_k\ln n^2]$$
$$-(e_k^*\partial_i\tilde{e}_i-e_k\partial_i\tilde{e}_i^*)\partial_k\ln n^2\}dS, \tag{3}$$

where

$$A^{-1}=\frac{2V}{\rho\sqrt{2\Delta}}\int_S(\tilde{\mathbf{e}}^*\mathbf{e}+\tilde{\mathbf{e}}\mathbf{e}^*)dS$$

is a normalization factor, the indices i and k take on the values x and y, $\partial_i=\partial/\partial x_i$, and a summation over repeated indices is implied. The first term in expression (3) upon integration can be transformed to a curvilinear integral of a real

TABLE I. Transformation of the fields and their propagation constants under the spin–orbit interaction operator.

		$\varkappa=+1 \quad l\geqslant 1$ $\varkappa=-1 \quad l>1$ $\sigma=\pm 1$ $\mathrm{CV}_{\sigma l}^{\varkappa\sigma}$	$\varkappa=-1 \quad l=1$ TM	$\varkappa=-1 \quad l=1$ TE
$\lvert\tilde{\mathbf{e}}\rangle$	e_x	$\frac{1}{\sqrt{2}}F_l e^{i\sigma l\varphi}$	$F_1\cos l\varphi$	$F_1\sin l\varphi$
	e_y	$\frac{i\varkappa\sigma}{\sqrt{2}}F_l e^{i\sigma l\varphi}$	$F_1\sin l\varphi$	$-F_1\cos l\varphi$
$\hat{\mathbf{D}}\lvert\tilde{\mathbf{e}}\rangle$	e_x	$\frac{1}{\sqrt{2}}G_l^{-\varkappa}e^{i\sigma l\varphi}$	$G_1^+\cos l\varphi$	$G_1^+\sin l\varphi$
	e_y	$\frac{i\varkappa\sigma}{\sqrt{2}}G_l^{-\varkappa}e^{i\sigma l\varphi}$	$G_1^+\sin l\varphi$	$-G_1^+\cos l\varphi$
$\hat{\mathbf{T}}\hat{\mathbf{D}}\lvert\tilde{\mathbf{e}}\rangle$	e_x	$\frac{1}{\sqrt{2}}G_l^{-\varkappa}e^{i\sigma(l+2\varkappa)\varphi}$	$G_1^+\cos l\varphi$	$-G_1^+\sin l\varphi$
	e_y	$\frac{-i\varkappa\sigma}{\sqrt{2}}G_l^{-\varkappa}e^{i\sigma(l+2\varkappa)\varphi}$	$G_1^+\sin l\varphi$	$G_1^+\cos l\varphi$
$a\langle\tilde{\mathbf{e}}\rvert\frac{\partial f}{\partial R}\hat{\mathbf{D}}\lvert\tilde{\mathbf{e}}\rangle$		$I_l^{-\varkappa}$	I_l^+	I_1^+
$a\langle\tilde{\mathbf{e}}\rvert\frac{\partial f}{\partial R}\hat{\mathbf{T}}\hat{\mathbf{D}}\lvert\tilde{\mathbf{e}}\rangle$		0	I_l^+	$-I_1^+$
$\delta\beta$		$I_l^{-\varkappa}$	$2I_l^+$	0
$\delta\beta(f=R^2)$		$-\varkappa(l+\varkappa)\frac{(\sqrt{2\Delta})^3}{2\rho V}$	0	0

$$a=\frac{(\sqrt{2\Delta})^3}{4\rho V}\frac{1}{\langle\tilde{\mathbf{e}}|\tilde{\mathbf{e}}\rangle},\quad \delta\beta=\frac{(\sqrt{2\Delta})^3}{4\rho V}\frac{\langle\tilde{\mathbf{e}}|\frac{\partial f}{\partial R}(\hat{\mathbf{D}}+\hat{\mathbf{T}}\hat{\mathbf{D}})|\tilde{\mathbf{e}}\rangle}{\langle\tilde{\mathbf{e}}|\tilde{\mathbf{e}}\rangle},$$

$$I_l^{-\varkappa}=\frac{(\sqrt{2\Delta})^3}{4\rho V}\int_0^\infty\frac{\partial f}{\partial R}F_l G_l^{-\varkappa}RdR\Big/\int_0^\infty F_l^2RdR$$

.

function, which, in view of the boundedness of the field at infinity, must go to zero. For small Δ one can assume[8] that $\mathbf{e}\approx\tilde{\mathbf{e}}$. We expand $\nabla\ln n^2(r)$ in a series to first order in Δ ($\nabla\ln n^2\approx-2\Delta\nabla f$; Ref. 8). It can be shown that for all the eigen fields of the optical fiber $\tilde{e}_k^*\partial_k f\partial_i\tilde{e}_i=\tilde{e}_k\partial_k f\partial_i\tilde{e}i*$. In this case we obtain for the polarization correction $\delta\beta$

$$\delta\beta=2\Delta A\int_S\tilde{e}_i^*\partial_i f\partial_k\tilde{e}_k dS, \tag{4}$$

which holds for both real and complex fields **e**, unlike the expression given in Ref. 8, which is satisfied only for real fields. We write the integrand in Eq. (4) in operator form:

$$\tilde{e}_i^*\partial_i f\partial_k\tilde{e}_k=(\tilde{e}_x^*,\tilde{e}_y^*)\begin{pmatrix}\partial_x f\partial_x & \partial_x f\partial_y\\ \partial_y f\partial_x & \partial_y f\partial_y\end{pmatrix}\begin{pmatrix}\tilde{e}_x\\ \tilde{e}_y\end{pmatrix}=\langle\tilde{\mathbf{e}}|\hat{\mathbf{V}}|\tilde{\mathbf{e}}\rangle. \tag{5}$$

We decompose the matrix differential operator $\hat{\mathbf{V}}$ in Pauli matrices:

$$\hat{\mathbf{V}}=\hat{\sigma}_0\hat{\mathbf{V}}_0+\hat{\sigma}_1\hat{\mathbf{V}}_1+\hat{\sigma}_2\hat{\mathbf{V}}_2+\hat{\sigma}_3\hat{\mathbf{V}}_3,$$

where

$$\hat{\mathbf{V}}_0=\frac{1}{2}(\partial_x f\partial_x+\partial_y f\partial_y)=\frac{1}{2}\partial_r f\partial_r,$$

$$\hat{\mathbf{V}}_1=\frac{1}{2}(\partial_x f\partial_x-\partial_y f\partial_y)=\frac{1}{2}\partial_r f\left(\cos 2\varphi\partial_r-\frac{1}{r}\sin 2\varphi\partial_\varphi\right),$$

$$\hat{\mathbf{V}}_2=\frac{1}{2}(\partial_x f\partial_y+\partial_y f\partial_x)=\frac{1}{2}\partial_r f\left(\sin 2\varphi\partial_r+\frac{1}{r}\cos 2\varphi\partial_\varphi\right),$$

$$\hat{\mathbf{V}}_3=\frac{i}{2}(\partial_x f\partial_y+\partial_y f\partial_x)=\frac{i}{2r}\partial_r f\partial_\varphi. \qquad (6)$$

In going to a cylindrical coordinate system we have specialized to the case of an axisymmetric fiber ($\partial_\varphi f=0$). It is convenient to represent the operator $\hat{\mathbf{V}}$ in the form

$$\hat{\mathbf{V}}=\frac{1}{2\rho^2}\frac{\partial f}{\partial R}(\hat{\mathbf{D}}+\hat{\mathbf{T}}\hat{\mathbf{D}}),$$

where

$$\hat{\mathbf{D}}=\hat{\sigma}_0\frac{\partial}{\partial R}+\frac{i}{R}\hat{\sigma}_3\frac{\partial}{\partial\varphi},$$

$$\hat{\mathbf{T}}=\hat{\sigma}_1\cos 2\varphi+\hat{\sigma}_2\sin 2\varphi=\begin{pmatrix}\cos 2\varphi & \sin 2\varphi\\ \sin 2\varphi & -\cos 2\varphi\end{pmatrix}_L$$

$$=\begin{pmatrix}0 & e^{-i2\varphi}\\ e^{i2\varphi} & 0\end{pmatrix}_C.$$

The subscripts L and C indicate that the matrix operators are represented in a linearly or circularly polarized basis, respectively.

The form of the operator (7) is analogous to that of the spin–orbit interaction for electrons in a cylindrically symmetric field. The expectation value of the operator $\hat{\mathbf{V}}$ is equal to the polarization correction $\delta\beta$ in expression (3). The operator $\hat{\mathbf{D}}$ contains terms that are analogous to the contact interaction operator $\hat{\mathbf{K}}=\hat{\sigma}_0(\partial/\partial R)$ and the spin–orbit interaction $\hat{\mathbf{S}}=(i/R)\hat{\sigma}_3(\partial/\partial\varphi)$ for an electron in the hydrogen atom[9] it follows from Eqs. (1) and (2) that the fields $\mathbf{e}$ for the CV vortices and TE and TM modes are eigenvectors of the operator

$$\hat{\mathbf{H}}=\nabla^2+n^2(r)k^2+\frac{\Delta}{2\rho^2}\frac{\partial f}{\partial R}(\hat{\mathbf{D}}+\hat{\mathbf{T}}\hat{\mathbf{D}}), \qquad (8)$$

and the propagation constants β are its eigenvalues.

Table I gives the results of the operation of the operators $\hat{\mathbf{D}}$ and $\hat{\mathbf{T}}\hat{\mathbf{D}}$ on the fields of the eigenmodes of the fiber. It is seen from Table I that these operators act quite differently on the circularly polarized CV vortices from the linearly polarized azimuthally symmetric fields of the TE and TM modes. The operator $\hat{\mathbf{D}}$ effects a transformation of the radial distribution of the field: $F_l(R)\Rightarrow G_l^{-\varkappa}(R)$, where $G_l^{-\varkappa}(R)=dF_l/dR-\varkappa(l/R)F_l$. The matrix $\hat{\mathbf{T}}$ can be represented in the form of a product of the Pauli matrix $\hat{\sigma}_1$ and the operator of rotation by an angle 2φ:

$$\hat{\mathbf{T}}=\hat{\sigma}_1\hat{\mathbf{R}}(2\varphi)=\begin{pmatrix}1 & 0\\ 0 & -1\end{pmatrix}\begin{pmatrix}\cos 2\varphi & \sin 2\varphi\\ -\sin 2\varphi & \cos 2\varphi\end{pmatrix}. \qquad (9)$$

The rotation operator $\hat{\mathbf{R}}$ transforms the value of the topological charge: $l\Rightarrow l+2\varkappa$. The matrix $\hat{\sigma}_1$ transforms the direction of circulation to the opposite: $\sigma^+\Leftrightarrow\sigma^-$. The operator $\hat{\mathbf{T}}\hat{\mathbf{D}}$ acting on the fields $\tilde{\mathbf{e}}$ for the CV vortices transforms them to orthogonal mode states. Therefore, only the operator $\hat{\mathbf{D}}$, which does not alter the state of polarization of the field but transforms the phase of a field with a definite circular polarization, contributes to the polarization correction $\delta\beta$. The situation is quite different for the action of the operators $\hat{\mathbf{D}}$ and $\hat{\mathbf{T}}\hat{\mathbf{D}}$ on the fields of the TE and TM modes. Here both parts of the operator $\hat{\mathbf{V}}$ contribute to the change in field. Consequently, in the re-radiated TE and TM field both the phase and polarization change. This difference in the action of the operator $\hat{\mathbf{V}}$ on the polarization of the fields of CV vortices and TE and TM modes is indicative of the presence of two different physical processes: 1) for the field of the CV vortices it is circular birefringence; 2) for the TE and TM modes it is linear birefringence. The presence of these two types of birefringence in a locally isotropic inhomogeneous medium was also pointed out in Refs. 10 and 11.

The values of the fields $\tilde{\mathbf{e}}$ given in Table I correspond to the zeroth corrections of the perturbation theory considered in Ref. 8. Thus the action of the operator $\hat{\mathbf{H}}$ in (8) on the fields of the characteristic CV vortices and partial IV vortices can be pictured as follows. The field $\tilde{\mathbf{e}}$ of the optical vortex, rotating around the z axis, re-radiates both the characteristic field $\tilde{\mathbf{e}}$ and an additional field $\mathbf{e}_1$. The field $\mathbf{e}_1$ is a ''relativistic'' correction to the rotating field $\tilde{\mathbf{e}}$, which restores the rotating field far from the optical axis z; thus the total angular momentum remains unchanged despite the changes in the topological charge l and the helicity σ_z.

[1] A. V. Volyar, T. A. Fadeeva, and N. A. Groshenko, Pis'ma Zh. Tekh. Fiz. **23**(22), 58 (1997) [Tech. Phys. Lett. **23**, 883 (1997)].
[2] M. Berry, Proc. R. Soc. London, Ser. A **392**, 45 (1984).
[3] A. V. Volyar, V. Z. Zhilaĭtis, T. A. Fadeeva, and V. G. Shvedov, Pis'ma Zh. Tekh. Fiz. **24**(8), 83 (1998) [Tech. Phys. Lett. **24**, 322 (1998)].
[4] L. D. Landau and E. M. Lifshitz, *Quantum Mechanics: Non-Relativistic Theory*, 3rd ed., Pergamon Press, Oxford (1977) [cited Russian original, Nauka, Moscow (1989), 768 pp.].
[5] D. Gloge and D. Marcuse, J. Opt. Soc. Am. **59**, 1629 (1969).
[6] G. Eichmann, J. Opt. Soc. Am. **61**, 161 (1970).
[7] V. S. Liberman and B. Ya. Zel'dovich, Phys. Rev. A **46**, 5199 (1992).
[8] A. W. Snyder and J. D. Love, *Optical Waveguide Theory*, Chapman and Hall, New York (1983); Radio i Svyaz', Moscow (1987), 656 pp.
[9] A. S. Davydov, *Quantum Mechanics*, 2nd ed., Pergamon Press, Oxford (1976) [cited Russian original, Nauka, Moscow (1976), 703 pp.].
[10] A. V. Volyar, Yu. N. Mitsaĭ, V. I. Myagkov, and T. A. Fadeeva, Pis'ma Zh. Tekh. Fiz. **20**(3), 48 (1994) [Tech. Phys. Lett. **20**, 111 (1994)].
[11] V. S. Liberman and B. Ya. Zel'dovich, Phys. Rev. A **49**, 2389 (1994).

Translated by Steve Torstveit